Europe PMC Funders Group
Author Manuscript
Chem Rev. Author manuscript; available in PMC 2015 October 19.

Published in final edited form as:
Chem Rev. 2015 October 14; 115(19): 10907–10937. doi:10.1021/cr500314d.

Non-invasive Imaging of Nanomedicines and Nanotheranostics: Principles, Progress and Prospects

Sijumon Kunjachan[a], **Josef Ehling**[a], **Gert Storm**[b,c], **Fabian Kiessling**[a,*], and **Twan Lammers**[a,b,c,*]

[a]Dept. of Nanomedicines and Theranostics, Institute for Experimental Molecular Imaging (ExMI), University Clinic and Helmholtz Institute for Biomedical Engineering, RWTH Aachen University, Pauwelsstrasse 30, 52074 Aachen, Germany [b]Dept. of Targeted Therapeutics, MIRA Institute for Biomedical Technology and Technical Medicine, University of Twente, PO Box 217, 7500 AE, Enschede, The Netherlands [c]Dept. of Pharmaceutics, Utrecht Institute for Pharmaceutical Sciences (UIPS), Utrecht University, Universiteitsweg 99, 3584 CG Utrecht, The Netherlands

1. INTRODUCTION

Nanomedicine is defined as "the application of nanotechnology to medicine, including the use of nanometer-sized carrier materials for facilitating disease diagnosis, disease treatment and treatment monitoring"[1]. Examples of carrier materials routinely used for nanomedicine applications are liposomes, polymers, micelles, dendrimers, nanoparticles and antibodies (Figure 1) [2-5]. Nanomedicines have several advantages over standard low-molecular-weight agents. They are for instance able to I) protect the payload from premature clearance, enzymatic degradation and/or exposure to potentially harmful physiological conditions; II) improve the biodistribution and target site accumulation of drugs and imaging agents; III) improve the *in vivo* efficacy of diagnostic and therapeutic interventions; IV) attenuate drug and imaging agent accumulation in healthy, non-target tissues; and V) reduce the incidence and intensity of side effects [6-9]. Nanomedicines can overcome several of the biological, physical, chemical and clinical barriers associated with (in-) effective drug delivery to pathological sites [10-13], and they have been shown to be valuable tools for improving the therapeutic index of low-molecular-weight agents in cancer, inflammatory disorders, infections and other life-threatening diseases. Several nanomedicines are nowadays routinely used in the clinic, including e.g. Doxil/Caelyx (PEGylated liposomes containing doxorubicin), Abraxane (paclitaxel-loaded albumin nanoparticles), Oncaspar (PEG-L-asparaginase), Depocyt (liposomal cytarabine) and Genexol-PM (polymeric micelles containing paclitaxel). A significant number of additional nanomedicine formulations are in clinical trials, in particular for the treatment of cancer, and many more are currently being evaluated at the preclinical level.

[*]Corresponding authors: Prof. Twan Lammers, Prof. Fabian Kiessling, Dept. of Experimental Molecular Imaging, RWTH Aachen University Clinic, Pauwelsstrasse 30, 52074 Aachen, Germany. Tel: +49-241-8080116. Fax: +49-241-803380116. tlammers@ukaachen.de, fkiessling@ukaachen.de.

Europe PMC Funders Author Manuscripts
Europe PMC Funders Author Manuscripts

Europe PMC Funders Author Manuscripts

Europe PMC Funders Author Manuscripts

To better understand and to optimize drug delivery to pathological sites, it is important to quantitatively monitor various different aspects of the drug delivery process, including e.g. pharmacokinetics, biodistribution, target site accumulation, local distribution at the target site, localization in healthy tissues, kinetics of drug release, and therapeutic efficacy. Therefore, in recent years, there has been an increasing focus on the use of non-invasive imaging techniques, such as positron emission tomography (PET), single photon emission computed tomography (SPECT), computed tomography (CT), magnetic resonance imaging (MRI), optical imaging (OI) and ultrasound (US), for monitoring drug delivery, drug release and drug efficacy [14-25].

Among these techniques, CT, MRI and US can be used both with and without contrast agents. In case of the former, i.e. when contrast agents are used, these modalities require pre-scans, to determine the background level of CT, MRI and US signal prior to contrast agent administration. Such baseline measurements are needed to quantify the functional or molecular imaging information. Conversely, in the case of 'hot-spot' techniques, such as PET and SPECT (and certain forms of OI), no background signals are detected in the absence of contrast agents, and pre-scans are not needed. Hot-spot imaging techniques consequently do not provide any anatomical information, and they need to be combined with modalities such as CT or MRI, which are highly useful for anatomical and morphological imaging. This results in hybrid imaging techniques, such PET-CT, SPECT-CT and PET-MRI, in which the anatomical information obtained using CT or MRI is used to assist in allocating the functional and molecular hot-spot information to the correct organ or tissue.

It is important to take into account in this regard that each of the above-introduced imaging modalities is employed for a different purpose, based on its specific capabilities, its sensitivity and its specificity. Figure 2 provides an overview of the most important applications of non-invasive imaging techniques in nanomedicine and drug delivery research. Since each of these modalities conveys a different type anatomical, functional or molecular imaging information, and since each of them has its own specific pros and cons, it is imperative to have a proper understanding of the properties, the specific uses and the clinical translatability of each of these imaging techniques, in order to properly assess their suitability for nanomedicine-based diagnostic, therapeutic and theranostic interventions. Here, we therefore summarize the basic properties of these techniques, we describe selected examples from the literature demonstrating the specific suitability of each of these modalities for drug delivery purposes, and we provide a framework for the rational use of non-invasive imagingin nanomedicine research.

2. POSITRON EMISSION TOMOGRAPHY

Positron emission tomography (PET) is an imaging technique in which positron-emitting radionuclides are visualized and quantified. The emitted positrons annihilate nearby electrons, thereby generating two 511 keV photons, which are detected by detectors embedded in PET scanners. Examples of routinely used positron-emitting isotopes are ^{11}C, ^{13}N, ^{15}O, ^{18}F, ^{44}Sc, ^{62}Cu, ^{64}Cu, ^{68}Ga, ^{72}As, ^{74}As, ^{76}Br, ^{82}Rb, ^{86}Y, ^{89}Zr, and ^{124}I [26-33]. Given the exquisite sensitivity of PET scanners and the excellent tissue-penetrating properties of photons, radionuclide concentrations in the (sub-) picomolar range

Europe PMC Funders Author Manuscripts

Europe PMC Funders Author Manuscripts

generally suffice to generate high signal-to-noise-ratios, and render useful images and quantitative information. Therefore, PET is routinely used in the clinic for disease diagnosis, disease staging and therapy monitoring [26;34-37].

Because of its high sensitivity, unlimited penetration depth, quantifiable results and the broad range of available radionuclides, PET is highly suitable for monitoring the pharmacokinetics, the biodistribution and the target site accumulation of nanomedicine formulations. PET probes can be conjugated to or encapsulated within nanomedicines, e.g. via chelating groups such as DOTA, DTPA or HYNIC. In addition, ^{11}C- or ^{18}F-containing drug molecules or nanomedicine components can be incorporated for quantitative *in vivo* analyses [38-46]. An advantage of this is that the physicochemical and pharmacokinetic properties of the drugs and nanoformulations can be preserved, as no additional chelating groups have to be introduced for radiolabeling. Disadvantages associated with PET include the lack of anatomical information, the relatively low spatial resolution and the necessity for using radioactive probes. The former two can be overcome by using hybrid imaging techniques, such as PET-CT and PET-MRI. Via appropriate co-registration tools, fused PET-CT and PET-MRI images can be generated, which can much more clearly depict the anatomical and spatial distribution of the probe in the tissue or organ of interest, and which can provide more detailed and more meaningful information on the overall levels of probe accumulation [47-50].

Among the many examples available in the literature, a representative study in which PET was used to analyze the biodistribution of nanomedicine formulations has been published by Ferrara and colleagues, who prepared long-circulating PEGylated liposomes carrying ^{18}F-containing lipids (Figure 3A) [51]. Free ^{18}F-fluorodipalmitine (FDP) and liposome-incorporated ^{18}F-FDP were intravenously (i.v.) injected into male Fisher rats via the tail vein. A continuous bed motion scan was performed at 90 min post i.v. injection (p.i.), to enable PET scanning of the entire animal. Maximum intensity projections (MIP) were acquired, and the biodistribution of free ^{18}F-FDP versus liposome-incorporated ^{18}F-FDP was analyzed. Figure 3A shows the overall distribution pattern of free and of liposome-associated ^{18}F-FDP. As can be clearly seen, for free ^{18}F-FDP, there was substantial accumulation in the liver (6% ID/cc) at 90 min p.i., and somewhat less accumulation in spleen (4% ID/cc) and lungs (2% ID/cc). PEGylated liposomes encapsulating ^{18}F-FDP, on the other hand, were retained in systemic circulation much more efficiently, as exemplified by the almost exclusive visualization of the heart and of large blood vessels, confirming their prolonged circulation times (Figure 3A) [51].

Another exemplary study illustrating the suitability of PET-based imaging for whole-body pharmacokinetic and biodistributional analyses was published by Andreozzi et al., who studied the *in vivo* behavior of solid lipid nanoparticles (SLN) containing bovine serum albumin (BSA) radiolabeled with ^{64}Cu via the chelator 6-[p-(bromoacetamido)-benzyl] -1,4,8,11-tetraazacyclo-tetradecane- *N*,*N'*,*N"*,*N'"*- tetra acetic acid (BAT) [52]. Static PET scans were acquired at 0.5, 3, 20 and 48 h post i.v. injection. The scans were reconstructed to yield 3D structures and the intensity of radioactivity was measured for several organs of interest. These organs were later excised to quantify the overall amounts of radioactivity using a gamma counter. As shown in Figure 3B, the PET images displayed signals in the

Europe PMC Funders Author Manuscripts

Europe PMC Funders Author Manuscripts

carotid (C) and in the heart (H) at 0.5 and 3 h p.i., indicating SLN presence in systemic circulation. At later time points, SLN were cleared from the blood, and accumulated in liver (L), spleen (S) and intestine (I). The non-invasive imaging results were validated at ~52 h p.i., using *ex vivo* gamma counting, showing the highest levels of accumulation in the liver (6.6±0.7% ID/g), followed by spleen (2.9±1.1 %ID/g), right (2.2±0.2 %ID/g) and left (1.7±1.1 %ID/g) kidney, intestine (1.7±0.9 %ID/g), lungs (1.2±0.5 %ID/g) and heart (1.1±0.4 %ID/g). The results obtained using *in vivo* PET imaging and *ex vivo* gamma counting were correlated, and were found to match very well, exemplifying the high suitability of PET for non-invasive and quantitative biodistribution monitoring.

Focusing on tumor-targeted drug delivery, Lee and colleagues used PET to determine the difference between RGD-targeted vs. non-targeted nanomedicines [53]. To this end, they functionalized iron oxide (IO) nanoparticles with arginine-glycine-aspartic acid (RGD) peptides for targeting to tumor blood vessels (via $\alpha_v\beta_3$, $\alpha_v\beta_5$ and $\alpha_5\beta_1$ integrin receptors; overexpressed by activated endothelial cells), and they modified them with DOTA to enable ^{64}Cu complexation and simultaneous PET-MR monitoring (Figure 3C). The biodistribution of the constructs was evaluated in nude mice bearing human U87MG tumors, and as exemplified in Figure 3D, the obtained PET images clearly demonstrated a difference in tumor uptake for RGD-targeted vs. non-targeted nanoparticles. Accumulation of the tumor angiogenesis-specific ^{64}Cu-DOTA-IO-RGD probe was found to start at around 1 h p.i., and became prominent at 4 h p.i. In case of non-targeted probes and in blocking experiment (upon pre-administration of excess free RGD), on the other hand, hardly any accumulation in tumors could be visualized (Figure 3C). In order to confirm the findings obtained using PET, the targeted and non-targeted IO particles were also examined using MRI [53]. These results confirmed the high and specific tumor uptake of the RGD-targeted constructs at 4 h post i.v. injection. It is important to note in this regard that imaging (RGD-targeted) nanomedicine formulations is not restricted to oncology, but is also increasingly employed in inflammatory disorders, in particular in case of cardiovascular pathologies, for instance for monitoring early-stage atherosclerosis [54-61].

Sentinel lymph nodes are the sites first reached by metastatic cancer cells in the body, and are the main channels for metastatic spread. Consequently, sensitively and specifically identifying sentinel lymph nodes is highly important for tumor staging, and is decisive in deciphering appropriate therapeutic regimens for treating metastatic cancers. The high sensitivity of PET might be very helpful for visualizing and identifying sentinel lymph nodes, using e.g. radioactively labeled nanomedicine formulations. An example of this is provided in Figure 3D, showing mice bearing highly metastatic 4T1-murine breast carcinoma tumors (NB: 4T1 cells were injected into the ankle region of the left hind limb) upon the administration of multimodal ^{64}Cu-labeled mesoporous silica nanoparticles containing besides ^{64}Cu also gadolinium and a near-infrared optical imaging agent (see Chapter 6 and Figure 9 for more details) [62]. PET imaging was carried out at four different time points after the administration of the particles into the foot sole, i.e. at 1, 6, 24 and 48 h p.i., to visualize drainage via the sentinel lymph nodes. Figure 3D shows a very strong signal, indicating high probe accumulation, in the tumor sentinel lymph node at 1 h p.i. (as high as 80% ID/g). From 6 h p.i. onwards, some accumulation of nanoparticles was

Europe PMC Funders Author Manuscripts

Europe PMC Funders Author Manuscripts

observed in the liver, which reached a maximum at 48 h post i.v. injection. There was a very clear demarcation of the tumor sentinel lymph node as compared to the normal contralateral lymph node: PET signals in the former were 35- and 7-fold higher than in the latter, on day 1 and day 2 p.i., respectively.

Given the prolonged circulation time of nanomedicines, as well as their gradual (EPR-mediated) accumulation in pathological tissues over time, PET tracers with long radioactive half-lives are preferred. As exemplified by Figure 4A, the half-life time of PET radionuclides varies significantly, from several minutes to several days. For nanomedicine research, besides ^{64}Cu ($t_{1/2}$ = 13 h), radionuclides such as ^{89}Zr, $^{72/74}$As and ^{124}I are therefore of particular interest [63]. In this context, ^{89}Zr ($t_{1/2}$ = 78 h) has already been relatively extensively employed for monitoring tumor targeting [64;65], for detecting tumor-associated macrophages[66], and for visualizing and quantifying the biodistribution and the target site accumulation of monoclonal antibodies[67-75]. As an example, in a recently published study by Pérez-Medina and colleagues, PEGylated liposomal nanomedicines were labeled with ^{89}Zr to enable prolonged PET-CT imaging [76]. The authors used two different liposome labeling strategies, i.e. click labeling and surface chelation (based on dibenzoazacyclooctyne (DBCO) and deferoxamine (DFO), respectively) to track their formulations (Figure 4B). The two different types of liposomes, i.e. click labeled liposomes (CLL) and surface chelation liposomes (SCL), were evaluated in NCr nude mice bearing 4T1 breast cancer xenografts. It was found that ^{89}Zr-labeled SCL enabled a more realistic reflection of liposome biodistribution than ^{89}Zr-labeled CLL, with a blood half-life time of ~7 h vs. ~1 h, respectively, and with significantly higher levels of tumor accumulation (up to 14 %ID; Figure 4C). These differences were attributed to differences in the labeling efficiency and labeling stability of SCL vs. CLL. ^{89}Zr-based PET imaging has also already been employed to monitor nanomedicine targeting to cardiovascular pathologies. An interesting example of this has recently been reported by Majmudar et al, who aimed to specifically detect macrophages in atherosclerotic plaques [77]. In this study, dextran nanoparticles (DNP) were functionalized with DFO to enable hybrid PET-MR imaging (Figure 4D-E). As in the case of liposomes (cf. Figure 4C), ^{89}Zr-DNP primarily accumulated in liver and spleen, but also showed prominent localization in macrophages in plaques in the aortic root of atherogenic ApoE$^{-/-}$ mice. These efforts exemplify that ever more efforts in this area of research are moving towards the labeling of long-circulating nanomedicines with long-lived PET nuclides, and they illustrate the usefulness of PET for visualizing and quantifying the biodistribution and the target site accumulation of nanomedicines.

3. SINGLE PHOTON EMISSION COMPUTED TOMOGRAPHY

Single photon emission computed tomography (SPECT) is similar to PET from a nanomedicine point of view. As opposed to the coincident gamma rays used to reconstruct PET images, however, SPECT is based on non-coincident gamma rays generated by radionuclides. Consequently, the sensitivity of SPECT is about an order of magnitude lower than that of PET and its quantification is somewhat more difficult. Prototypic examples of radio-isotopes used in SPECT are ^{99m}Tc, ^{111}In, ^{123}I and ^{201}TI. In contrast to PET, where all emitted gamma photons have an energy of 511 keV, energies routinely used in SPECT are

Europe PMC Funders Author Manuscripts

Europe PMC Funders Author Manuscripts

different, and energy-dependent imaging enables the assessment of different radiotracers and thus of different radiolabeled (nano-) probes at the same time. Analogous to PET, the most important advantages of SPECT are high sensitivity, highly quantitative results and high penetration depth. Disadvantages include lack of anatomical information, the relatively low spatial resolution and the need for using radioactive probes. The former can be overcome by resorting to hybrid imaging techniques, in which SPECT is generally combined with CT (and to a lesser extent with MRI).

A nice example illustrating the suitability of SPECT-CT-based hybrid imaging for monitoring nanomedicine-mediated drug targeting has been reported by Head and colleagues, who used a synergistic therapeutic approach, i.e. radiofrequency ablation (RFA) plus i.v. administered liposomal doxorubicin, to visualize and quantify drug delivery to tumors, and to analyze its therapeutic effects [78]. Nude rats bearing head-and-neck squamous cell carcinoma (SCC) xenografts on both sides of the skull base were employed, to analyze the effect of RFA on drug delivery and efficacy. RFA treatment was performed 5 min after the i.v. injection of ^{99m}Tc-labeled liposomal doxorubicin. One of the two tumors (indicated by the arrow in Figure 5A) was subjected to RFA, whereas the other one (indicated by the arrowhead) was used as an intra-individual control. Both the transaxial and the coronal images obtained in these analyses demonstrated that RFA is able to substantially increase the tumor accumulation of radiolabeled liposomal doxorubicin (likely both by direct (i.e. thermal) and by indirect (i.e. inflammation-related) effects) [78], and they also convincingly showed that SPECT is able to depict these differences with high sensitivity and high specificity.

In another interesting study, Chrastina et al. reported on the applicability of hybrid SPECT-CT for the non-invasive monitoring of nanomedicine-based drug targeting to the lungs [79]. To this end, generation-5 poly(amidoamine) dendrimers (G5-PAMAM; Figure 5B) were functionalized with antibodies targeted to aminopeptidase P2 (APP2), to mediate specific lung homing. Upon radiolabeling with ^{125}I, the dendrimers were i.v. administered to healthy mice, followed by whole body SPECT-CT imaging at 1 h post i.v. injection. As shown in the right panels in Figure 5B, in case of non-targeted G5-PAMAM-dendrimers, the vast majority of the administered dose accumulated in organs of the mononuclear phagocytic system (MPS), such as liver and spleen. APP2-antibody targeted nanoformulations, on the other hand, displayed a very strong affinity toward lung tissue (left panels in Figure 5B), thereby nicely exemplifying the possibility of combining molecular SPECT with anatomical CT for non-invasively imaging the *in vivo* distribution of passively vs. actively targeted nanomedicine formulations.

Using a similar experimental setup, Zhang and colleagues employed SPECT-CT to assess the potential of targeting the Ephrin B4 receptor (EphB4R) for specific homing of nanomedicines to prostate cancer xenografts [80]. An EphB4R-specific peptide (TNYL-RAW) was developed, and coupled to PEG-coated and core-crosslinked polymeric micelles (CCPM), which were double-labeled with ^{111}In and the near-infrared dye Cy7 (Figure 5C). The TNYL-RAW-targeted CCPM were i.v. injected into nude mice bearing EphB4R-positive PC3 and EphB4R-negative A549 tumor xenografts, and tumor accumulation was visualized and quantified. In addition, pre-blocking experiments with free TNYL-RAW

Europe PMC Funders Author Manuscripts

Europe PMC Funders Author Manuscripts

were performed, and peptide-free controls CCPM were evaluated, to substantiate target-specific binding. As shown in Figure 5C, using hybrid SPECT-CT, efficient target site accumulation at 24 h p.i. was only observed for TNYL-RAW-CCPM. Scintillation counting and histological evaluation were carried out to validate the tumor-specific accumulation of these CCPM in EphB4R-positive tumors, confirming efficient binding and tumor targeting only for peptide-modified micelles, and exemplifying the usefulness of SPECT for non-invasively visualizing and quantifying the biodistribution of nanomedicine formulations.

4. COMPUTED TOMOGRAPHY

Computed tomography (CT) is an x-ray-based imaging technique, which allows the cross-sectional 3D visualization of organs and tissues of interest. CT generates high-resolution anatomical images using highly electron-dense contrast agents, such as iodine and barium, and aids in the assessment of disease differentiation, in perfusion analyses and in angiography. CT has decent soft versus hard tissue contrast when contrast agents are used; this contrast is poor, however, when no contrast agents are administered. Without contrast agents, CT is nonetheless highly suitable for visualizing highly electron-dense (hard) tissues, such as bone. Consequently, it is widely used for orthopedic applications, as well as for hybrid imaging purposes, providing high-resolution anatomical information to aid in the assessment of PET-, SPECT- and OI-based protocols. Low contrast agent sensitivity, the (consequent) need for high contrast agent doses and potential contrast agent-related toxicities are some of the primary points of concern associated with CT. To overcome these shortcomings, as will be outlined below, several nanomedicine-based constructs and concepts have been designed and evaluated.

To facilitate angiography and perfusion monitoring, De Vries and colleagues prepared iodine-containing polymeric nanoemulsions, and evaluated their retention in systemic circulation (as well as their organ accumulation) using high-resolution micro-CT imaging [81]. Iodine-loaded poly(butadiene)-b-poly(ethylene glycol) (PBD-PEG) block copolymer self-assemblies (Figure 6A) were i.v. injected into healthy mice, and the signal changes due to the presence of contrast agent were determined in blood, urine, heart, liver, spleen and kidney. Transversal and coronal CT scans acquired at 12 min p.i. convincingly showed that the probe is detectable in the heart (as indicated by the arrows in Figure 6A), showing its reasonable retention within systemic circulation. Circulation times followed first-order kinetics, with a half-life time of ~1 h. As expected, over time, the formulation gradually accumulated in organs of the mononuclear phagocytic system (MPS), most notably in the spleen. Based on these findings, the authors concluded that such relatively long-circulating iodine-containing nanoemulsions are suitable contrast agents for CT angiography and perfusion analyses.

In spite of its relatively low sensitivity towards contrast agents, CT imaging has in a number of studies been employed for analyzing the biodistribution of nanomedicines. Zheng and colleagues, for instance, prepared liposomes containing iohexol, and performed quantitative CT imaging to assess their distribution in a rabbit tumor model [82]. In this study, healthy male rabbits bearing VX2 sarcoma tumors in the left lateral quadriceps were injected with liposomal contrast agent via an ear vein catheter. CT images of the animals were acquired

Europe PMC Funders Author Manuscripts

Europe PMC Funders Author Manuscripts

pre- and post- administration of the liposomal formulation (at 30 min and at 1, 2, 3, 5, 7, 10 and 14 d p.i.). Figure 6B shows axial images of several organs and tissues of interest (panel 1). After an initial retention phase within the systemic circulation, liposomes eventually accumulated in tumor, liver and spleen. The developed formulation exhibited a very long circulation time, with a half-life time of ~65 h. Seven days after i.v. injection, a tumor concentration of ~1.1% of the injected dose was observed, and a tumor-to-muscle ratio of ~12, indicating efficient passive drug targeting to tumors. This study therefore demonstrates that in spite of relatively low contrast agent sensitivity, CT imaging does enable the longitudinal assessment of nanomedicine biodistribution and target site accumulation. Similarly, the whole body CT images of the rabbits at 30 min, 24 and 48 h p.i. clearly showed a gradual opacification of the tumor region, confirming the accumulation of iohexol-containing liposomes (Figure 6B, panel 2). The lower panels in Figure 6B depict the accumulation of liposomes in tumors over time, up until day 14. The occupancy peaked at 72±5% at 48 h p.i., likely coinciding with the peak in EPR, and from then onwards, the liposomes were gradually cleared from the tumor. This study therefore nicely demonstrates that in spite of the relatively low contrast agent sensitivity of CT, it can still be used to visualize and quantify EPR-mediated passive drug targeting.

In a similarly interesting study from the same laboratory, Dunne and colleagues used CT imaging to evaluate the tumor targeting potential of iohexol-loaded PEGylated liposomes functionalized with NGR-peptides, which target the tumor vasculature [83]. Nude mice bearing subcutaneous H520 xenografts in their right hind flanks were used for this study. Standard and NGR-targeted PEGylated iohexol-liposomes were administered as an i.v. bolus injection via the lateral tail vein. Anatomical whole body micro-CT scans were performed at several different time points p.i. (i.e. 0.17, 8, 24, 48, 72, 96 and 144 h). The increase in signal intensity was recorded, converted to Hounsfield units (HU) and compared to pre-injection values. Iodine concentrations in a particular 3D ROI were determined via the mean increase in HU. Figure 6C shows coronal sections of the whole body biodistribution of the probes. The tumor accumulation (arrows) of several different formulations, with varying NGR density and PEG length, was visualized and quantified. Image analysis revealed that the formulation containing 0.64 mol% of NGR-PEG_{2000}-DSPE displayed the highest degree of tumor accumulation, which was about a 2-fold higher as compared to non-targeted liposomes. The transversal tumor sections in the bottom panels in Figure 6C furthermore provide insights into the heterogeneity of liposome accumulation and distribution within the tumor. Even though the dynamic range of signal intensities is relatively low (because of the relatively poor contrast agent sensitivity of CT), differences between the different formulations can be visualized, confirming the notion that CT-based biodistribution and tumor accumulation monitoring is in principle feasible.

5. MAGNETIC RESONANCE IMAGING

Magnetic resonance imaging (MRI) is based on a principle similar to that used in chemical nuclear magnetic resonance (NMR) analysis, in which the spins of specific atomic nuclei are visualized within the body. Despite its common use in disease differentiation, disease diagnosis and therapy monitoring, MRI is also widely used for nanomedicine research, to perform pharmacokinetic and biodistribution analyses, to monitor drug release and to enable

Europe PMC Funders Author Manuscripts

Europe PMC Funders Author Manuscripts

cell-tracking studies. MRI encompasses relaxivity-based analyses (with and without contrast agents), diffusion-weighted imaging (DWI), and endogenous/exogenous magnetic resonance spectroscopy (MRS). Several reports and reviews have extensively described the physicochemical basis of MRI and of (nanoparticle-based) MR contrast agents [55;84-92]. In general, MRI serves as a highly useful and broadly applicable platform for (pre-) clinical diagnosis and therapy monitoring. There are, however, several disadvantages associated with MRI, such as relatively low contrast agent sensitivity, relatively difficult quantification procedures, and the time and cost involved.

In principle, MRI can be used relatively well for monitoring the biodistribution and target site accumulation of nanomedicines. PET and SPECT imaging, however, are generally preferred for such purposes, because of their higher contrast agent sensitivity, and easier quantification procedures. On the other hand, MRI is exquisitely suitable for monitoring drug release and drug efficacy. The former relates to the fact that T_1-MR contrast agents, as opposed to radionuclides, depend on access to freely diffusing water molecules to generate contrast, and therefore render different signals when present within vs. outside of a nanocarrier, thereby providing optimal conditions for assessing drug release [93]. The latter relates to the excellent soft-tissue contrast of MRI, which enables the non-invasive and highly accurate detection of e.g. tumors and sites of inflammation, which make it highly useful for longitudinally monitoring therapeutic responses. MRI is furthermore highly suited for multimodal imaging approaches, e.g. as in case of PET-MRI, in which it is used to provide the anatomical (and potentially also functional) information needed to more accurately assess the biodistribution and target site accumulation of radionuclide-labeled nanomedicines.

A representative example of a study in which MRI is used to monitor the target site accumulation of nanomedicine formulations has been published by Huang and colleagues [94]. They synthesized generation-3 poly-l-lysine-based dendrimers coupled to chlorotoxin (CTX), and evaluated their tumor targeting potential in a rat model of glioblastoma. C6 glioma cells were injected into the right frontal hemisphere of the rats, and CTX was used as a targeting ligand, because of its high affinity for glioma cells (as well as for other tumor cells of neuroectodermal origin; such as medulloblastoma, prostate cancer, sarcoma and intestinal carcinoma). Three different formulations were injected intravenously, i.e. low-molecular-weight Gd-DTPA, Gd-DTPA-D3-PEG and actively targeted DTPA-D3-PEG-CTX. As exemplified by Figure 7A, using all three formulations, signals corresponding to the tumor could be visualized as early as 5 min post i.v. injection. From then onwards, the tumor-specific signal started to fade for Gd-DTPA, whereas for Gd-DTPA-D3-PEG, the signal persisted up until 3 h. For DTPA-D3-PEG-CTX, the signal persisted even up until 24 h, illustrating that active targeting can improve the retention of nanomedicine formulations at the target site. This study nicely shows that in spite of the relatively low contrast agent sensitivity of MRI, it can still be used to visualize (and quantify) tumor accumulation, and to discriminate between formulations with different tumor localization kinetics.

A similar approach has been published by Sun et al., who evaluated the ability of CTX-targeted iron oxide-based nanoparticles for visualizing tumor targeting using MRI [95]. In this study, standard amine-modified PEGylated iron oxide nanoparticles (NP-PEG-NH_2),

Europe PMC Funders Author Manuscripts

Europe PMC Funders Author Manuscripts

succinimidyl iodoacetate-modified PEGylated iron oxide nanoparticles (NP-PEG-SIA) and chlorotoxin-targeted PEGylated iron oxide nanoparticles (NP-PEG-CTX) were synthesized, and they were i.v. injected into 9L gliosarcoma-bearing nude mice. As shown in Figure 7B, R_2-relaxivity maps were generated for the various nanoformulations, and the benefit of CTX-mediated tumor targeting could be clearly visualized at 3 h post i.v. injection. The authors were able to demonstrate that the tumor accumulation of both passively and actively targeted iron oxide nanoparticles was relatively heterogeneous, likely reflecting the non-uniform perfusion of tumors, which tend to be more extensively vascularized in their periphery than in their core.

In a follow-up study, CTX-targeted iron oxide-based nanoparticles containing a drug (methotrexate; MTX) to treat 9L gliosarcoma-bearing mice were developed [96]. Intravenously injected MTX-containing NP with (NP-MTX-CTX) and without chlorotoxin (NP-MTX) were compared. Figure 7C gives an overview of the efficacy of active vs. passive targeting, visualized using MRI: the effective accumulation of the targeted probe over time can be clearly delineated using the color-coded T2 maps. On day 1 p.i., there is a considerable decrease in signal intensity in case of both NP-MTX and NP-MTX-CTX, indicating accumulation of the probes in the tumor. On day 3 p.i., however, T2-times were only found to be significantly shortened for actively targeted probe, indicating more efficient retention at the pathological site upon CTX-mediated active targeting. In this regard, it is important to take into account that the initial accumulation of both the passively and the actively targeted nanoparticles in the tumor can be attributed to the EPR effect, in particular to enhanced permeability, and that the incorporation of targeting moieties likely only increases the retention of the probes within tumors. Together, these studies exemplify that even though the contrast agent sensitivity of MRI is relatively low, it can still be used for visualizing and quantifying drug targeting to pathological sites.

The imaging of drug release from nanomedicine formulations, as opposed to the monitoring of their biodistribution and target site accumulation, is arguably the most important application for using MRI in drug delivery research. Since T_1-MR contrast agents depend on access to surrounding water molecules for generating signals, their entrapment in and their release from drug delivery systems can be visualized and quantified using MRI. This is a major difference to radionuclides, which generate similarly strong signals before and after the release from carrier materials. This specific ability of MR contrast agents to be used for visualizing and quantifying drug release was elegantly exploited by De Smet and colleagues, who set out to monitor content release from temperature-sensitive liposomes (TSL) upon high-intensity focused ultrasound (HIFU)-mediated hyperthermia (Figure 8A)[97]. TSL co-encapsulating doxorubicin and a gadolinium-based T_1-contrast agent (Gd-HPDO3A) were synthesized, and i.v. injected into Fisher rats bearing 9L gliosarcoma tumors on their hind limbs. In this study, three animals received a combination of hyperthermia and TSL, and three control animals received TSL without HIFU-mediated hyperthermia. MR T_1-maps were acquired during HIFU treatment, and as shown in Figure 8A, significant T_1-shortening was observed upon TSL administration and HIFU-treatment, indicative of content release. In rat 1, there was distinct decrease in T_1 signal in the whole tumor region, indicating highly efficient release in the whole tumor area. In rat 2, the T_1-decrease was prominent in the periphery and absent in the rim, which was explained (and confirmed via post-mortem

Europe PMC Funders Author Manuscripts

Europe PMC Funders Author Manuscripts

histopathological analysis) on the basis on central tumor necrosis. In the absence of HIFU-treatment, drug delivery and release was found to be minimal under these conditions (Rat 4; Figure 8A). The results obtained for gadolinium release correlated very well with those obtained for doxorubicin release, both intra- and inter-individually: for rat 1, for instance, the intratumoral accumulation of doxorubicin (1.9±0.2 %ID/g) and gadolinium (1.7±0.1 %ID/g) was significantly higher than in rat 2 (0.4±0.04 and 0.4±0.02% ID/g, respectively). In line with previous studies on the MR-monitoring of hyperthermia-mediated drug delivery using TSL, this study therefore nicely exemplifies the potential of using MRI for temporally and spatially analyzing drug release.

Onuki and colleagues recently reported a similarly elegant approach to simultaneously visualize both drug delivery and drug release using multifunctional nanomedicines and a combination of MRI and magnetic resonance spectroscopy (MRS) [98]. Poly(lactic-co-glycolic acid) (PLGA) -based nanoparticles carrying 5-fluorouracil (5-FU), gadolinium-DTPA (Gd-DTPA) and superparamagnetic iron oxide nanoparticles (SPIO; Figure 8B) were prepared, and their properties were evaluated in SCID mice bearing MCF-7 breast cancer xenografts. Upon i.v. injection, the particles exhibited a strong T_2* contrast, generated by the encapsulated SPIO (Figure 8B, row 1), which corresponds to their *in vivo* localization in the tumors. This dark contrast (note that SPIO result in hypointense signals) remained unaltered over time, and both at 30 min and at 2.5 h p.i., the T2*-weighted images clearly demonstrated the presence of PLGA-SPIO nanoparticles within tumors. At the same time, using T_1-mapping, the release of Gd-DTPA from the multifunctional nanomedicine formulations could be observed at 30 min p.i. (note that the T_1-shortening by Gd in this case results in black spots in the T_1 maps). This gadolinium-related signal disappeared at 2.5 h, indicating that the release of gadolinium (and also of 5-FU; which because of its size and hydrophilicity is assumed to be released with similar kinetics as Gd-DTPA) occured relatively early on after i.v. administration, i.e. already within 30 min, and that after this, released Gd-DTPA rapidly diffuses away from the SPIO-containing PLGA-particles, as evidenced by the fact that the signal has already completely disappeared at 2.5 h post i.v. injection. This is further exemplified in the lower right panels in Figure 8B, which simultaneously show nanoparticle localization, and Gd-DTPA (and 5-FU) release, and which provide quantitative feedback (in μM) on the overall amount of GD-DTPA released from this multimodal formulation. These observations, together with the fact that 5-FU release from SPIO-containing nanoparticles can be visualized using MRS (because of SPIO-induced resonance line broadening; see left panel in Figure 8B), exemplify that MRI is highly suited for non-invasively assessing (the kinetics of) drug localization and drug release [98].

Taking these efforts one step further, Delli Castelli and colleagues monitored and modeled both the release, and the intratumoral and intracellular trafficking of contrast agent-labeled liposomes using MRI [99]. To this end, they synthesized two different paramagnetic liposomes. The first formulation contained Gd-HPDO3A, and was used to visualize differences in (sub-) cellular localization and content release using T_1 and T_2 contrast. In this setup, T_2 contrast indicates changes in magnetic susceptibility due to the localization of high amounts of paramagnetic Gd-containing complexes within small volumes, i.e. within

Europe PMC Funders Author Manuscripts

Europe PMC Funders Author Manuscripts

liposomes. The translocation of Gd-HPDO3A from the small volumes within the liposomes to much larger intracellular volumes (e.g. endosomes, lysosomes and cytoplasm) decreases the T_2 signal and, conversely, increases T_1 contrast. Consequently, the changes in T_1 vs. T_2 contrast can be used to detect content release from liposomes. The second liposomal formulation contained the paramagnetic shift agent Tm-DOTMA, which can simultaneously act as a T_2 and as a chemical exchange saturation transfer (CEST) agent. The rationale behind the use of such so-called lipoCEST agents[93] relies on the fact that these formulations behave differently depending on differences in water exchange, thereby enabling the assessment of cellular uptake and intracellular processing of CEST agent-containing liposomes. When intact liposomes are present in the extracellular fluid, the CEST signal is maximal. Upon endocytosis, it substantially decreases, and upon intracellular degradation, it completely vanishes. By using both of these liposome formulations and three different MR imaging protocols (i.e. T_1, T_2 and CEST), the authors elegantly demonstrated the exquisite suitability of MRI for analyzing the cellular uptake, trafficking and processing of liposomes (Figure 8C). In the actual experiments, they injected both liposomal formulations, containing Gd-HPDO3A and Tm-DOTMA, directly into B16 melanoma tumors in mice, and acquired T_1-weighted images (for Gd-HPDO3A), saturation transfer maps (for Tm-DOTMA) and T_2 maps (for both) at several different time points post intratumoral injection. Based on the results obtained, mathematical modeling and quantitative image analysis of six consecutive cellular processing steps (i.e. step a: cellular internalization; step b: uptake into endocytic vesicles; step c: release of the MR contrast agents in endo- and lysosomes; step d: cytosolic entry of the contrast agents; step e: efflux of contrast agents out of the tumor cells; and step f: washout of the agents out of the tumor region, via the vascular system; see left panel in Figure 8C). Using this experimental setup, the authors convincingly showed that it is not only possible to non-invasively assess content release from liposomes using multicontrast MRI, but also to visualize and quantify (the kinetics of) cellular uptake, cellular trafficking and intracellular processing [99].

Recapitulating the above insights and efforts, it can be concluded that MRI is moderately suitable for assessing the biodistribution and the target accumulation of nanomedicines, and highly suitable for monitoring drug release. When taking the official definition of nanomedicine into account, however, i.e. “the application of nanotechnology to medicine, including the use of nanometer-sized carrier materials for facilitating disease diagnosis, disease treatment and treatment monitoring” [1], it seems important to also briefly discuss the potential usefulness of diagnostic nanomedicine materials and non-invasive imaging techniques for assessing the potential of cellular therapies.

MRI has been relatively extensively employed for imaging cell-based vaccination therapies. A pioneering clinical study in this regard has been published De Vries and colleagues, who treated melanoma patients with dendritic cell (DC) vaccines which were labeled both with superparamagnetic iron oxide (SPIO) nanoparticles and with ^{111}In-oxine [100]. Using MRI and scintigraphic imaging, the localization and migration of the DC vaccines in lymph nodes was monitored prior to and two days after lymph node injection. Localization and retention within the primary lymph node as well as migration to several neighboring lymph nodes could be observed (Figure 9A). As DC need to accumulate in lymph nodes for antigen cross-presentation and activation of the immune system, such MR imaging strategies are

Europe PMC Funders Author Manuscripts

Europe PMC Funders Author Manuscripts

considered to be useful for validating that the DC are correctly injected into the lymph node, and also for visualizing and quantifying their retention, and their migration to (neighboring) lymph nodes.

The versatility of MRI also allows for the monitoring of nuclei other than protons, such as 19-fluorine. ^{19}F-MRI is highly attractive, as there is hardly any fluor present in the body (except e.g. in teeth), enabling background-free hot-spot imaging [101]. Ahrens and colleagues recently for the first time showed that ^{19}F-MRI can be used to monitor DC-based vaccines in patients suffering from colorectal adenocarcinoma [101]. The DC were labeled ex vivo with a perfluorocarbon-based nanoemulsion, The nanoemulsion was well-tolerated and efficiently internalized, with each individual DC containing 10^{12}-10^{13} fluorine molecules, sufficient for proper ^{19}F-MRI detection. The labeled DC were intradermally injected into the right leg (near the inguinal lymph node), and MRI was performed at 4 and 24 h after the administration of 10^6 and 10^7 DC. As shown in Figure 9B, 4 h after the injection of 10^7 labeled DC, fluorine hot-spots could be clearly visualized at the injection site. Co-registration with simultaneously acquired ^{1}H-MR images was performed to obtain anatomical information. Quantification of the ^{19}F-MRI signals illustrated that at 4 h after injection, almost all of the 10^7 DC were still present at the site of administration, while at 24 h after injection, approximately half of the DC had migrated away from the site of administration

Also at the preclinical level, MRI has been employed for cell tracking purposes. A nice example of this has been published by Long and colleagues, who monitored the migration of inactivated melanoma cancer cell-based vaccines from the site of injection, via afferent lymphatics, to cytotoxic T cells, for antitumor immunotherapy [102]. To this end, irradiated and inactivated B16 melanoma cells were pre-incubated with SPIO, and combined with B78H1-GM-CSF cells (producing the granulocyte macrophage colony-stimulating factor) in a ratio of 10:1. As depicted schematically in Figure 9C, the mixed cell suspension was intradermally injected into the hind footpads of B16 tumor-bearing C57BL/6 mice. T_2-weighted MRI was performed on a 9.4T scanner equipped with an actively RF-decoupled coil system on a daily basis for 8 consecutive days (Figure 9C). Rapid acquisition with refocused echo (RARE) spin-echo images were captured at selected locations, showing that the cell vaccines gradually drained into the popliteal lymph node (PLN). The localization of the SPIO-labeled cells in the PLN could be clearly visualized (closed arrows in Figure 9C), while in case of non-labeled cells, no MR signal changes were detected (open arrows in Figure 9C). Hypointense lymph nodes could be detected from day 3 onwards, hinting toward DC-mediated transport of the vaccines from the site of injection to the lymph node. Such magnetovaccination strategies, together with advanced MRI detection methods, are considered to be useful for individualizing and improving cell immunotherapies.

A final interesting application of SPIO-containing nanomedicines is based on magnetic drug targeting, in which magnetic fields are used to guide iron oxide-containing nanomaterials to the target site and/or to more efficiently retain them there. A nice example of this has been reported by Clement and colleagues, who synthesized PEGylated magneto-liposomes (ML), and assessed their accumulation in mice bearing tumors on their left and their right flank [103]. ML were intravenously injected via the tail vein and a magnet was placed just besides the

Europe PMC Funders Author Manuscripts

Europe PMC Funders Author Manuscripts

tumor on the right flank. T_1-weighted spin echo, T_2-weighted spin echo, T_2-weighted gradient echo and 3D spoiled gradient echo sequences were applied. A significantly improved accumulation (and/or retention) of ML in the right tumor, which was exposed to the magnet, was observed (Figure 9D) [103]. In the gradient echo images, the difference between the magnetically targeted (right) and the contralateral (left) control tumors could be detected more sensitively detected than in the spin echo images These findings confirm the usefulness of iron oxide-containing nanomedicines for magnetic drug targeting, and they illustrate the suitability of MRI for non-invasively and quantitatively monitoring target site accumulation.

6. OPTICAL IMAGING

In recent years, optical imaging (OI) has been increasingly used for evaluating the biodistribution of nanomedicine formulations. Due to its ease of use (as compared to e.g. PET and SPECT; which involve radiolabeling) and its excellent contrast agent sensitivity, OI is highly suitable for monitoring the target site accumulation of near-infrared fluorophore (NIRF) -labeled nanomedicines, in particular in case of subcutaneous tumors and other superficial lesions, such as inflamed paws in rheumatoid arthritis [104-106].

Fluorescence reflectance imaging (FRI) is by far the most extensively used OI technique employed in drug delivery research. FRI provides reasonably representative information on the localization of NIRF-labeled nanomedicines in superficial lesions, and e.g. enables a semi-quantitative comparison of the accumulation of free vs. nanomedicine-associated fluorophores at the target site, or of different fluorophore-labeled nanomedicine formulations. However, an absolute quantification of probe accumulation (in % injected dose per gram tissue) is impossible using 2D FRI, as is the non-invasive assessment of the overall biodistribution of NIRF-labeled nanomedicines (due to limited light penetration). To overcome these shortcomings, at least to some extent, a 3D OI technique known as fluorescence molecular tomography (FMT) has been developed, which enables a more in-depth and more quantitative assessment of the biodistribution and target site accumulation of NIRF-labeled (nano-) probes [107-109]. However, in spite of the progress made in FMT, a fundamental limitation which applies to all OI techniques is that the fluorescence signals detected often cannot be correctly assigned to specific anatomical regions. This is due to the diffusive scattering of fluorescence signals in the body, as well as to strong light absorption by highly perfused organs and tissues. This inability of OI and in particular of FMT has resulted in the development of hybrid imaging techniques, such as CT-FMT, in which high-resolution micro-CT is used to provide the anatomical information which is otherwise lacking in OI, and in which this anatomical information is used to better reconstruct the fluorescence data obtained using FMT, to more accurately and more representatively visualize and quantify probe accumulation [57;110-112]. Therefore, as in case of PET and SPECT, anatomical CT-based imaging information assists FMT in assigning probe accumulation to certain organs and tissues, and it thereby substantially facilitates probe quantification in non-superficial tissues.

The ease, the versatility and the sensitivity of OI, together with its ability to image multiple fluorophores at the same in the same animal, are the most important pros of this technique.

Europe PMC Funders Author Manuscripts

Europe PMC Funders Author Manuscripts

Problems associated with auto-fluorescence, poor penetration depth and lacking anatomical information are the most important cons. The majority of OI applications relate to preclinical research, but in certain specific cases, e.g. in case of intra-operative imaging, endoscopic imaging and optical mammography, clear evidence has been obtained that this technique can also be translated to the clinic, for facilitating disease diagnosis and for assisting surgeons in removing as much malignant tissue as necessary, but as less healthy tissue as possible (e.g. from the peritoneal cavity, in case of metastatic ovarian carcinoma) [112-116].

As mentioned above, OI has excellent sensitivity for monitoring NIRF-labeled nanomedicines in superficial lesions, but has problems detecting probe accumulation in deeper-seated tissues. It should be realized, however, that the sensitivity of OI narrows down to the order of a few nanomoles (depending upon the type of optical instrument used). Because of this, OI is highly suitable for non-invasively visualizing passive and active drug targeting in case of superficial / subcutaneous tumors. An appealing example has been published by Chen and colleagues [117], who used NIRF-labeled high-density lipoprotein (HDL) nanoparticles to image both tumor vasculature-directed active targeting and EPR-mediated passive targeting (Figure 10A). Specific targeting to blood vessels in tumors was studied using HDL nanoparticles functionalized with RGD-peptides, while EPR-mediated passive tumor targeting was assessed using non-modified and RAD-functionalized HDL nanoparticles. The three different NIRF-labeled nanomedicine formulations were i.v. injected into EW7 Ewing's sarcoma-bearing nude mice, and whole-body OI was performed at several different time points post i.v. injection. From these longitudinal studies, as shown in Figure 10A, it was concluded that in case of RGD-HDL, active targeting to tumor vasculature was evident from 30 min p.i. onwards, and progressed up until 24 h p.i., whereas in case of both controls, i.e. peptide-free and RAD-targeted HDL, accumulation was slower and significantly lower at initial time points. Interestingly, however, at 24 h p.i., somewhat higher overall levels of tumor accumulation were observed for both non-specific probes, indicating that over time, passive targeting dominates over active vascular targeting (at least in this particular tumor model). This study exemplifies the ability of OI to (semi-) quantitatively compare the kinetics of specific probe accumulation in subcutaneous tumors.

Kim and colleagues reported on the use of OI to visualize the accumulation of (hydro-) cyanine-containing chitosan-based nanocarriers in subcutaneous SCC7 xenografts [118]. The rationale behind this study was that tumors generally possess a strong inflammatory component, and that tumor-associated immune responses are characterized by the presence of increased numbers of reactive oxygen species (ROS). The image-guided nanomedicines used in this study contained both cyanine and hydrocyanine, the latter being the reduced form of cyanine. In the presence of ROS, hydrocyanine undergoes an oxidation reaction to yield cyanine, and as exemplified by Figure 10B, this transition could be sensitively detected using OI. Both cyanine- and hydrocyanine-conjugated nanoparticles displayed significant tumor accumulation, but the signal-to-background ratio was clearly better for the ROS-responsive hydrocyanine-containing probes, especially at later time points post i.v. injection. These efforts illustrate the ability of OI to relatively sensitively detect differences in tumor physiology-dependent target site accumulation.

Europe PMC Funders Author Manuscripts

Europe PMC Funders Author Manuscripts

The potential of OI for tumor sentinel lymph node (T-SLN) imaging has been evaluated by Huang et al [62]. Analogous to one of the PET-studies mentioned above (cf. Figure 3D), mesoporous silica particles (MSN) were loaded with the NIRF ZW800, and upon the injection of ZW800-MSN into the footpad of mice bearing metastatic 4T1 tumors, 2D FRI was performed at several times points post i.v. injection, As exemplified by Figure 10C, it was found that there were strong OI signals generated in tumor-associated SLN from 1 h p.i. onwards, which persisted up until 21 d post injection. In case of normal contralateral SLN, on the other hand, the signal was much weaker, and faded much more rapidly. On the basis of this, the authors concluded that OI is suitable for visualizing T-SLN, and they reasoned that this high accumulation of NIRF-labeled MSN in T-SLN can be mainly attributed to strong uptake by tumor-associated inflammatory macrophages [62]. Importantly, however, in Figure 10C, it can also be observed that these whole body OI analyses showed very low levels of ZW800-MSN accumulation in the liver, whereas identical studies performed in the same animals using PET revealed very high levels of liver localization (cf. Figure 3D). Besides demonstrating that OI can be used to detect T-SLN, this study therefore also nicely highlights one of the main shortcomings of whole body OI, i.e. the poor penetration depth of 2D FRI, and the consequent underestimation of NIRF probe accumulation in non-superficial (healthy) organs and tissues[119].

Kunjachan et al. have recently set out to evaluate the potential of using FRI and FMT for visualizing the biodistribution and target site accumulation of a NIRF-labeled passively tumor-targeted polymeric drug carrier [120]. To this end, CD-1 nude mice bearing CT26 colon carcinoma xenografts were i.v. injected with a ~70 kDa-sized pHPMA-based copolymer carrying Dy750 (Figure 11A). 2D FRI was carried out at several early time points post i.v. injection, showing localization in heart and in large blood vessels, thereby confirming the long-circulating properties of this polymeric drug delivery system (Figure 11B) [121;122]. These signals decreased over time, while at 24 h p.i., prominent EPR-mediated tumor accumulation could be observed. In addition, a relatively strong accumulation could be observed in the bladder, indicating kidney clearance (animals were under continuous anesthesia during the first hour, leading to progressive probe accumulation in the bladder), and illustrating that even such relatively large polymeric drug carriers, with an average size above the renal clearance threshold, can be excreted renally [120;123].

To overcome some of the shortcomings associated with 2D FRI for whole-body biodistribution analysis, in particular localization in deeper-seated healthy organs, the authors then established a hybrid imaging approach, in which 3D FMT information was fused with micro-CT images, to enable a quantitative assessment of probe accumulation also in tissues other than superficial tumors. FMT-based optical imaging, in which lasers are used to excite fluorescence in small animals at up to 120 spatial locations, in which detectors record diffuse excitation and emission images, and in which advanced algorithms volumetrically reconstruct the accumulation of NIRF, is generally considered to enable more quantitative and in-depth analyses of OI agents in non-superficial tissues. The major shortcoming of FMT, however, relates to its inability to accurately assign the reconstructed probe accumulation to a given anatomical region and/or organ of interest [111;124;125]. This is considered to be one of the main reasons why 3D FMT has thus far not yet been extensively

Europe PMC Funders Author Manuscripts

Europe PMC Funders Author Manuscripts

used to non-invasively visualize and quantify the whole-body biodistribution of NIRF-labeled nanomedicines.

Extending several pioneering efforts with regard to the combination of FMT with micro-CT for molecular and functional imaging purposes [49;112;126;127], using NIRF-labeled polymeric nanomedicines known to accumulate in tumors both effectively and selectively by means of EPR, Kunjachan et al. showed that hybrid CT-FMT imaging can be employed to non-invasively, more accurately and more meaningfully assess the accumulation of nanomedicine formulations also in tissues other than subcutaneous tumors [120]. To provide proof-of-principle for this, analogous to the efforts mentioned above, pHPMA-Dy750 was administered to CT26 tumor-bearing mice, CT and FMT scans were performed at several different time points p.i., and the CT images were subsequently fused with the respective FMT signals, to obtain fused CT-FMT images. In line with the kinetics of EPR-mediated tumor targeting, the tumor accumulation of pHPMA-Dy750 was very low at 1 h p.i., but very prominent at 72 h (as shown by the circles in the left panel of Figure 11C). To at the same time enable analyses on probe accumulation in healthy organs, several physiologically relevant organs were 3D segmented on the basis of the CT scans, and the pHPMA-Dy750-based FMT signals were fused with these images (middle and right panels in Figure 11C). The robustness of the methodology for 3D organ segmentation was validated, and *in vivo* CT-FMT quantification of the healthy organ accumulation indicated that the results were well in line with previous studies using similarly sized radiolabeled pHPMA-based nanocarriers [122;128]. Consequently, these efforts convincingly demonstrate that combining micro-CT with FMT enables more informative, more realistic and more meaningful OI studies on the biodistribution of NIRF-labeled nanomedicine formulations.

Another ‘hybrid’ optical imaging technique that has attracted increasing attention in recent years is photoacoustic imaging (PAI) [129-131]. PAI is based on the illumination of (light-absorbing molecules and nanoprobes in) tissues using pulsed laser light, on their energy absorption and heat generation, and on the resulting thermoelastic expansion of tissues. The latter can be picked up using ultrasound detectors. PAI combines the multispectral possibilities of pulsed laser light illumination with the enhanced penetration depth and the high sensitivity of ultrasound imaging. Several recent studies have reported on the potential of PAI, e.g. for detecting tumors and monitoring antitumor responses [132-136], for sentinel lymph node detection [137-139], and for imaging inflammation [140-142] and vascularization[143-145]. PAI setups such as multi-spectral optoacoustic tomography (MSOT) allow for the discrimination of probe-specific signals from those of background signals and they enable the quantitative assessment of endogenous (e.g. hemoglobin, desoxyhemoglobin and melanin) and exogenous (e.g. indocyanine green, methylene blue and porphyrin) contrast agents [146-148]. Several different nanomedicine formulations have also already been employed for PAI. These e.g. include gold nanoparticles (e.g. nanospheres, nanoshells, nanorods, nanocages, etc) [149-155], carbon nanotubes [156-158] and melanin-based polymers and nanoparticles [159-161]. An interesting example in this regard has recently been reported by Kircher and colleagues, who showed that nanoparticles consisting of a gold core (for PAI), a Raman-active layer (for surface-enhanced Raman-spectroscopy; SERS), and a gadolinium-based coating (for MRI) can be employed for trimodal tumor imaging and image-guided

Europe PMC Funders Author Manuscripts

Europe PMC Funders Author Manuscripts

tumor resection[162]. These so-called MPR (magnetic resonance-photoacoustic-Raman) nanoparticles were used to macroscopically identify tumors using MRI, to more accurately localize deep-seated tumors using PAI, and to perform microscopical fine margin tumor resection using SERS. Such studies, alongside efforts to further improve and establish PAI as a clinically useful non-invasive imaging modality, will surely lead to many more publication in which (hybrid) nanoparticles are employed for photoacoustic imaging purposes in the next couple of years.

Besides for monitoring the biodistribution and the target site accumulation of fluorophore-labeled nanocarriers using CT-FMT, and for facilitating fine-margin tumor resection using gold nanoparticles and PAI, OI is also highly useful for assessing the potential of nucleic acid-containing nanomedicine formulations, employed e.g. for gene therapy or for siRNA delivery purposes. An example of the latter has been reported by Medarova and colleagues, who used Cy5.5-labeled iron oxide-based magnetic nanoparticles (MN) containing siRNA directed against GFP (Figure 12A), and who tested them in nude mice bearing subcutaneous GFP- and RFP-transfected tumors, to monitor both tumor-directed drug delivery and gene silencing efficacy [163]. Initially, the delivery of MN-NIRF-siGFP to tumors was evaluated, by means of both MRI and OI, showing relatively efficient EPR-mediated drug targeting, which much higher levels in tumors than in healthy muscle tissue (Figure 12A). The efficacy and specificity of gene silencing were analyzed at 48 h p.i., showing that MN-NIRF-siGFP substantially suppressed GFP expression in GFP-transfected tumors, but did not affect RFP-transfected tumors (lower left panels in Figure 12B). These findings were validated using ex vivo OI, confirming not only significant tumor accumulation of MN-NIRF-siGFP (independent of tumor type; right panels in Figure 12A), but also effective and selective GFP silencing (dependent of tumor type; right panels in Figure 12B). This study therefore nicely illustrates the suitability of OI for non-invasively assessing the potential of siRNA-containing nanomedicine formulations.

Using bioluminescence (BLI) -based OI to assess the efficiency of gene delivery, Navarro and colleagues compared generation-5 PAMAM dendrimers to linear PEI polymers [164]. Both gene delivery systems contained plasmid DNA encoding for luciferase. Effective transfection of (tumor) cells with luciferase enables the local activation of luciferin (which is co-injected intraperitoneally), generating a luminescent signal which can be sensitively detected using BLI-based OI. To assess the potential of G5-PAMAM dendrimers vs. L-PEI polymers for DNA delivery and cancer cell transfection, the formulations were i.v. injected into mice bearing subcutaneous Neuro 2A tumors. As shown in Figure 12C, consistent with many previous reports, i.v. injected L-PEI resulted in very high transgene expression levels in the lungs of mice, whereas the luminescent signal generated in tumors was relatively low. G5-PAMAM-dendrimers, on the other hand, resulted in much lower levels of off-target gene expression in the lung, and in much higher levels of gene expression in tumors. These exemplary efforts, together with the large number of similar studies in which plasmid DNA encoding for luciferase was used to assess the efficacy of gene therapy, demonstrate the suitability of BLI-based OI for non-invasively monitoring nucleic acid delivery.

Europe PMC Funders Author Manuscripts

Europe PMC Funders Author Manuscripts

7. ULTRASOUND IMAGING

Ultrasound (US) imaging is based on the principle that back-scattered signals from acoustic waves vary depending on reflection by different tissues (as well as by US contrast agents). US can convey a clear anatomical depiction of the tissue or area of interest, with high temporal and spatial resolution. US is a very versatile technique, which is inexpensive, fast, well-established and routinely used in the clinic. Some of the drawbacks associated with US include operator-dependency, inability to perform whole body imaging, and limitations with regard to the versatility of the contrast agents that can be used (i.e. 1-5 μm-sized gas- or air-filled microbubbles; which remain exclusively intravascular).

In recent years, more and more studies have been reported in which US is used for drug delivery purposes. These primarily include combinations of US with microbubble (MB) and nanobubble (NB) based formulations, which can either be co-loaded with drugs, or administered separately, to enhance extravasation, penetration and/or cellular internalization [165-167]. The latter process, i.e. cell membrane permeation and increased internalization, is generally referred to as sonoporation, and has been extensively used for gene delivery purposes [168;169]. The principle for sonoporation, as well as for enhanced extravasation and penetration, relies on stably oscillating MB, as well as on the jet streams and shock waves resulting from the destruction of MB. Depending on their composition and on the applied US powers and frequencies, MB can either cavitate stably (i.e. non-destructively) or inertially (i.e. destructively). Both types of cavitation can lead to vascular and cellular membrane disruption, via the oscillation-dependent opening of tight junctions, acoustic microstreaming and shock wave-generation [83;86]. Furthermore, MB- and NB-based formulations have been shown to be useful for perfusion monitoring, which enables non-invasive imaging of the circulating properties of these formulations, as well as the longitudinal assessment of the efficacy of pro- or anti-angiogenic therapies [170].

An exemplary study showing that nanoformulations and US can be used for perfusion imaging was published by Wheatley and colleagues, who developed nanobubbles termed ST-68N, composed of a span-60 and tween-80 surfactant-shell, and monitored their fate in white New Zealand rabbits [171]. *In vivo* power Doppler US images were obtained before and after injection (upper panels in Figure 13A), showing significant signal enhancement in the kidneys at 1.5 min p.i., because of the presence of NB in renal blood vessels. This notion was confirmed via pulse-inversion harmonic images (lower panels in Figure 13A), demonstrating the suitability of US plus NB for non-invasive perfusion monitoring.

In another study, reported by Rapoport and colleagues, US was used to non-invasively visualize doxorubicin- and perfluoropentane-containing PEG-PLLA nanobubbles [172]. Cavitation analyses, based on their oscillation, growth and collapse of were performed, as well as studies in nude mice bearing MDA-MB-231 breast cancer and A2780 ovarian cancer xenografts, which were intratumorally and intravenously injected with these so-called nanodroplets. The left panels in Figure 13B show the US images generated in an MDA-MB-231 tumor prior to and at 4 h after i.t. injection. As expected, strong echo signals were generated immediately after injection, and they persisted within the tumors for days. The size of echo-producing entities was found to be much larger than the size of the injected NB,

Europe PMC Funders Author Manuscripts

Europe PMC Funders Author Manuscripts

indicating intratumoral coalescence into MB. Coalescence was confirmed by tumor imaging upon the i.v. administration of the nanodroplets. As shown in the right panels in Figure 13B, at 4.5 h after injection, highly echogenic signals were observed in tumors, as a result of the extravasation of the NB through leaky vessels and subsequent coalescence into MB. In healthy tissues with an intact endothelial lining, on the other hand, such as the kidney, no echogenicity could be detected (bottom right panel in Figure 13B). Results were validated in A2780 ovarian carcinoma xenografts, and extended by therapeutic analyses showing that doxorubicin-loaded nano/microbubbles were much more effective when combined with US [172], thereby exemplifying the ability of using US for drug delivery applications.

Using MB loaded with model drugs within their shell and targeted to tumor blood vessels via anti-VEGFR2 antibodies, Fokong et al. confirmed the suitability of US for simultaneously monitoring tumor accumulation and enhancing drug delivery [173]. To this end, as exemplified by Figures 14A-B, they evaluated 1-step and 2-step loading strategies to entrap the model drugs Rhodamine-B and Coumarin-6 into the shell of poly(n-butyl cyanoacrylate) (PBCA) MB. The MB were then surface-hydrolyzed, conjugated to streptavidin and functionalized with biotinylated antibodies directed toward VEGFR2, which is highly overexpressed on angiogenic tumor blood vessels. Fluorophore entrapment was validated using two-photon laser scanning microscopy and quantified using TECAN measurements, and showed that up to $2*10^6$ model drug molecules can be entrapped within the shell of a single MB. The authors furthermore demonstrated that upon US-mediated MB destruction, ~80% of the shell-incorporated models drugs are released. Upon injecting these MB i.v., US imaging showed that they efficiently localized to tumors via VEGFR2-binding (Figure 14C), and exposure to destructive US pulses resulted in efficient content release within tumors and tumor blood vessels. Fluorescence microscopy analyses also hinted toward enhanced extravasation and penetration of the model drugs (Figure 14D). Consequently, such theranostic MB are considered to hold significant potential for image-guided, targeted and triggered drug delivery, in particular of highly toxic compounds, for which prolonged and systemic exposure should by be prevented.

As already pointed out above, the combination of MB plus US is more and more implemented to improve drug delivery across biological barriers. Upon US-mediated MB oscillation and destruction, acoustic forces and microjets are generated, resulting in the loosening of the endothelial lining and/or the permeation of cellular membranes, thereby facilitating the transport of drugs (and contrast agents) from the intravascular compartment into the interstitial and/or intracellular compartment. This phenomenon, coined sonoporation, is not only used to enhance the efficacy of poorly internalized agents, such as nucleic acids, into cells, but also to promote drug delivery across the BBB, and (deeper) into tumors [168;170;174-182]. If used as such, US is only employed for interventional purposes, i.e. not for imaging, indicating that other non-invasive imaging techniques, such as SPECT, MRI and OI, are necessary to non-invasively and longitudinally assess the *in vivo* efficacy of sonoporation. A nice example of this has been provided by Deckers and colleagues, who used 2D FRI to monitor the impact of MB- plus US-mediated sonoporation on the uptake and retention of the fluorescent model drug TOTO-3 in subcutaneous mouse tumors [167]. TOTO-3 is a cell-impermeable and nucleus-specific near-infrared fluorophore, and is

Europe PMC Funders Author Manuscripts

Europe PMC Funders Author Manuscripts

dubbed to be a ‘smart’ agent because it shows a 100-1000-fold enhancement in signal intensity upon DNA binding. Mice bearing tumors on both hind limbs were co-injected with TOTO-3 and MB (both administered intratumorally into both tumors), and US was subsequently applied only to the right tumor (i.e. the lower tumor in Figure 15A). Before and at several different time points after the treatment with destructive US pulses, TOTO-3-associated fluorescence was visualized and quantified. As shown in the longitudinal FRI scans in Figure 15A, no signal was observed before probe administration and US treatment (panel 1), whereas immediately after probe injection, a very strong signal was obtained for both tumors (panel 2). Two and four hours later, however, a strong signal only persisted in the US-treated tumors, indicative of a substantially enhanced internalization of TOTO-3 (panels 3-4). These findings convincingly demonstrate that sonoporation, i.e. the combination of US and MB, can be used to improve the cellular uptake of poorly internalized (model) drugs.

Besides for imaging, US can also be used for therapeutic purposes. Such applications mainly include thrombolysis and hyperthermia treatment. The latter can either refer to high-intensity focused ultrasound (HIFU; resulting in temperature increases up to 70° C; for ablation purposes), or to low-intensity US (for mild hyperthermia; and drug release from temperature-sensitive liposomes). HIFU is clinically used for the ablation of benign tumors, such as uterine fibroids, and trials are currently ongoing in cancer patients, e.g. for breast tumors and for the palliative treatment of bone metastases [183-185]. Recently, it has been shown that pulsed HIFU can also be employed to non-invasively enhance the delivery of various diagnostic and therapeutic agents via non-thermal mechanisms [186;187]. Acoustic cavitation is one of such non-thermal mechanisms for inducing temporary changes in biological tissues or vessels to enhance drug delivery [188]. Hancock and colleagues recently reported a setup in which pulsed HIFU was used to enhance the systemic delivery of fluorescently labeled lectin and polystyrene nanospheres [189]. Immediately upon HIFU exposure (i.e. 10-15 min afterwards), both probes were i.v. injected, and 30 min later, the mice were sacrificed, and the skin covering treated and control muscle regions was removed. The animals were then analyzed under an inverted fluorescence microscope, and digital images were captured. As shown in Figure 15B, HIFU-treated muscle tissue showed much broader and much more intense signals than control muscle tissue, with clear extravascular signals both for fluorescently labeled lectin and for fluorescent nanospheres, indicative of efficient US-mediated sonoporation. These findings illustrate the applicability of HIFU-based techniques for enabling and/or enhancing the extravasation and/or retention of nanomedicine formulations at the target site.

A final interesting application of US relates to its ability to generate heat in deep-seated tissues. In such setups, focused US can be used to induce mild hyperthermia, and thereby drug release from the temperature-sensitive nanocarriers [167;186;190]. Negussie and colleagues, for instance, prepared low-temperature-sensitive liposomes (TSL; responsive at 40-41 °C) co-loaded with doxorubicin and with the MR contrast agent Gd-HPDO3A, and demonstrated that MR-guided US can be used to mediate and monitor temperature-triggered drug and contrast agent release in rabbits bearing VX2 sarcoma tumors [186] (Figure 15C). MR images were obtained before (panel 1) and after (panel 2) the injection of the TSL. The perfusion of TSL through large blood vessels in periphery and core of the tumor could be

Europe PMC Funders Author Manuscripts

Europe PMC Funders Author Manuscripts

clearly visualized (panel 2). As shown in panel 3, upon applying US-mediated hyperthermia, a temperature map for the tumor region can be obtained using MR-thermometry, which provides valuable feedback on the efficiency of heating. After four 10-minute heating intervals, Gd-HPDO3A release in the tumor tissue was evident from the T1-weighted MR image (panel 4), and the spatial location of this nicely corresponded to the most intensely heated area (cf. panels 3 and 4). This study elegantly exemplifies the potential of using MR-guided US for inducing and imaging drug release from temperature-sensitive nanomedicine formulations.

8. TRANSLATIONAL IMAGING

Besides for preclinical purposes, non-invasive imaging is also highly useful for facilitating the clinical translation of nanomedicines. It can e.g. be employed to visualize and quantify how efficient passive or active drug targeting is in individual patients, and to - on the basis of this - preselect patients likely to respond to nanomedicine-based chemotherapeutic interventions (and to exclude those unlikely to respond) [23,191]. In addition, it can be used to visualize the off-target localization of nanomedicines, e.g. in potentially endangered healthy tissues, which under certain circumstances might lead to exclusion from (further) targeted treatment. Moreover, by systematically integrating imaging also during follow-up, and by closely monitoring therapeutic responses upon nanomedicine treatment, clinical decision making can be facilitated and improved, as decisions on whether or not to (dis-) continue treatment, and on whether or not to adjust drug doses, can be made relatively early on.

Consequently, combining drug targeting and imaging might be very valuable for individualizing nano-chemotherapeutic treatments, and it provides a rational basis for personalized nanomedicine[191]. A pioneering study in this regard has been published by Harrington and colleagues, who visualized and quantified EPR-mediated passive tumor targeting using ^{111}In-labeled PEGylated liposomes in patients suffering from different types of tumors [192]. The liposomes were administered to patients with squamous lung carcinoma, head and neck cancer, and breast cancer, using whole body gamma camera imaging and SPECT. As shown in Figure 16A, relatively efficient passive drug targeting was observed for the former two malignancies. Overall, the levels of accumulation varied from 2.7 to 53.0 %ID/kg of tumor. The highest accumulation was observed in head and neck cancer (33±16 %ID/kg), intermediate accumulation was noted in lung carcinoma (18±6 %ID/kg), and relatively low levels were detected in breast cancer (5±3 %ID/kg). These numbers indicate that there was a relatively high degree of heterogeneity in the tumor uptake of liposomes, both between patients with different types of tumors, and also between patients with the same type of tumor. Besides in tumors, significant accumulation was also observed in liver and spleen, with values being approximately five-fold higher for the former than for the latter (34±15 vs. 7±2 %ID/kg, respectively). The authors finally also carried out longitudinal gamma camera imaging in a single patient affected by AIDS-related Kaposi sarcoma (KS), exemplifying very strong accumulation in both primary and metastatic KS lesions (right panel in Figure 16A). In good agreement with this, PEGylated liposomes containing doxorubicin are known to be highly effective for treating Kaposi sarcoma [192].

Europe PMC Funders Author Manuscripts

Europe PMC Funders Author Manuscripts

At about the same time, Seymour and colleagues for the first time visualized active nanomedicine-mediated drug targeting in patients [193]. They prepared pHPMA-based polymeric drug carrier functionalized with doxorubicin, tyrosinamide (for radiolabeling) and galactosamine (for targeting to asialoglycoprotein receptors; which are overexpressed by hepatocytes), and used planar gamma camera and SPECT imaging to monitor drug targeting to hepatocellular carcinomas. The biodistribution of this actively targeted polymer-drug conjugate, which was termed PK2, was compared to PK1, which lacks galactosamine, showing highly efficient liver targeting in case of the former (left panels in Figure 16B). However, upon imaging the intra-hepatic distribution of PK2, it was found that most of the conjugate accumulated in healthy liver tissue, rather than in tumors (right panels in Figure 16B), explaining - at least in part - why PK2 treatment resulted is relatively disappointing response rates.

Recently, in a bench-to-bedside approach, Hrkach and colleagues prepared actively targeted PLGA-based nanoparticles (TNP) containing docetaxel (DTXL), and evaluated the efficacy of the most optimal formulation(s) in vitro, in vivo and in patients [194]. DTXL-TNP was targeted to the prostate-specific membrane antigen (PSMA), using the targeting ligand ACUPA, and its clinical efficacy was monitored using contrast-enhanced CT imaging. As evidenced by Figure 16C, in a patient suffering from cholangiocarcinoma with metastatic lung lesions, as well as in a patient suffering from tonsillar cancer, non-invasive imaging provided relatively early insights on the efficacy of the intervention, with already within 1.5 months after the start of the therapy, clear indications for efficient disease treatment. This study illustrates that besides for monitoring nanomedicine biodistribution and target site accumulation, non-invasive imaging is also highly useful for longitudinal treatment monitoring.

The above efforts exemplify the potential of combining drug targeting and imaging in the clinical situation. By labeling nanomedicines, and by subjecting patients to gamma camera, PET and SPECT imaging, non-invasive and quantitative information on the pharmacokinetics, biodistribution, target site accumulation and off-target localization of the formulations can be obtained. As depicted schematically in Figure 17, this non-invasive imaging information can be used to decide whether or not to treat patients with nanomedicines, and it might thereby provide a rational framework for personalizing nanomedicine treatments. It is reasonable to assume in this regard, that if the amounts accumulating in tumors (and/or metastases) are high, that targeted treatments would then be more efficient than if hardly any fraction of the i.v. administered dose accumulates at the target site (first patient selection step; Figure 17A). In case of the former, patients can then be confidently treated with the nanomedicine formulation in question, whereas in case of the latter, it might be wise to treat them with other chemotherapeutic agents already from day 2 onwards. In addition, if whole-body imaging shows that besides in tumors, high levels of the nanomedicine formulation also (unexpectedly) strongly accumulate in potentially endangered healthy tissues, e.g. because of co-morbidities, then such patients can be excluded from nanomedicine treatment, to minimize the risk of developing severe or even life-threatening side effects. Furthermore, by at the same time also including ‘standard’ imaging-based diagnostic procedures during follow-up, important information on potential treatment responses can be obtained (second patient selection step; Figure 17A), which can

Europe PMC Funders Author Manuscripts

be useful for relatively rapid decision making with regard to whether or not to continue nanotherapy, and whether or not to adjust drug doses.

Finally, it is important to keep in mind in this regard that non-invasive imaging may be particularly useful in case of metastatic disease [195]. Using e.g. fluorodeoxyglucose (FDG) - based PET scans, metastases can be sensitively and accurately localized in patients. By subsequently performing PET or SPECT scans with radionuclide-labeled nanomedicines, information can be obtained on the accumulation of these formulations in both primary tumors and metastases, and treatment protocols can be adapted accordingly. As exemplified by Figure 17B, in such setups, it seems obvious that if all lesions show significant nanomedicine uptake, that patients should then be treated with the nanomedicine formulation in question. Conversely, if all - or the vast majority of - lesions do not accumulate nanocarriers efficiently, it seems logical not to treat patients with nanomedicines, but with alternative therapies, such as surgery, radiotherapy, standard chemotherapy, experimental chemotherapy and/or immunotherapy. Consequently, in spite of the fact that not much is known yet about the potential of nanomedicines for targeting and treating metastasis [196], non-invasive imaging appears to be very valuable for individualizing and improving the therapy of metastatic cancers. Taken together, we believe that theranostic concepts, in which drug targeting and imaging are intimately combined, are highly useful for personalizing nanomedicine-based (chemo-) therapeutic interventions, facilitating both clinical translation and clinical practice, and ensuring that the right (nano-) drug is given to the right patient at the right dose and at the right time.

9. CONCLUSION

Non-invasive imaging is used for many different (pre-) clinical purposes, ranging from disease diagnosis, disease staging and treatment monitoring, to the visualization and quantification of nanomedicine-mediated drug targeting and (triggered) drug release. Several different imaging techniques - such as PET, SPECT, CT, MRI, OI and US - are available for monitoring the biodistribution, the target site accumulation and the off-target localization of nanomedicines, and each of these modalities has its own specific pros and cons. The successful use of non-invasive imaging techniques to a large extent depends on choosing the right imaging modality and the right contrast agent for the right application. Several (bio-) medical questions can be accurately and quantitatively resolved using only one imaging modality, while others require a combination of two different imaging techniques (e.g. hybrid PET-CT, PET-MRI, SPECT-CT and CT-FMT). Consequently, in order to optimally integrate non-invasive imaging in drug delivery research, and to facilitate the combination of drug targeting and imaging to individualize and improve nanomedicine treatments, it is important to keep the specific advantages, limitations and applications of each of these imaging techniques in mind.

ACKNOWLEDGEMENTS

This work was supported by the European Research Council (ERC Starting Grant 309495: NeoNaNo), by the European Union (COST-Action TD1004-Nanotheragnostics), by the German Research Foundation (DFG; LA2937/1-2), and by the German Federal State of North Rhine Westphalia (NRW; HighTech.NRW / EU-Ziel 2-Programm (EFRE); ForSaTum).

Europe PMC Funders Author Manuscripts

Europe PMC Funders Author Manuscripts

BIOGRAPHIES

Sijumon Kunjachan

Sijumon Kunjachan studied Pharmaceutics at Mahatma Gandhi University, India and did his research training at Central Drug Research Institute and Indian Institute of Technology Kanpur. He obtained his PhD (experimental medicine) from RWTH Aachen University in 2013. He worked on multidrug resistance, on optical imaging, and on several different passively and actively targeted nanomedicine formulations for image-guided drug delivery to tumors. He subsequently joined the Department of Radiation Oncology at Harvard Medical School (Brigham and Women's Hospital and Dana-Farber Cancer Institute) as a postdoctoral scientist. His main research interests include nanomedicine, imaging, radiation therapy and cancer therapeutics.

Josef Ehling

Josef Ehling studied medicine at RWTH Aachen University and received his MD in pathology in 2010. After working as a physician at the Institute of Pathology for three years, he became a junior scientist at the Institute for Experimental Molecular Imaging (ExMI) of RWTH Aachen University Clinic. His research interests include the design and evaluation of novel contrast agents and imaging techniques for the non-invasive and quantitative assessment of the microenvironment, including e.g. the aberrant deposition of ECM proteins and pathological angiogenesis in tumors and in liver and kidney fibrosis.

Gert Storm

Europe PMC Funders Author Manuscripts

Gert Storm obtained his PhD degree in 1987 at the Department of Pharmaceutics at Utrecht University. He holds professor positions at Utrecht University (Targeted Drug Delivery), University Medical Centre Utrecht (Imaging-Guided Drug Delivery) and University of Twente (Targeted Therapeutics). He is author/co-author of more than 450 original articles, reviews and book chapters. His primary research interests are in the fields of biopharmaceutics and drug targeting. He received several awards for his activities as translational pharmaceutical scientist. He is included in the 2014 list of The World's Most Influential Scientific Minds of Thomson Reuters (Highly Cited Researchers 2014, period 2002-2012).

Fabian Kiessling

Fabian Kiessling completed his MD thesis at Heidelberg University in 2001. He subsequently worked at the Departments of Radiology and Medical Physics in Radiology at the German Cancer Research Center in Heidelberg, where he headed the Molecular Imaging Group. In parallel, he did his clinical training at the University of Heidelberg and received his board certification as a Radiologist in 2007. He is the author of over 200 scientific publications and book chapters, edited two books and received several research awards. Since 2008, he has been the chair of the Institute for Experimental Molecular Imaging at RWTH Aachen University. With a particular focus on angiogenesis, the aim of his research is the development of novel diagnostic probes and imaging tools for disease-specific diagnosis and therapy monitoring.

Twan Lammers

Europe PMC Funders Author Manuscripts

Europe PMC Funders Author Manuscripts

Twan Lammers obtained a DSc degree in Radiation Oncology from Heidelberg University in 2008 and a PhD degree in Pharmaceutics from Utrecht University in 2009. In the same year, he started the Nanomedicine and Theranostics group at the Institute for Experimental Molecular Imaging at the University Clinic of RWTH Aachen. In 2014, he was promoted to professor of Nanomedicine and Theranostics at RWTH Aachen. Since 2012, he has also worked as a part-time assistant professor at the Department of Targeted Therapeutics at the University of Twente. He published over 100 research articles and reviews, and received several awards. His primary research interests include drug targeting to tumors, image-guided drug delivery and tumor-targeted combination therapies.

References

(1). European Science Foundation's Forward Look Nanomedicine: An EMRC Consensus Opinion. European Science Foundation; 2005. www.esf.org

(2). Kataoka K, Harada A, Nagasaki Y. Block Copolymer Micelles for Drug Delivery: Design, Characterization and Biological Significance. Adv. Drug Deliv. Rev. 2001; 47:113–131. [PubMed: 11251249]

(3). Panyam J, Labhasetwar V. Biodegradable Nanoparticles for Drug and Gene Delivery to Cells and Tissue. Adv. Drug Deliv. Rev. 2003; 55:329–347. [PubMed: 12628320]

(4). Torchilin VP. Recent Advances With Liposomes As Pharmaceutical Carriers. Nat. Rev. Drug Discovery. 2005; 4:145–160. [PubMed: 15688077]

(5). Duncan R. Polymer Conjugates As Anticancer Nanomedicines. Nat. Rev. Cancer. 2006; 6:688–701. [PubMed: 16900224]

(6). Langer R. Drug Delivery and Targeting. Nature. 1998; 392:5–10. [PubMed: 9579855]

(7). Allen TM, Cullis PR. Drug Delivery Systems: Entering the Mainstream. Science. 2004; 303:1818–1822. [PubMed: 15031496]

(8). Peer D, Karp JM, Hong S, Farokhzad OC, Margalit R, Langer R. Nanocarriers As an Emerging Platform for Cancer Therapy. Nat. Nanotechnol. 2007; 2:751–760. [PubMed: 18654426]

(9). Davis ME, Chen Z, Shin DM. Nanoparticle Therapeutics: an Emerging Treatment Modality for Cancer. Nat. Rev. Drug Discovery. 2008; 7:771–782. [PubMed: 18758474]

(10). Liu Y, Miyoshi H, Nakamura M. Nanomedicine for Drug Delivery and Imaging: a Promising Avenue for Cancer Therapy and Diagnosis Using Targeted Functional Nanoparticles. Int. J. Cancer. 2007; 120:2527–2537. [PubMed: 17390371]

(11). Lammers T. Improving the Efficacy of Combined Modality Anticancer Therapy Using HPMA Copolymer-Based Nanomedicine Formulations. Adv. Drug Deliv. Rev. 2010; 62:203–230. [PubMed: 19951732]

(12). Lammers T, Kiessling F, Hennink WE, Storm G. Drug Targeting to Tumors: Principles, Pitfalls and (Pre-) Clinical Progress. J. Controlled Release. 2012; 161:175–187.

(13). Duncan R, Gaspar R. Nanomedicine(s) Under the Microscope. Mol. Pharmaceutics. 2011; 8:2101–2141.

(14). Louie A. Multimodality Imaging Probes: Design and Challenges. Chem. Rev. 2010:3146–3195. [PubMed: 20225900]

Europe PMC Funders Author Manuscripts

(15). MacKay JA, Li Z. Theranostic Agents That Co-Deliver Therapeutic and Imaging Agents? Adv. Drug Delivery Rev. 2010; 62:1003–1004.

(16). Sumer B, Gao J. Theranostic Nanomedicine for Cancer. Nanomedicine (London, U.K.). 2008; 3:137–140. [PubMed: 18373419]

(17). Janib SM, Moses AS, MacKay JA. Imaging and Drug Delivery Using Theranostic Nanoparticles. Adv. Drug Deliv. Rev. 2010; 62:1052–1063. [PubMed: 20709124]

(18). Lammers T, Subr V, Ulbrich K, Hennink WE, Storm G, Kiessling F. Polymeric Nanomedicines for Image-Guided Drug Delivery and Tumor-Targeted Combination Therapy. Nano Today. 2010; 5:197–212.

(19). Xie J, Lee S, Chen X. Nanoparticle-Based Theranostic Agents. Adv. Drug Delivery Rev. 2010; 62:1064–1079.

(20). Chen X, Gambhir SS, Cheon J. Theranostic Nanomedicine. Acc. Chem. Res. 2011; 44:841. [PubMed: 22004477]

(21). Jokerst JV, Gambhir SS. Molecular Imaging With Theranostic Nanoparticles. Acc. Chem. Res. 2011; 44:1050–1060. [PubMed: 21919457]

(22). Terreno E, Uggeri F, Aime S. Image Guided Therapy: the Advent of Theranostic Agents. J. Controlled Release. 2012; 161:328–337.

(23). Lammers T, Aime S, Hennink WE, Storm G, Kiessling F. Theranostic Nanomedicine. Acc. Chem. Res. 2011; 44:1029–1038. [PubMed: 21545096]

(24). Kunjachan S, Jayapaul J, Mertens ME, Storm G, Kiessling F, Lammers T. Theranostic Systems and Strategies for Monitoring Nanomedicine-Mediated Drug Targeting. Curr. Pharm. Biotechnol. 2012; 13:609–622. [PubMed: 22214503]

(25). Cormode DP, Skajaa T, Fayad ZA, Mulder WJM. Nanotechnology in Medical Imaging Probe Design and Applications. Arterioscler. Thromb. Vasc. Biol. 2009; 29:992–1000. [PubMed: 19057023]

(26). Bar-Shalom R, Valdivia AY, Blaufox MD. PET Imaging in Oncology. Semin. Nucl. Med. 2000; 30:150–185. [PubMed: 10928381]

(27). Chopra, A. Molecular Imaging and Contrast Agent Database (MICAD). 2004. [74As]-Labeled Monoclonal Antibody Against Anionic Phospholipids.

(28). Pressly ED, Rossin R, Hagooly A, Fukukawa K, Messmore BW, Welch MJ, Wooley KL, Lamm MS, Hule RA, Pochan DJ, Hawker CJ. Structural Effects on the Biodistribution and Positron Emission Tomography (PET) Imaging of Well-Defined (64)Cu-Labeled Nanoparticles Comprised of Amphiphilic Block Graft Copolymers. Biomacromolecules. 2007; 8:3126–3134. [PubMed: 17880180]

(29). Devaraj NK, Keliher EJ, Thurber GM, Nahrendorf M, Weissleder R. 18F Labeled Nanoparticles for in Vivo PET-CT Imaging. Bioconjugate Chem. 2009; 20:397–401.

(30). Herth MM, Barz M, Jahn M, Zentel R, Rosch F. 72/74As-Labeling of HPMA Based Polymers for Long-Term in Vivo PET Imaging. Bioorg. Med. Chem Lett. 2010; 20:5454–5458. [PubMed: 20709549]

(31). Roesch F. Scandium-44: Benefits of a Long-Lived PET Radionuclide Available From the (44)Ti/(44)Sc Generator System. Curr. Radiopharm. 2012; 5:187–201. [PubMed: 22642388]

(32). Muller C, Bunka M, Haller S, Koster U, Groehn V, Bernhardt P, van der Meulen N, Turler A, Schibli R. Promising Prospects for 44Sc-/47Sc-Based Theragnostics: Application of 47Sc for Radionuclide Tumor Therapy in Mice. J. Nucl. Med. 2014; 55:1658–1664. [PubMed: 25034091]

(33). Chakravarty R, Goel S, Valdovinos HF, Hernandez R, Hong H, Nickles RJ, Cai W. Matching the Decay Half-Life With the Biological Half-Life: ImmunoPET Imaging With (44)Sc-Labeled Cetuximab Fab Fragment. Bioconjugate Chem. 2014; 25:2197–2204.

(34). Gambhir SS. Molecular Imaging of Cancer With Positron Emission Tomography. Nat. Rev. Cancer. 2002; 2:683–693. [PubMed: 12209157]

(35). Li KCP, Pandit SD, Guccione S, Bednarski MD. Molecular Imaging Applications in Nanomedicine. Biomed. Microdevices. 2004; 6:113–116. [PubMed: 15320632]

(36). Cai W, Chen X. Nanoplatforms for Targeted Molecular Imaging in Living Subjects. Small. 2007; 3:1840–1854. [PubMed: 17943716]

Europe PMC Funders Author Manuscripts

(37). Ping Li W, Meyer LA, Capretto DA, Sherman CD, Anderson CJ. Receptor-Binding, Biodistribution, and Metabolism Studies of 64 Cu-DOTA-Cetuximab, a PET-Imaging Agent for Epidermal Growth-Factor Receptor-Positive Tumors. Cancer Biother. Radiopharm. 2008; 23:158–171. [PubMed: 18454685]

(38). Devaraj NK, Keliher EJ, Thurber GM, Nahrendorf M, Weissleder R. 18F Labeled Nanoparticles for in Vivo PET-CT Imaging. Bioconjugate Chem. 2009; 20:397–401.

(39). Herth MM, Barz M, Moderegger D, Allmeroth M, Jahn M, Thews O, Zentel R, Rosch F. Radioactive Labeling of Defined HPMA-Based Polymeric Structures Using [18F]FETos for in Vivo Imaging by Positron Emission Tomography. Biomacromolecules. 2009; 10:1697–1703. [PubMed: 19425549]

(40). Nahrendorf M, Keliher E, Panizzi P, Zhang H, Hembrador S, Figueiredo JL, Aikawa E, Kelly K, Libby P, Weissleder R. 18F-4V for PET-CT Imaging of VCAM-1 Expression in Atherosclerosis. JACC. Cardiovasc. Imaging. 2009; 2:1213–1222. [PubMed: 19833312]

(41). Keliher EJ, Reiner T, Turetsky A, Hilderbrand SA, Weissleder R. High-Yielding, Two-Step 18F Labeling Strategy for 18F-PARP1 Inhibitors. ChemMedChem. 2011; 6:424–427. [PubMed: 21360818]

(42). Hendricks JA, Keliher EJ, Marinelli B, Reiner T, Weissleder R, Mazitschek R. In Vivo PET Imaging of Histone Deacetylases by 18F-Suberoylanilide Hydroxamic Acid (18F-SAHA). J. Med. Chem. 2011; 54:5576–5582. [PubMed: 21721525]

(43). Reiner T, Keliher EJ, Earley S, Marinelli B, Weissleder R. Synthesis and in Vivo Imaging of a 18F-Labeled PARP1 Inhibitor Using a Chemically Orthogonal Scavenger-Assisted High-Performance Method. Angew. Chem. Int. Ed. 2011; 50:1922–1925.

(44). Hendricks JA, Keliher EJ, Wan D, Hilderbrand SA, Weissleder R, Mazitschek R. Synthesis of [18F]BODIPY: Bifunctional Reporter for Hybrid Optical/Positron Emission Tomography Imaging. Angew. Chem. Int. Ed. 2012; 51:4603–4606.

(45). Schieferstein H, Kelsch A, Reibel A, Koynov K, Barz M, Buchholz HG, Bausbacher N, Thews O, Zentel R, Ross TL. 18F-Radiolabeling, Preliminary Evaluation of Folate-pHPMA Conjugates via PET. Macromol. Biosci. 2014; 14:1396–1405. [PubMed: 25088821]

(46). Hara T, Truelove J, Tawakol A, Wojtkiewicz GR, Hucker WJ, MacNabb MH, Brownell AL, Jokivarsi K, Kessinger CW, Jaff MR, Henke PK, Weissleder R, Jaffer FA. 18F-Fluorodeoxyglucose Positron Emission Tomography/Computed Tomography Enables the Detection of Recurrent Same-Site Deep Vein Thrombosis by Illuminating Recently Formed, Neutrophil-Rich Thrombus. Circulation. 2014; 130:1044–1052. [PubMed: 25070665]

(47). Oh P, Borgstrom P, Witkiewicz H, Li Y, Borgstrom BJ, Chrastina A, Iwata K, Zinn KR, Baldwin R, Testa JE, Schnitzer JE. Live Dynamic Imaging of Caveolae Pumping Targeted Antibody Rapidly and Specifically Across Endothelium in the Lung. Nat. Biotechnol. 2007; 25:327–337. [PubMed: 17334358]

(48). Judenhofer MS, Wehrl HF, Newport DF, Catana C, Siegel SB, Becker M, Thielscher A, Kneilling M, Lichy MP, Eichner M, Klingel K, Reischl G, Widmaier S, Rocken M, Nutt RE, Machulla HJ, Uludag K, Cherry SR, Claussen CD, Pichler BJ. Simultaneous PET-MRI: a New Approach for Functional and Morphological Imaging. Nat. Med. 2008; 14:459–465. [PubMed: 18376410]

(49). Nahrendorf M, Keliher E, Marinelli B, Waterman P, Feruglio PF, Fexon L, Pivovarov M, Swirski FK, Pittet MJ, Vinegoni C, Weissleder R. Hybrid PET-Optical Imaging Using Targeted Probes. Proc. Natl. Acad. Sci. U.S.A. 2010; 107:7910–7915. [PubMed: 20385821]

(50). Warde N. Imaging: PET-CT Promising in Animal Studies. Nat.Rev.Rheumatol. 2011; 7:3. [PubMed: 21260966]

(51). Marik J, Tartis MS, Zhang H, Fung JY, Kheirolomoom A, Sutcliffe JL, Ferrara KW. Long-Circulating Liposomes Radiolabeled With [18F] Fluorodipalmitin ([18F] FDP). Nucl. Med. Biol. 2007; 34:165–171. [PubMed: 17307124]

(52). Andreozzi E, Seo JW, Ferrara K, Louie A. Novel Method to Label Solid Lipid Nanoparticles With 64Cu for Positron Emission Tomography Imaging. Bioconjugate Chem. 2011

Europe PMC Funders Author Manuscripts

(53). Lee HY, Li Z, Chen K, Hsu AR, Xu C, Xie J, Sun S, Chen X. PET/MRI Dual-Modality Tumor Imaging Using Arginine-Glycine-Aspartic (RGD)-Conjugated Radiolabeled Iron Oxide Nanoparticles. J. Nucl. Med. 2008; 49:1371–1379. [PubMed: 18632815]

(54). Winter PM, Morawski AM, Caruthers SD, Fuhrhop RW, Zhang H, Williams TA, Allen JS, Lacy EK, Robertson JD, Lanza GM, Wickline SA. Molecular Imaging of Angiogenesis in Early-Stage Atherosclerosis With Alphav-Beta3-Integrin-Targeted Nanoparticles. Circulation. 2003; 108:2270–2274. [PubMed: 14557370]

(55). Flacke S, Fischer S, Scott MJ, Fuhrhop RJ, Allen JS, McLean M, Winter P, Sicard GA, Gaffney PJ, Wickline SA, Lanza GM. Novel MRI Contrast Agent for Molecular Imaging of Fibrin Implications for Detecting Vulnerable Plaques. Circulation. 2001; 104:1280–1285. [PubMed: 11551880]

(56). Mulder WJ, Fayad ZA. Nanomedicine Captures Cardiovascular Disease. Arterioscler., Thromb. Vasc. Biol. 2008; 28:801–802. [PubMed: 18421003]

(57). Nahrendorf M, Waterman P, Thurber G, Groves K, Rajopadhye M, Panizzi P, Marinelli B, Aikawa E, Pittet MJ, Swirski FK, Weissleder R. Hybrid in Vivo FMT-CT Imaging of Protease Activity in Atherosclerosis With Customized Nanosensors. Arterioscler. Thromb. Vasc. Biol. 2009; 29:1444–1451. [PubMed: 19608968]

(58). Skajaa T, Cormode DP, Falk E, Mulder WJM, Fisher EA, Fayad ZA. High-Density Lipoprotein-Based Contrast Agents for Multimodal Imaging of Atherosclerosis. Arterioscler. Thromb. Vasc. Biol. 2010; 30:169–176. [PubMed: 19815819]

(59). Lanza G, Winter P, Cyrus T, Caruthers S, Marsh J, Hughes M, Wickline S. Nanomedicine Opportunities in Cardiology. Ann. N. Y. Acad. Sci. 2006; 1080:451–465. [PubMed: 17132801]

(60). Lanza GM, Winter PM, Caruthers SD, Hughes MS, Cyrus T, Marsh JN, Neubauer AM, Partlow KC, Wickline SA. Nanomedicine Opportunities for Cardiovascular Disease With Perfluorocarbon Nanoparticles. Nanomedicine (London, U.K.). 2006; 1:321–329. [PubMed: 17716162]

(61). Mulder WJM, Strijkers GJ, van Tilborg GAF, Cormode DP, Fayad ZA, Nicolay K. Nanoparticulate Assemblies of Amphiphiles and Diagnostically Active Materials for Multimodality Imaging. Acc. Chem. Res. 2009; 42:904–914. [PubMed: 19435319]

(62). Huang X, Zhang F, Lee S, Swierczewska M, Kiesewetter DO, Lang L, Zhang G, Zhu L, Gao H, Choi HS, Niu G, Chen X. Long-Term Multimodal Imaging of Tumor Draining Sentinel Lymph Nodes Using Mesoporous Silica-Based Nanoprobes. Biomaterials. 2012; 33:4370–4378. [PubMed: 22425023]

(63). Stockhofe K, Postema JM, Schieferstein H, Ross TL. Radiolabeling of Nanoparticles and Polymers for PET Imaging. Pharmaceuticals. 2014; 7:392–418. [PubMed: 24699244]

(64). Karmani L, Labar D, Valembois V, Bouchat V, Nagaswaran PG, Bol A, Gillart J, Leveque P, Bouzin C, Bonifazi D, Michiels C, Feron O, Gregoire V, Lucas S, Vander BT, Gallez B. Antibody-Functionalized Nanoparticles for Imaging Cancer: Influence of Conjugation to Gold Nanoparticles on the Biodistribution of 89Zr-Labeled Cetuximab in Mice. Contrast. Media Mol. Imaging. 2013; 8:402–408. [PubMed: 23740810]

(65). Vosjan MJ, Vercammen J, Kolkman JA, Stigter-van WM, Revets H, van Dongen GA. Nanobodies Targeting the Hepatocyte Growth Factor: Potential New Drugs for Molecular Cancer Therapy. Mol. Cancer Ther. 2012; 11:1017–1025. [PubMed: 22319202]

(66). Keliher EJ, Yoo J, Nahrendorf M, Lewis JS, Marinelli B, Newton A, Pittet MJ, Weissleder R. 89Zr-Labeled Dextran Nanoparticles Allow in Vivo Macrophage Imaging. Bioconjugate Chem. 2011; 22:2383–2389.

(67). van Dongen GA, Huisman MC, Boellaard R, Hendrikse N, Windhorst A, Visser G, Molthoff CF, Vugts DJ. 89Zr-Immuno-PET for Imaging of Long Ciculating Drugs and Disease Targets: Why, How and When to Be Applied? Q. J Nucl. Med. Mol. Imaging. 2014

(68). Cohen R, Vugts DJ, Stigter-van WM, Visser GW, van Dongen GA. Inert Coupling of IRDye800CW and Zirconium-89 to Monoclonal Antibodies for Single- or Dual-Mode Fluorescence and PET Imaging. Nat. Protoc. 2013; 8:1010–1018. [PubMed: 23619892]

Europe PMC Funders Author Manuscripts

(69). Vugts DJ, Visser GW, van Dongen GA. 89Zr-PET Radiochemistry in the Development and Application of Therapeutic Monoclonal Antibodies and Other Biologicals. Curr. Top. Med. Chem. 2013; 13:446–457. [PubMed: 23432007]

(70). Heuveling DA, van SA, Vugts DJ, Hendrikse NH, Yaqub M, Hoekstra OS, Karagozoglu KH, Leemans CR, van Dongen GA, de BR. Pilot Study on the Feasibility of PET/CT Lymphoscintigraphy With 89Zr-Nanocolloidal Albumin for Sentinel Node Identification in Oral Cancer Patients. J. Nucl. Med. 2013; 54:585–589. [PubMed: 23378643]

(71). Heuveling DA, Visser GW, Baclayon M, Roos WH, Wuite GJ, Hoekstra OS, Leemans CR, de BR, van Dongen GA. 89Zr-Nanocolloidal Albumin-Based PET/CT Lymphoscintigraphy for Sentinel Node Detection in Head and Neck Cancer: Preclinical Results. J. Nucl. Med. 2011; 52:1580–1584. [PubMed: 21890880]

(72). Vugts DJ, van Dongen GA. (89)Zr-Labeled Compounds for PET Imaging Guided Personalized Therapy. Drug Discovery Today: Technol. 2011; 8:e53–e61.

(73). Tijink BM, Laeremans T, Budde M, Stigter-van WM, Dreier T, de Haard HJ, Leemans CR, van Dongen GA. Improved Tumor Targeting of Anti-Epidermal Growth Factor Receptor Nanobodies Through Albumin Binding: Taking Advantage of Modular Nanobody Technology. Mol. Cancer Ther. 2008; 7:2288–2297. [PubMed: 18723476]

(74). Perk LR, Visser GW, Vosjan MJ, Stigter-van WM, Tijink BM, Leemans CR, van Dongen GA. (89)Zr As a PET Surrogate Radioisotope for Scouting Biodistribution of the Therapeutic Radiometals (90)Y and (177)Lu in Tumor-Bearing Nude Mice After Coupling to the Internalizing Antibody Cetuximab. J. Nucl. Med. 2005; 46:1898–1906. [PubMed: 16269605]

(75). Verel I, Visser GW, Boellaard R, Boerman OC, van EJ, Snow GB, Lammertsma AA, van Dongen GA. Quantitative 89Zr Immuno-PET for in Vivo Scouting of 90Y-Labeled Monoclonal Antibodies in Xenograft-Bearing Nude Mice. J. Nucl. Med. 2003; 44:1663–1670. [PubMed: 14530484]

(76). Perez-Medina C, Abdel-Atti D, Zhang Y, Longo VA, Irwin CP, Binderup T, Ruiz-Cabello J, Fayad ZA, Lewis JS, Mulder WJM, Reiner T. A Modular Labeling Strategy for In Vivo PET and Near-Infrared Fluorescence Imaging of Nanoparticle Tumor Targeting. J. Nucl. Med. 2014; 55:1706–1711. [PubMed: 25060196]

(77). Majmudar MD, Yoo J, Keliher EJ, Truelove JJ, Iwamoto Y, Sena B, Dutta P, Borodovsky A, Fitzgerald K, Carli MFD, Libby P, Anderson DG, Swirski FK, Weissleder R, Nahrendorf M. Polymeric Nanoparticle PET/MR Imaging Allows Macrophage Detection in Atherosclerotic Plaques. Circ. Res. 2013; 122:755–761. [PubMed: 23300273]

(78). Head HW, Dodd GD, Bao A, Soundararajan A, Garcia-Rojas X, Prihoda TJ, McManus LM, Goins BA, Santoyo CA, Phillips WT. Combination Radiofrequency Ablation and Intravenous Radiolabeled Liposomal Doxorubicin: Imaging and Quantification of Increased Drug Delivery to Tumors. Radiology. 2010; 255:405. [PubMed: 20413753]

(79). Chrastina A, Massey KA, Schnitzer JE. Overcoming in Vivo Barriers to Targeted Nanodelivery. Wiley Interdiscip.Rev.: Nanomed.Nanobiotechnol. 2011; 3:421–437. [PubMed: 21538941]

(80). Zhang R, Xiong C, Huang M, Zhou M, Huang Q, Wen X, Liang D, Li C. Peptide-Conjugated Polymeric Micellar Nanoparticles for Dual SPECT and Optical Imaging of EphB4 Receptors in Prostate Cancer Xenografts. Biomaterials. 2011; 32:5872–5879. [PubMed: 21612822]

(81). de Vries A, Custers E, Lub J, van den Bosch S, Nicolay K, Grull H. Block-Copolymer-Stabilized Iodinated Emulsions for Use As CT Contrast Agents. Biomaterials. 2010; 31:6537–6544. [PubMed: 20541800]

(82). Zheng J, Jaffray D, Allen C. Quantitative CT Imaging of the Spatial and Temporal Distribution of Liposomes in a Rabbit Tumor Model. Mol. Pharmaceutics. 2009; 6:571–580.

(83). Dunne M, Zheng J, Rosenblat J, Jaffray DA, Allen C. APN/CD13-Targeting As a Strategy to Alter the Tumor Accumulation of Liposomes. J. Controlled Release. 2011; 154:298–305.

(84). Mulder WJ, McMahon MT, Nicolay K. The Evolution of MRI Probes: From the Initial Development to State-of-the-Art Applications. NMR Biomed. 2013; 26:725–727. [PubMed: 23784954]

(85). Langereis S, Geelen T, Grull H, Strijkers GJ, Nicolay K. Paramagnetic Liposomes for Molecular MRI and MRI-Guided Drug Delivery. NMR Biomed. 2013; 26:728–744. [PubMed: 23703874]

Europe PMC Funders Author Manuscripts

(86). Kluza E, Strijkers GJ, Nicolay K. Multifunctional Magnetic Resonance Imaging Probes. Recent Results Cancer Res. 2013; 187:151–190. [PubMed: 23179881]

(87). Caravan P, Ellison JJ, McMurry TJ, Lauffer RB. Gadolinium(III) Chelates As MRI Contrast Agents: Structure, Dynamics, and Applications. Chem. Rev. 1999; 8:2293–2352. [PubMed: 11749483]

(88). Mulder WJM, Strijkers GJ, van Tilborg GAF, Griffioen AW, Nicolay K. Lipid-Based Nanoparticles for Contrast-Enhanced MRI and Molecular Imaging. NMR Biomed. 2006; 19:142–164. [PubMed: 16450332]

(89). Mulder WJ, Strijkers GJ, van Tilborg GA, Cormode DP, Fayad ZA, Nicolay K. Nanoparticulate Assemblies of Amphiphiles and Diagnostically Active Materials for Multimodality Imaging. Acc. Chem. Res. 2009; 42:904–914. [PubMed: 19435319]

(90). Mulder WJ, Strijkers GJ, Vucic E, Cormode DP, Nicolay K, Fayad ZA. Magnetic Resonance Molecular Imaging Contrast Agents and Their Application in Atherosclerosis. Top. Magn. Reson. Imaging. 2007; 18:409–417. [PubMed: 18025995]

(91). Mulder WJ, Griffioen AW, Strijkers GJ, Cormode DP, Nicolay K, Fayad ZA. Magnetic and Fluorescent Nanoparticles for Multimodality Imaging. Nanomedicine (London, U. K.). 2007; 2:307–324. [PubMed: 17716176]

(92). Strijkers GJ, Mulder WJ, van Tilborg GA, Nicolay K. MRI Contrast Agents: Current Status and Future Perspectives. Anticancer Agents Med. Chem. 2007; 7:291–305. [PubMed: 17504156]

(93). Terreno E, Castelli DD, Viale A, Aime S. Challenges for Molecular Magnetic Resonance Imaging. Chem. Rev. 2012; 110:3019–3042. [PubMed: 20415475]

(94). Huang R, Han L, Li J, Liu S, Shao K, Kuang Y, Hu X, Wang X, Lei H, Jiang C. Chlorotoxin-Modified Macromolecular Contrast Agent for MRI Tumor Diagnosis. Biomaterials. 2011; 32:5177–5186. [PubMed: 21531455]

(95). Sun C, Veiseh O, Gunn J, Fang C, Hansen S, Lee D, Sze R, Ellenbogen RG, Olson J, Zhang M. In Vivo MRI Detection of Gliomas by Chlorotoxin-Conjugated Superparamagnetic Nanoprobes. Small. 2008; 4:372–379. [PubMed: 18232053]

(96). Sun C, Fang C, Stephen Z, Veiseh O, Hansen S, Lee D, Ellenbogen RG, Olson J, Zhang M. Tumor-Targeted Drug Delivery and MRI Contrast Enhancement by Chlorotoxin-Conjugated Iron Oxide Nanoparticles. Nanomedicine (London, U.K.). 2008; 3:495–505. [PubMed: 18694312]

(97). de Smet M, Heijman E, Langereis S, Hijnen NM, Gruell H. Magnetic Resonance Imaging of High Intensity Focused Ultrasound Mediated Drug Delivery From Temperature-Sensitive Liposomes: An in Vivo Proof-of-Concept Study. J. Controlled Release. 2011; 150:102–110.

(98). Onuki Y, Jacobs I, Artemov D, Kato Y. Noninvasive Visualization of in Vivo Release and Intratumoral Distribution of Surrogate MR Contrast Agent Using the Dual MR Contrast Technique. Biomaterials. 2010; 31:7132–7138. [PubMed: 20580427]

(99). li Castelli D, Dastru W, Terreno E, Cittadino E, Mainini F, Torres E, Spadaro M, Aime S. In Vivo MRI Multicontrast Kinetic Analysis of the Uptake and Intracellular Trafficking of Paramagnetically Labeled Liposomes. J. Controlled Release. 2010; 144:271–279.

(100). de Vries IJ, Lesterhuis WJ, Barentsz JO, Verdijk P, van Krieken JH, Boerman OC, Oyen WJ, Bonenkamp JJ, Boezeman JB, Adema GJ, Bulte JW, Scheenen TW, Punt CJ, Heerschap A, Figdor CG. Magnetic Resonance Tracking of Dendritic Cells in Melanoma Patients for Monitoring of Cellular Therapy. Nat. Biotechnol. 2005; 23:1407–1413. [PubMed: 16258544]

(101). Ahrens ET, Helfer BM, O'Hanlon CF, Schirda C. Clinical Cell Therapy Imaging Using a Perfluorocarbon Tracer and Fluorine-19 MRI. Magn. Reson. Med. 2014; 72:1696–1701. [PubMed: 25241945]

(102). Long CM, van Laarhoven HWM, Bulte JWM, Levitsky HI. Magnetovaccination As a Novel Method to Assess and Quantify Dendritic Cell Tumor Antigen Capture and Delivery to Lymph Nodes. Cancer Res. 2009; 69:3180–3187. [PubMed: 19276358]

(103). Fortin-Ripoche JP, Martina MS, Gazeau F, Menager C, Wilhelm C, Bacri JC, Lesieur S, Clement O. Magnetic Targeting of Magnetoliposomes to Solid Tumors With MR Imaging Monitoring in Mice: Feasibility. Radiology. 2006; 239:415–424. [PubMed: 16549622]

Europe PMC Funders Author Manuscripts

(104). Wunder A, Muller-Ladner U, Stelzer EHK, Funk JA, Neumann E, Stehle G, Pap T, Sinn H, Gay S, Fiehn C. Albumin-Based Drug Delivery As Novel Therapeutic Approach for Rheumatoid Arthritis. J. Immunol. 2003; 170:4793–4801. [PubMed: 12707361]

(105). Licha K, Olbrich C. Optical Imaging in Drug Discovery and Diagnostic Applications. Adv. Drug Deliv. Rev. 2005; 57:1087–1108. [PubMed: 15908041]

(106). Mountz JM, Alavi A, Mountz JD. Emerging Optical and Nuclear Medicine Imaging Methods in Rheumatoid Arthritis. Nat. Rev. Rheumatol. 2012; 8:719–728. [PubMed: 23007740]

(107). Ntziachristos V, Weissleder R. Experimental Three-Dimensional Fluorescence Reconstruction of Diffuse Media by Use of a Normalized Born Approximation. Opt. Lett. 2001; 26:893–895. [PubMed: 18040483]

(108). Kunjachan S, Pola R, Gremse F, Theek B, Ehling J, Moeckel D, Hermanns-Sachweh B, Pechar M, Ulbrich K, Hennink WE, Storm G, Lederle W, Kiessling F, Lammers T. Passive Versus Active Tumor Targeting Using RGD- and NGR-Modified Polymeric Nanomedicines. Nano Lett. 2014; 14:972–981. [PubMed: 24422585]

(109). Ntziachristos V, Bremer C, Weissleder R. Fluorescence Imaging With Near-Infrared Light: New Technological Advances That Enable in Vivo Molecular Imaging. Eur. J. Radiol. 2003; 13:195–208.

(110). Hyde D, de Kleine R, MacLaurin SA, Miller E, Brooks DH, Krucker T, Ntziachristos V. Hybrid FMT-CT Imaging of Amyloid- Plaques in a Murine Alzheimer's Disease Model. NeuroImage. 2009; 44:1304–1311. [PubMed: 19041402]

(111). Ntziachristos V, Tung CH, Bremer C, Weissleder R. Fluorescence Molecular Tomography Resolves Protease Activity in Vivo. Nat. Med. 2002; 8:757–760. [PubMed: 12091907]

(112). Ale A, Ermolayev V, Herzog E, Cohrs C, de Angelis MH, Ntziachristos V. FMT-XCT: in Vivo Animal Studies With Hybrid Fluorescence Molecular Tomography-X-Ray Computed Tomography. Nat. Methods. 2012; 9:615–620. [PubMed: 22561987]

(113). Kumar S, Richards-Kortum R. Optical Molecular Imaging Agents for Cancer Diagnostics and Therapeutics. Nanomedicine. 2011; 1:23–30. [PubMed: 17716206]

(114). Dam GM, Themelis G, Crane LMA, Harlaar NJ, Pleijhuis RG, Kelder W, Sarantopoulos A, Jong J. S. d. Arts HJG, Zee AGJ, Bart J, Low PS, Ntziachristos V. Intraoperative Tumor-Specific Fluorescence Imaging in Ovarian Cancer by Folate Receptor Targeting: First in-Human Results. Nat. Med. 2011; 17:1315–1319. [PubMed: 21926976]

(115). Keereweer S, Kerrebijn J, van Driel P, Xie B, Kaijzel E, Snoeks T, Que I, Hutteman M, van der Vorst J, Mieog J, Vahrmeijer A, van de Velde C, Baatenburg de Jong R, Lowik C. Optical Image-Guided Surgery- "Where Do We Stand"? Mol. Imaging Biol. 2011; 13:199–207. [PubMed: 20617389]

(116). Kosaka N, Mitsunaga M, Longmire MR, Choyke PL, Kobayashi H. Near Infrared Fluorescence-Guided Real-Time Endoscopic Detection of Peritoneal Ovarian Cancer Nodules Using Intravenously Injected Indocyanine Green. Int. J. Cancer. 2011; 129:1671–1677. [PubMed: 21469142]

(117). Chen W, Jarzyna PA, van Tilborg GAF, Nguyen VA, Cormode DP, Klink A, Griffioen AW, Randolph GJ, Fisher EA, Mulder WJM, Fayad ZA. RGD Peptide Functionalized and Reconstituted High-Density Lipoprotein Nanoparticles As a Versatile and Multimodal Tumor Targeting Molecular Imaging Probe. FASEB J. 2010; 24:1689–1699. [PubMed: 20075195]

(118). Kim JY, Choi WI, Kim YH, Tae G. Highly Selective in-Vivo Imaging of Tumor As an Inflammation Site by ROS Detection Using Hydrocyanine-Conjugated, Functional Nano-Carriers. J. Controlled Release. 2011; 156:398–405.

(119). Frangioni JV. In Vivo Near-Infrared Fluorescence Imaging. Curr. Opin. Chem. Biol. 2003; 7:626–634. [PubMed: 14580568]

(120). Kunjachan S, Gremse F, Theek B, Koczera P, Pola R, Pechar M, Etrych T, Ulbrich K, Storm G, Kiessling F, Lammers T. Noninvasive Optical Imaging of Nanomedicine Biodistribution. ACS Nano. 2013; 7:252–262. [PubMed: 23067565]

(121). H. i. '. Veld R, Storm G, Hennink WE, Kiessling F, Lammers T. Macromolecular Nanotheranostics for Multimodal Anticancer Therapy. Nanoscale. 2011; 3:4022–4034. [PubMed: 21901211]

Europe PMC Funders Author Manuscripts

(122). Lammers T, Kuhnlein R, Kissel M, Subr V, Etrych T, Pola R, Pechar M, Ulbrich K, Storm G, Huber P, Peschke P. Effect of Physicochemical Modification on the Biodistribution and Tumor Accumulation of HPMA Copolymers. J. Controlled Release. 2005; 110:103–118.

(123). Etrych T, Subr V, Strohalm J, Sirova M, Rihova B, Ulbrich K. HPMA Copolymer-Doxorubicin Conjugates: The Effects of Molecular Weight and Architecture on Biodistribution and in Vivo Activity. J. Controlled Release. 2012

(124). Graves EE, Ripoll J, Weissleder R, Ntziachristos V. A Submillimeter Resolution Fluorescence Molecular Imaging System for Small Animal Imaging. Med. Phys. 2003; 30:901–911. [PubMed: 12772999]

(125). Ntziachristos V. Fluorescence Molecular Imaging. Annu. Rev. Biomed. Eng. 2006; 8:1–33. [PubMed: 16834550]

(126). Schulz RB, Ale A, Sarantopoulos A, Freyer M, Soehngen E, Zientkowska M, Ntziachristos V. Hybrid System for Simultaneous Fluorescence and X-Ray Computed Tomography. IEEE Trans. Med. Imaging. 2010; 29:465–473. [PubMed: 19906585]

(127). Panizzi P, Nahrendorf M, Figueiredo JL, Panizzi J, Marinelli B, Iwamoto Y, Keliher E, Maddur AA, Waterman P, Kroh HK, Leuschner F, Aikawa E, Swirski FK, Pittet MJ, Hackeng TM, Fuentes-Prior P, Schneewind O, Bock PE, Weissleder R. In Vivo Detection of Staphylococcus Aureus Endocarditis by Targeting Pathogen-Specific Prothrombin Activation. Nat. Med. 2011; 17:1142–1146. [PubMed: 21857652]

(128). Lammers T, Peschke P, Kuhnlein R, Subr V, Ulbrich K, Debus J, Huber P, Hennink W, Storm G. Effect of Radiotherapy and Hyperthermia on the Tumor Accumulation of HPMA Copolymer-Based Drug Delivery Systems. J. Controlled Release. 2007; 117:333–341.

(129). Xu M, Wang LV. Photoacoustic Imaging in Biomedicine. Rev. Sci. Instrum. 2006; 77

(130). Razansky D, Ntziachristos V. Hybrid Photoacoustic Fluorescence Molecular Tomography Using Finite-Element-Based Inversion. Med. Phys. 2007; 34:4293–4301. [PubMed: 18072494]

(131). Ntziachristos V. Going Deeper Than Microscopy: the Optical Imaging Frontier in Biology. Nat. Methods. 2010; 7:603–614. [PubMed: 20676081]

(132). Mallidi S, Larson T, Tam J, Joshi PP, Karpiouk A, Sokolov K, Emelianov S. Multiwavelength Photoacoustic Imaging and Plasmon Resonance Coupling of Gold Nanoparticles for Selective Detection of Cancer. Nano Lett. 2009; 9:2825–2831. [PubMed: 19572747]

(133). Kim C, Cho EC, Chen J, Song KH, Au L, Favazza C, Zhang Q, Cobley CM, Gao F, Xia Y, Wang LV. In Vivo Molecular Photoacoustic Tomography of Melanomas Targeted by Bioconjugated Gold Nanocages. ACS Nano. 2010; 4:4559–4564. [PubMed: 20731439]

(134). Manohar S, Ungureanu C, van Leeuwen TG. Gold Nanorods As Molecular Contrast Agents in Photoacoustic Imaging: the Promises and the Caveats. Contrast Media Mol. Imaging. 2011; 6:389–400. [PubMed: 22025339]

(135). Mallidi S, Luke GP, Emelianov S. Photoacoustic Imaging in Cancer Detection, Diagnosis, and Treatment Guidance. Trends Biotechnol. 2011; 29:213–221. [PubMed: 21324541]

(136). Stritzker J, Kirscher L, Scadeng M, Deliolanis NC, Morscher S, Symvoulidis P, Schaefer K, Zhang Q, Buckel L, Hess M, Donat U, Bradley WG, Ntziachristos V, Szalay AA. Vaccinia Virus-Mediated Melanin Production Allows MR and Optoacoustic Deep Tissue Imaging and Laser-Induced Thermotherapy of Cancer. Proc. Natl. Acad. Sci. U.S.A. 2012; 110:3316–3320. [PubMed: 23401518]

(137). Song L, Kim C, Maslov K, Shung KK, Wang LV. High-Speed Dynamic 3D Photoacoustic Imaging of Sentinel Lymph Node in a Murine Model Using an Ultrasound Array. Med. Phys. 2009; 36:3724–3729. [PubMed: 19746805]

(138). Song KH, Kim C, Cobley CM, Xia Y, Wang LV. Near-Infrared Gold Nanocages As a New Class of Tracers for Photoacoustic Sentinel Lymph Node Mapping on a Rat Model. Nano Lett. 2009; 9:183–188. [PubMed: 19072058]

(139). Erpelding TN, Kim C, Pramanik M, Jankovic L, Maslov K, Guo Z, Margenthaler JA, Pashley MD, Wang LV. Sentinel Lymph Nodes in the Rat: Noninvasive Photoacoustic and US Imaging With a Clinical US System. Radiology. 2010; 256:102–110. [PubMed: 20574088]

Europe PMC Funders Author Manuscripts

Europe PMC Funders Author Manuscripts

(140). Kim K, Huang SW, Ashkenazi S, O Donnell M, Agarwal A, Kotov NA, Denny MF, Kaplan MJ. Photoacoustic Imaging of Early Inflammatory Response Using Gold Nanorods. Appl. Phys. Lett. 2007; 90:223901.

(141). Wang B, Yantsen E, Larson T, Karpiouk AB, Sethuraman S, Su JL, Sokolov K, Emelianov SY. Plasmonic Intravascular Photoacoustic Imaging for Detection of Macrophages in Atherosclerotic Plaques. Nano Lett. 2008; 9:2212–2217. [PubMed: 18844426]

(142). Vonnemann J, Beziere N, Bottcher C, Riese SB, Kuehne C, Dernedde J, Licha K, von SC, Kosanke Y, Kimm M, Meier R, Ntziachristos V, Haag R. Polyglycerolsulfate Functionalized Gold Nanorods As Optoacoustic Signal Nanoamplifiers for in Vivo Bioimaging of Rheumatoid Arthritis. Theranostics. 2014; 4:629–641. [PubMed: 24723984]

(143). Hoelen CGA, de Mul FFM, Pongers R, Dekker A. Three-Dimensional Photoacoustic Imaging of Blood Vessels in Tissue. Opt. Lett. 1998; 23:648–650. [PubMed: 18084605]

(144). Wang X, Xie X, Ku G, Wang LV, Stoica G. Noninvasive Imaging of Hemoglobin Concentration and Oxygenation in the Rat Brain Using High-Resolution Photoacoustic Tomography. J. Biomed. Opt. 2006; 11:024015. [PubMed: 16674205]

(145). Hu S, Wang LV. Photoacoustic Imaging and Characterization of the Microvasculature. J. Biomed. Opt. 2010; 15:1–15.

(146). Ntziachristos V, Razansky D. Molecular Imaging by Means of Multispectral Optoacoustic Tomography (MSOT). Chem. Rev. 2010; 110:2783–2794. [PubMed: 20387910]

(147). Ho CJH, Balasundaram G, Driessen W, McLaren R, Wong CL, Dinish US, Attia ABE, Ntziachristos V, Olivo M. Multifunctional Photosensitizer-Based Contrast Agents for Photoacoustic Imaging. Sci. Rep. 2014; 4:1–6.

(148). Beziere N, Lozano N, Nunes A, Salichs J, Queiros D, Kostarelos K, Ntziachristos V. Dynamic Imaging of PEGylated Indocyanine Green (ICG) Liposomes Within the Tumor Microenvironment Using Multi-Spectral Optoacoustic Tomography (MSOT). Biomaterials. 2015; 37:415–424. [PubMed: 25453969]

(149). Kim JW, Galanzha EI, Shashkov EV, Moon HM, Zharov VP. Golden Carbon Nanotubes As Multimodal Photoacoustic and Photothermal High-Contrast Molecular Agents. Nat. Nanotechnol. 2009; 4:688–694. [PubMed: 19809462]

(150). Wang Y, Xie X, Wang X, Ku G, Gill KL, O'Neal DP, Stoica G, Wang LV. Photoacoustic Tomography of a Nanoshell Contrast Agent in the in Vivo Rat Brain. Nano Lett. 2004; 4:1689–1692.

(151). Chen J, Saeki F, Wiley BJ, Cang H, Cobb MJ, Li ZY, Au L, Zhang H, Kimmey MB, Li, Xia Y. Gold Nanocages: Bioconjugation and Their Potential Use As Optical Imaging Contrast Agents. Nano Lett. 2005; 5:473–477. [PubMed: 15755097]

(152). Agarwal A, Huang SW, O Donnell M, Day KC, Day M, Kotov N, Ashkenazi S. Targeted Gold Nanorod Contrast Agent for Prostate Cancer Detection by Photoacoustic Imaging. J. Appl. Phys. 2007; 102:064701.

(153). Yang X, Skrabalak SE, Li ZY, Xia Y, Wang LV. Photoacoustic Tomography of a Rat Cerebral Cortex in Vivo With Au Nanocages As an Optical Contrast Agent. Nano Lett. 2007; 7:3798–3802. [PubMed: 18020475]

(154). Skrabalak SE, Chen J, Sun Y, Lu X, Au L, Cobley CM, Xia Y. Gold Nanocages: Synthesis, Properties, and Applications. Acc. Chem. Res. 2008; 41:1587–1595. [PubMed: 18570442]

(155). Chen YS, Frey W, Kim S, Kruizinga P, Homan K, Emelianov S. Silica-Coated Gold Nanorods As Photoacoustic Signal Nanoamplifiers. Nano Lett. 2011; 11:348–354. [PubMed: 21244082]

(156). De La Zerda A, Zavaleta C, Keren S, Vaithilingam S, Bodapati S, Liu Z, Levi J, Smith BR, Ma TJ, Oralkan O, Cheng Z, Chen X, Dai H, Khuri-Yakub BT, Gambhir SS. Carbon Nanotubes As Photoacoustic Molecular Imaging Agents in Living Mice. Nat. Nanotechnol. 2008; 3:557–562. [PubMed: 18772918]

(157). Liu Z, Tabakman S, Welsher K, Dai H. Carbon Nanotubes in Biology and Medicine: In Vitro and in Vivo Detection, Imaging and Drug Delivery. Nano Res. 2010; 2:85–120. [PubMed: 20174481]

Europe PMC Funders Author Manuscripts

(158). de la Zerda A, Bodapati S, Teed R, May SY, Tabakman SM, Liu Z, Khuri-Yakub BT, Chen X, Dai H, Gambhir SS. Family of Enhanced Photoacoustic Imaging Agents for High-Sensitivity and Multiplexing Studies in Living Mice. ACS Nano. 2012; 6:4694–4701. [PubMed: 22607191]

(159). Fan Q, Cheng K, Hu X, Ma X, Zhang R, Yang M, Lu X, Xing L, Huang W, Gambhir SS, Cheng Z. Transferring Biomarker into Molecular Probe: Melanin Nanoparticle As a Naturally Active Platform for Multimodality Imaging. J. Am.Chem. Soc. 2014; 136:15185–15194. [PubMed: 25292385]

(160). Liopo A, Su R, Oraevsky AA. Melanin Nanoparticles As a Novel Contrast Agent for Optoacoustic Tomography. Photoacoustics. 2014

(161). Repenko T, Fokong S, Laporte LD, Go D, Kiessling F, Lammers T, Kuehne AJC. Water-Soluble Dopamine-Based Polymers for Photoacoustic Imaging. Chem. Commun. 2015; 51:6084–6087.

(162). Kircher MF, de la Zerda A, Jokerst JV, Zavaleta CL, Kempen PJ, Mittra E, Pitter K, Huang R, Campos C, Habte F, Sinclair R, Brennan CW, Mellinghoff IK, Holland EC, Gambhir SS. A Brain Tumor Molecular Imaging Strategy Using a New Triple-Modality MRI-Photoacoustic-Raman Nanoparticle. Nat. Med. 2012; 18:829–834. [PubMed: 22504484]

(163). Medarova Z, Pham W, Farrar C, Petkova V, Moore A. In Vivo Imaging of SiRNA Delivery and Silencing in Tumors. Nat. Med. 2007; 13:372–377. [PubMed: 17322898]

(164). Navarro G, Tros de Ilarduya C. Activated and Non-Activated PAMAM Dendrimers for Gene Delivery in Vitro and in Vivo. Nanomedicine. 2009; 5:287–297. [PubMed: 19523431]

(165). Deckers R, Rome C, Moonen CTW. The Role of Ultrasound and Magnetic Resonance in Local Drug Delivery. J. Magn. Reson. Imaging. 2008; 27:400–409. [PubMed: 18219675]

(166). Bohmer MR, Klibanov AL, Tiemann K, Hall CS, Gruell H, Steinbach OC. Ultrasound Triggered Image-Guided Drug Delivery. Eur. J. Radiol. 2009; 70:242–253. [PubMed: 19272727]

(167). Deckers R, Moonen CTW. Ultrasound Triggered, Image Guided, Local Drug Delivery. J. Controlled Release. 2010; 148:25–33.

(168). Hernot S, Klibanov AL. Microbubbles in Ultrasound-Triggered Drug and Gene Delivery. Adv. Drug Deliv. Rev. 2008; 60:1153–1166. [PubMed: 18486268]

(169). Wang Y, Li X, Zhou Y, Huang P, Xu Y. Preparation of Nanobubbles for Ultrasound Imaging and Intracelluar Drug Delivery. Int. J. Pharm. 2010; 384:148–153. [PubMed: 19781609]

(170). Kiessling F, Fokong S, Koczera P, Lederle W, Lammers T. Ultrasound Microbubbles for Molecular Diagnosis, Therapy, and Theranostics. J. Nucl. Med. 2012; 53:345–348. [PubMed: 22393225]

(171). Wheatley MA, Forsberg F, Dube N, Patel M, Oeffinger BE. Surfactant-Stabilized Contrast Agent on the Nanoscale for Diagnostic Ultrasound Imaging. Ultrasound Med. Biol. 2006; 32:83–93. [PubMed: 16364800]

(172). Rapoport N, Gao Z, Kennedy A. Multifunctional Nanoparticles for Combining Ultrasonic Tumor Imaging and Targeted Chemotherapy. J. Natl. Cancer Inst. 2007; 99:1095–1106. [PubMed: 17623798]

(173). Fokong S, Theek B, Wu Z, Koczera P, Appold L, Jorge S, Resch-Genger U, van Zandvoort M, Storm G, Kiessling F, Lammers T. Image-Guided, Targeted and Triggered Drug Delivery to Tumors Using Polymer-Based Microbubbles. J. Controlled Release. 2012; 163:75–81.

(174). Price RJ, Skyba DM, Kaul S, Skalak TC. Delivery of Colloidal Particles and Red Blood Cells to Tissue Through Microvessel Ruptures Created by Targeted Microbubble Destruction With Ultrasound. Circulation. 1998; 98:1264–1267. [PubMed: 9751673]

(175). Tachibana K, Uchida T, Ogawa K, Yamashita N, Tamura K. Induction of Cell-Membrane Porosity by Ultrasound. Lancet. 1999; 353

(176). Miller DL, Quddus J. Diagnostic Ultrasound Activation of Contrast Agent Gas Bodies Induces Capillary Rupture in Mice. Proc. Natl. Acad. Sci. U.S.A. 2000; 97:10179–10184. [PubMed: 10954753]

(177). Ellegala DB, Leong-Poi H, Carpenter JE, Klibanov AL, Kaul S, Shaffrey ME, Sklenar J, Lindner JR. Imaging Tumor Angiogenesis With Contrast Ultrasound and Microbubbles Targeted to Alpha(v)Beta3. Circulation. 2003; 108:336–341. [PubMed: 12835208]

Europe PMC Funders Author Manuscripts

(178). McDannold N, Vykhodtseva N, Raymond S, Jolesz FA, Hynynen K. MRI-Guided Targeted Blood-Brain Barrier Disruption With Focused Ultrasound: Histological Findings in Rabbits. Ultrasound Med. Biol. 2005; 31:1527–1537. [PubMed: 16286030]

(179). Hauff P, Seemann S, Reszka R, Schultze-Mosgau M, Reinhardt M, Buzasi T, Plath T, Rosewicz S, Schirner M. Evaluation of Gas-Filled Microparticles and Sonoporation As Gene Delivery System: Feasibility Study in Rodent Tumor Models. Radiology. 2005; 236:572–578. [PubMed: 16040915]

(180). Chen S, Ding J. h. Bekeredjian R, Yang B. z. Shohet RV, Johnston SA, Hohmeier HE, Newgard CB, Grayburn PA. Efficient Gene Delivery to Pancreatic Islets With Ultrasonic Microbubble Destruction Technology. Proc. Natl. Acad. Sci. U.S.A. 2006; 103:8469–8474. [PubMed: 16709667]

(181). Tartis MS, McCallan J, Lum AFH, LaBell R, Stieger SM, Matsunaga TO, Ferrara KW. Therapeutic Effects of Paclitaxel-Containing Ultrasound Contrast Agents. Ultrasound Med. Biol. 2006; 32:1771–1780. [PubMed: 17112963]

(182). Ferrara K, Pollard R, Borden M. Ultrasound Microbubble Contrast Agents: Fundamentals and Application to Gene and Drug Delivery. Annu. Rev. Biomed. Eng. 2007; 9:415–447. [PubMed: 17651012]

(183). Merckel LG, Deckers R, Baron P, Bleys RLAW, van Diest PJ, Moonen CTW, Mali WPT, van den Bosch MAAJ, Bartels LW. The Effects of Magnetic Resonance Imaging-Guided High-Intensity Focused Ultrasound Ablation on Human Cadaver Breast Tissue. Eur. J. Pharmacol. 2013

(184). Cheung TT, Fan ST, Chan SC, Chok KS, Chu FS, Jenkins CR, Lo RC, Fung JY, Chan AC, Sharr WW, Tsang SH, Dai WC, Poon RT, Lo CM. High-Intensity Focused Ultrasound Ablation: An Effective Bridging Therapy for Hepatocellular Carcinoma Patients. World J. Gastroenterol. 2013; 19:3083–3089. [PubMed: 23716988]

(185). Viallon M, Petrusca L, Auboiroux V, Goget T, Baboi L, Becker CD, Salomir R. Experimental Methods for Improved Spatial Control of Thermal Lesions in Magnetic Resonance-Guided Focused Ultrasound Ablation. Ultrasound Med. Biol. 2013:1–16. [PubMed: 24210860]

(186). Negussie AH, Yarmolenko PS, Partanen A, Ranjan A, Jacobs G, Woods D, Bryant H, Thomasson D, Dewhirst MW, Wood BJ, Dreher MR. Formulation and Characterisation of Magnetic Resonance Imageable Thermally Sensitive Liposomes for Use With Magnetic Resonance-Guided High Intensity Focused Ultrasound. Int. J. Hyperthermia. 2011; 27:140–155. [PubMed: 21314334]

(187). Ponce AM, Viglianti BL, Yu D, Yarmolenko PS, Michelich CR, Woo J, Bally MB, Dewhirst MW. Magnetic Resonance Imaging of Temperature-Sensitive Liposome Release: Drug Dose Painting and Antitumor Effects. J.Natl.Cancer Inst. 2007; 99:53–63. [PubMed: 17202113]

(188). Mo S, Coussios CC, Seymour L, Carlisle R. Ultrasound-Enhanced Drug Delivery for Cancer. Expert Opin. Drug Delivery. 2012; 9:1525–1538.

(189). Hancock HA, Smith LH, Cuesta J, Durrani AK, Angstadt M, Palmeri ML, Kimmel E, Frenkel V. Investigations into Pulsed High-Intensity Focused Ultrasound-Enhanced Delivery: Preliminary Evidence for a Novel Mechanism. Ultrasound Med.Biol. 2009; 35:1722–1736. [PubMed: 19616368]

(190). Geers B, Lentacker I, Sanders NN, Demeester J, Meairs S, De Smedt SC. Self-Assembled Liposome-Loaded Microbubbles: The Missing Link for Safe and Efficient Ultrasound Triggered Drug-Delivery. J. Controlled Release. 2011; 152:249–256.

(191). Lammers T, Rizzo LY, Storm G, Kiessling F. Personalized Nanomedicine. Clin. Cancer Res. 2012; 18:4889–4894. [PubMed: 22829203]

(192). Harrington KJ, Mohammadtaghi S, Uster PS, Glass D, Peters AM, Vile RG, Stewart JS. Effective Targeting of Solid Tumors in Patients With Locally Advanced Cancers by Radiolabeled Pegylated Liposomes. Clin. Cancer Res. 2001; 7:243–254. [PubMed: 11234875]

(193). Seymour LW, Ferry DR, Anderson D, Hesslewood S, Julyan PJ, Poyner R, Doran J, Young AM, Burtles S, Kerr DJ, Cancer Research, C. P. I Hepatic Drug Targeting: Phase I Evaluation of Polymer-Bound Doxorubicin. J. Clin. Oncol. 2012; 20:1668–1676. [PubMed: 11896118]

(194). Hrkach J, Von Hoff D, Mukkaram Ali M, Andrianova E, Auer J, Campbell T, De Witt D, Figa M, Figueiredo M, Horhota A, Low S, McDonnell K, Peeke E, Retnarajan B, Sabnis A, Schnipper E, Song JJ, Song YH, Summa J, Tompsett D, Troiano G, Van Geen Hoven T, Wright J, LoRusso P, Kantoff PW, Bander NH, Sweeney C, Farokhzad OC, Langer R, Zale S. Preclinical Development and Clinical Translation of a PSMA-Targeted Docetaxel Nanoparticle With a Differentiated Pharmacological Profile. Sci. Transl. Med. 2012; 4:1–11.

(195). Ojha T, Rizzo LY, Storm G, Kiessling F, Lammers T. Image-guided drug delivery: Preclinical applications and clinical translation. Expert Opin. Drug Deliv. in press.

(196). Schroeder A, Heller DA, Winslow MM, Dahlman JE, Pratt GW, Langer R, Jacks T, Anderson DG. Targeting metastatic cancer with nanotechnology. Nat. Rev. Cancer. 2011; 12:39–50. [PubMed: 22193407]

Europe PMC Funders Author Manuscripts

Europe PMC Funders Author Manuscripts

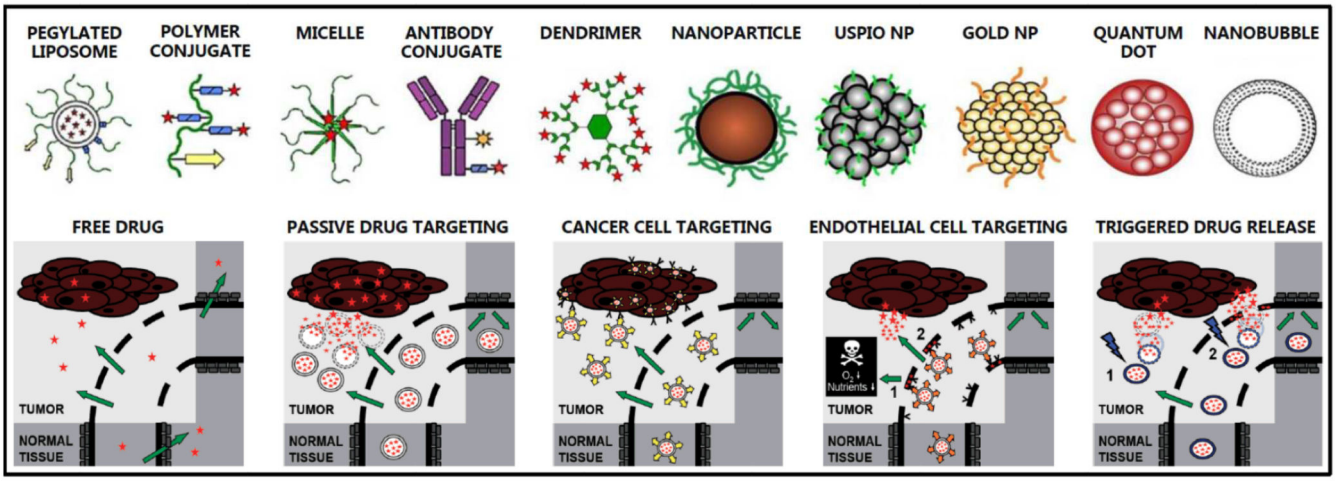

Figure 1.
Examples of routinely used drug delivery systems and drug targeting strategies.

Europe PMC Funders Author Manuscripts

Europe PMC Funders Author Manuscripts

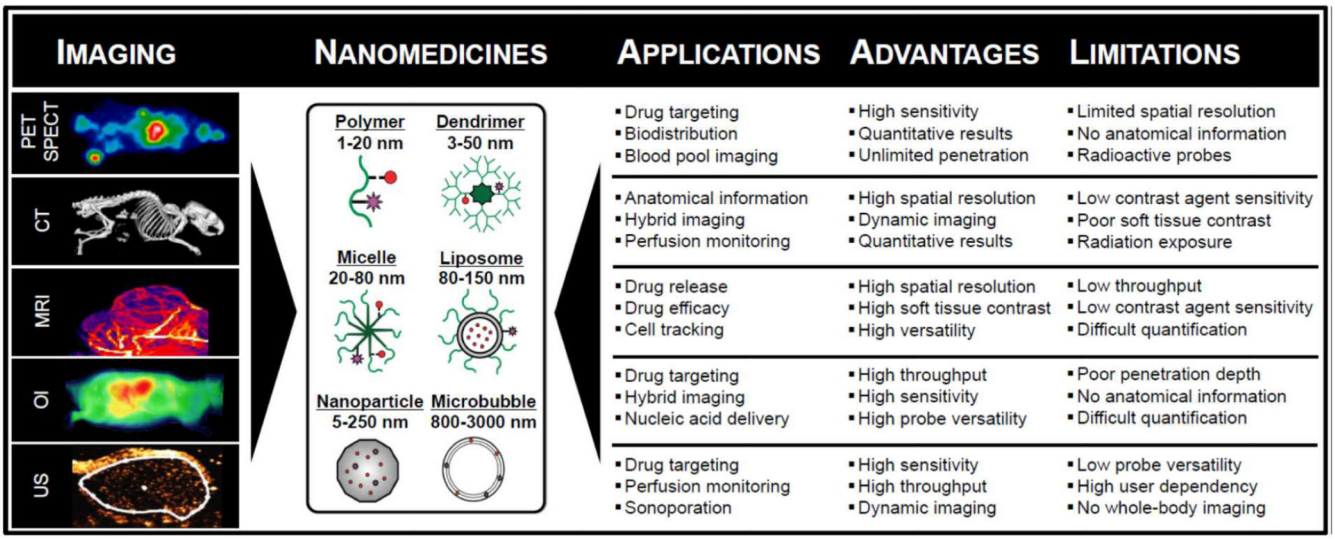

Figure 2.

Schematic depiction of non-invasive imaging techniques routinely used in nanomedicine research, as well as an overview of their specific applications, advantages and limitations.

Europe PMC Funders Author Manuscripts

Europe PMC Funders Author Manuscripts

Europe PMC Funders Author Manuscripts

Europe PMC Funders Author Manuscripts

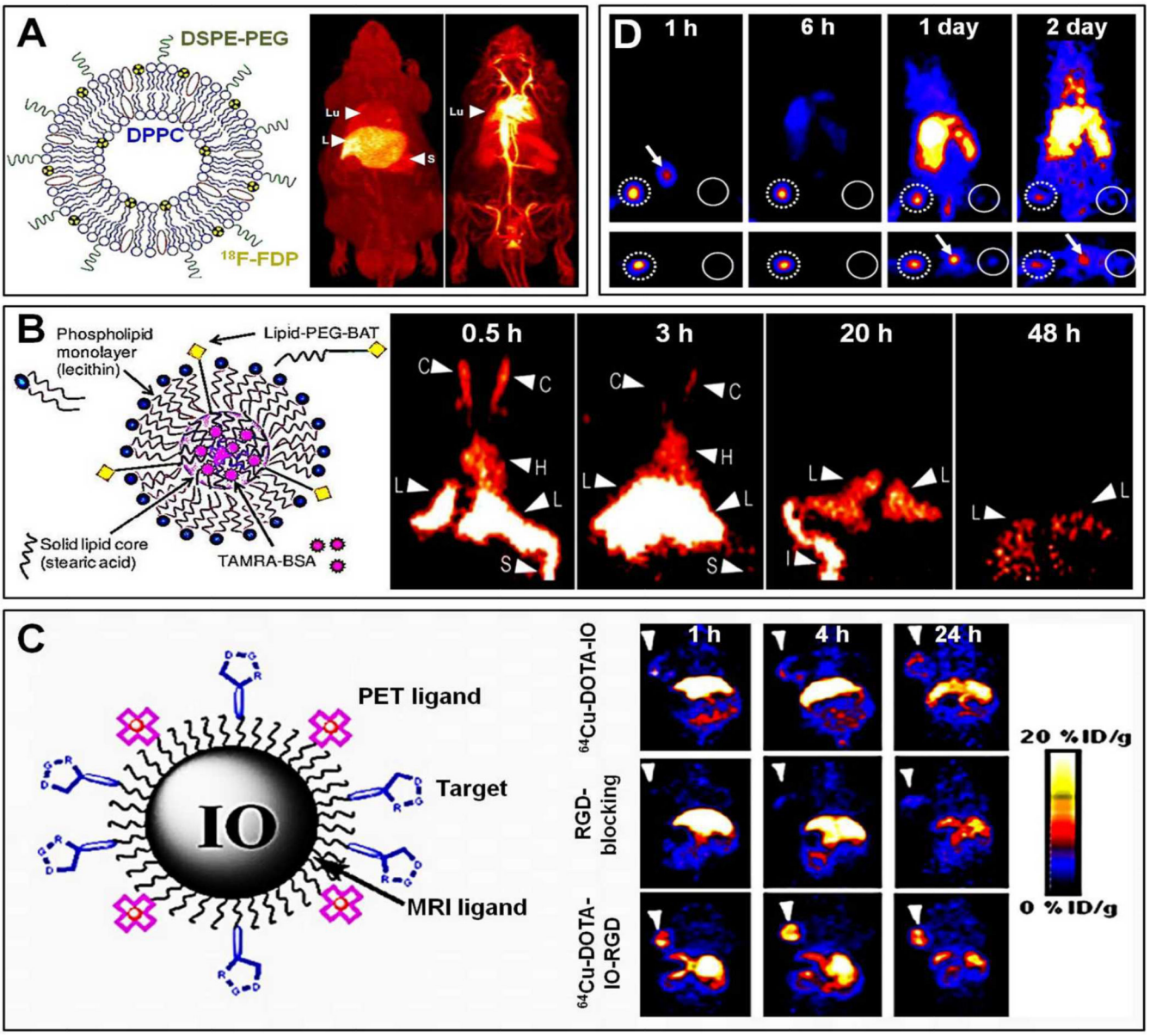

Figure 3. Non-invasive imaging of nanomedicines using PET

A. Left: Schematic structure of a liposomal nanomedicine formulation composed of DSPE-PEG and DPPC, labeled with ^{18}F-FDP. Right: Whole-body maximum intensity projections (MIP) of free ^{18}F-FDP (left) and ^{18}F-FDP-containing (right) liposomes in rats at 90 min after i.v. administration. The left panel exemplifies uptake of free ^{18}F-FDP in liver (L), spleen (S) and lungs (Lu), while the right panel clearly shows that ^{18}F-FDP-containing liposomes are still primarily present in systemic circulation at this time point. **B.** Schematic depiction of BAT-containing (for ^{64}Cu-labeling) solid lipid nanoparticles. Coronal micro-PET images obtained at 0.5, 3, 20 and 48 h after the i.v. injection of ^{64}Cu-labeled solid lipid nanoparticles are shown shown on the right. Initially, strong signals were detected in the heart (H) and carotid arteries (C), whereas at later time points, signals were localized in the liver (L), intestine (I) and spleen (S). **C.** Schematic depiction of iron oxide-based

nanocarriers co-functionalized with PET tracers and integrin-specific RGD peptides. Coronal PET images obtained at 1, 4 and 24 h after the i.v. injection of ^{64}Cu-labeled control iron oxide nanoparticles (^{64}Cu-DOTA-IO; top row), RGD-targeted nanoparticles after pre-blocking with excess free RGD (^{64}Cu-DOTA-IO-RGD; middle row), and RGD-targeted iron oxide nanoparticles (^{64}Cu-DOTA-IO-RGD; bottom row) exemplifying efficient and specific targeting to integrins in U87MG xenografts (arrowheads). **D.** PET imaging of sentinel lymph node identification in a 4T1 metastatic mouse model. Metastatic sentinel lymph nodes (dotted circles; left) and normal contralateral lymph nodes (solid circles; right) were visualized at 1, 6, 24 and 48 h after the injection of multimodal ^{64}Cu-labeled mesoporous silica nanoparticles (MSN-Dye-Gd-^{64}Cu) into the foot soles of the mice, indicating localization to sentinel lymph nodes. Arrows indicate probe accumulation in the bladder. Images are reprinted and adapted with permission from [51-62]. Copyright 2007 Elsevier, Copyright 2008 Society of Nuclear Medicine, Copyright 2012 Elsevier, Copyright 2011 American Chemical Society.

Europe PMC Funders Author Manuscripts

Europe PMC Funders Author Manuscripts

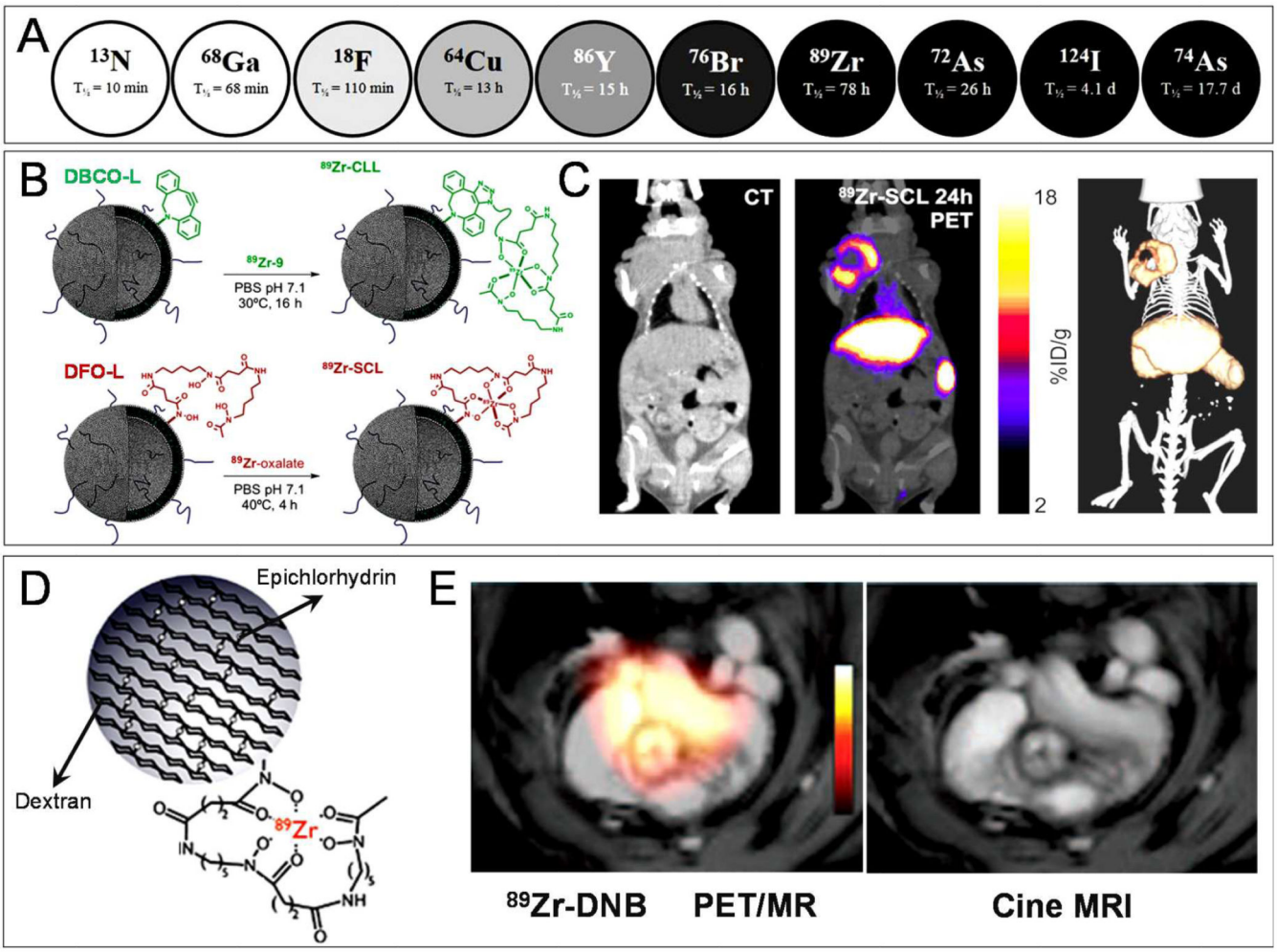

Figure 4. Non-invasive imaging of nanomedicines labeled with long-lived PET nuclides

A. Overview of shorter to longer lived PET radionuclides commonly employed in nuclear medicine and nanomedicine research. **B.** PEGylated liposomes were labeled with ^{89}Zr using two different labeling strategies: 'click labeling' and 'surface chelation'. For click labeling, dibenzoazacyclooctyne (DBCO) was used, while for surface chelation, deferoxamine (DFO) was employed. Due to the higher labeling efficiency and stability, only surface-chelated liposomes (^{89}Zr-SCL) were used for in vivo studies. **C.** NCr nude mice bearing 4T1 breast cancer tumors were used to evaluate the biodistribution and the target site accumulation of ^{89}Zr-SCL. PET-CT imaging was performed at 24 h post i.v. injection, showing prominent accumulation in tumor (upper left), liver (central) and spleen (lower right). **D.** ^{89}Zr-labeled polymeric nanoparticles based on dextran (^{89}Zr-DNP) were generated for macrophage imaging in atherosclerotic plaques. Polymeric dextran chains were crosslinked with epichlorhydrin and functionalized with deferoxamine (DFO) for ^{89}Zr chelation. **E.** PET-MR imaging of ^{89}Zr-DNP showing strong accumulation in the aortic root of atherogenic ApoE$^{-/-}$ mice at 48 h p.i. Images are reprinted and adapted with permission from ref [63;76;77] Copyright 2014 Society of Nuclear Medicine, Copyright 2013 American Heart Association.

Europe PMC Funders Author Manuscripts
Europe PMC Funders Author Manuscripts

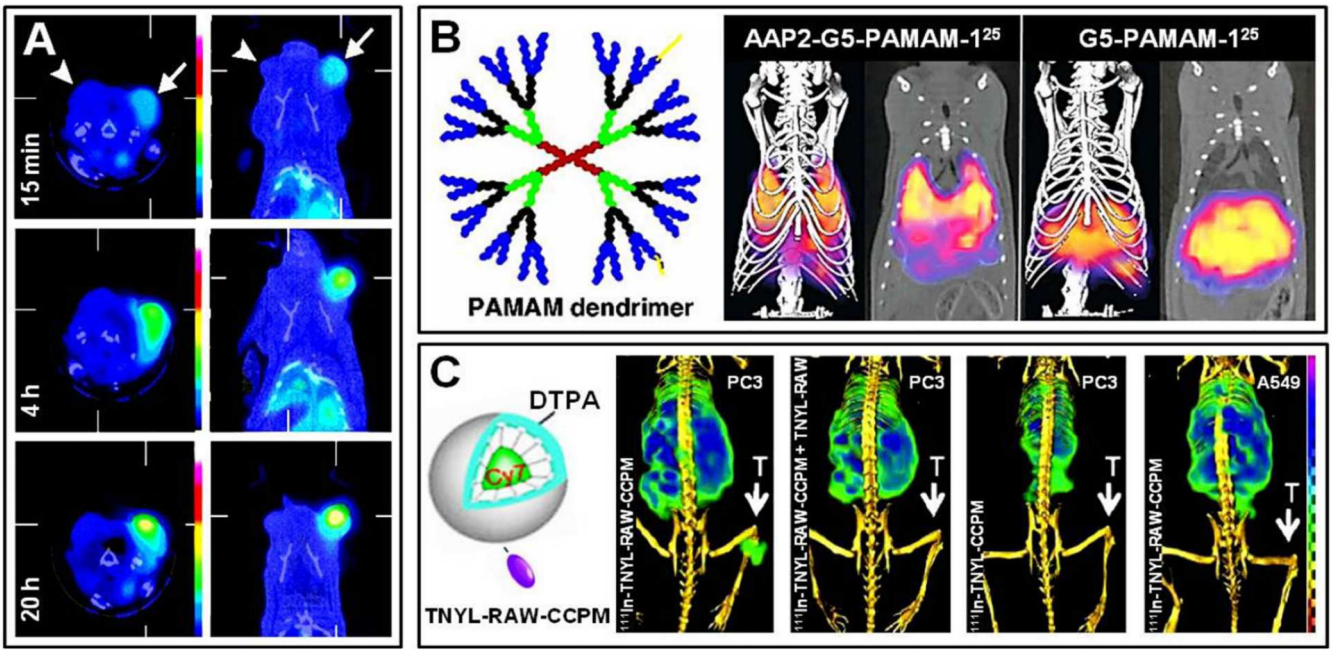

Figure 5. Non-invasive imaging of nanomedicines using SPECT

A. Transaxial and coronal SPECT-CT images of rats bearing head-and-neck squamous cell carcinoma tumors on either side of the skull base. Rats were i.v. injected with ^{99m}Tc-labeled liposomal doxorubicin, and probe accumulation was visualized and quantified in RFA-treated tumors (right; arrow) and sham-treated tumors (left; arrowhead). **B.** Hybrid SPECT-CT imaging of drug targeting to the lung using ^{125}I-labeled APP2 antibody-modified G5-PAMAM dendrimers versus control dendrimers. Images were obtained at 1 h post i.v. injection. 3D volumetric SPECT with iso-surface CT images and corresponding 2D coronal slices are shown. **C.** SPECT-CT imaging of mice bearing PC3 (EphB4R-positive) or A549 (EphB4R-negative) tumors at 24 h after the i.v. administration of ^{111}In-labeled EPhB4R-targeted core-cross linked polymeric micelles (TNYL-RAW-CCPM) and control CCPM. To confirm probe specificity, PC3 tumor-bearing mice were also pretreated with excess free TNYL-RAW peptide, for blocking purposes. Images are reprinted and adapted with permission from ref [78], [79] and [80]. Copyright 2010 Radiological Society of North America, Copyright 2011 Wiley Intersciences, Copyright 2011 Elsevier.

Europe PMC Funders Author Manuscripts
Europe PMC Funders Author Manuscripts

Europe PMC Funders Author Manuscripts

Europe PMC Funders Author Manuscripts

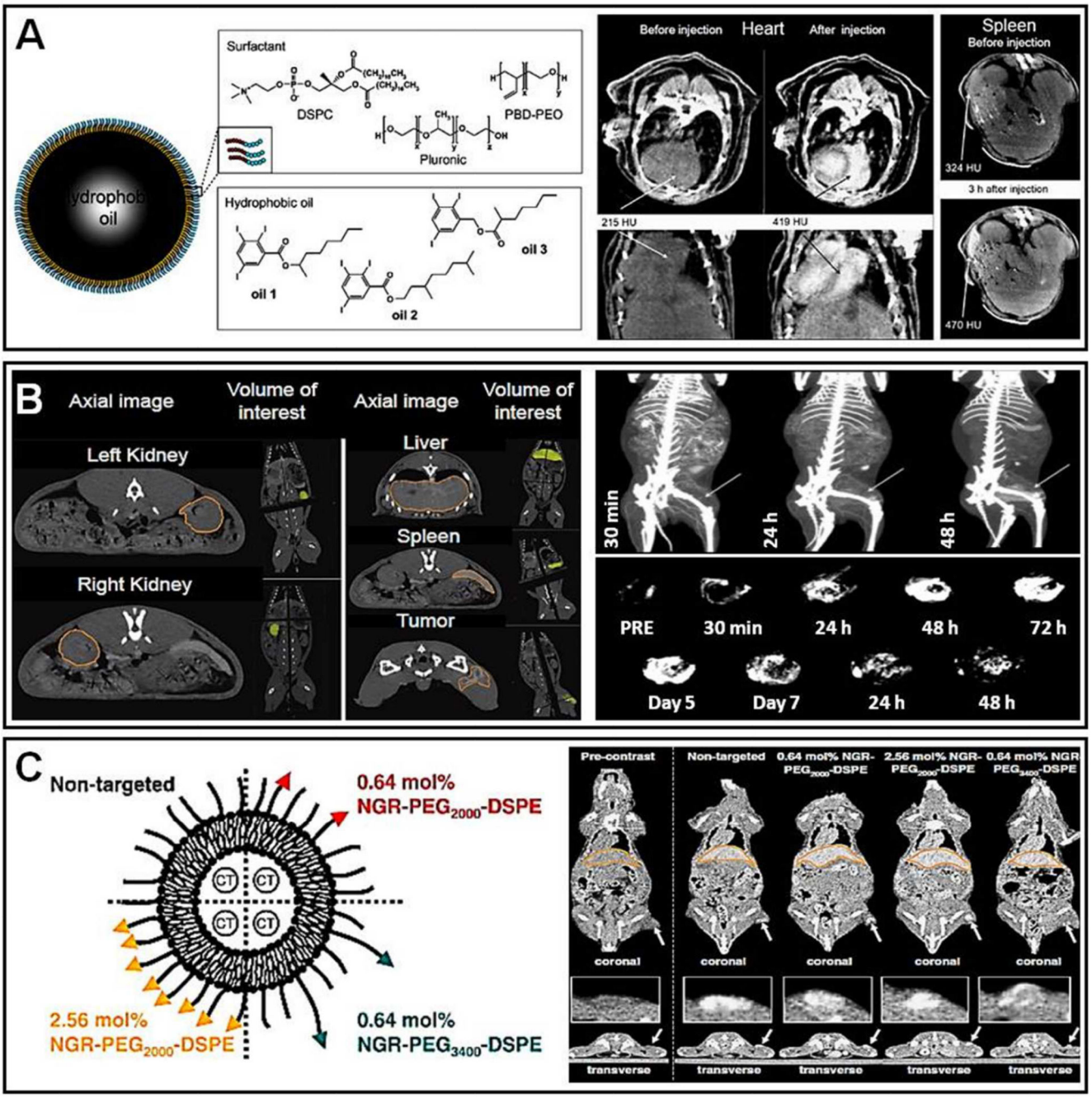

Figure 6. Non-invasive imaging of nanomedicines using CT

A. Left: Schematic depiction of PBD-PEG nanoemulsions. Right: After the i.v. injection of an iodine-containing PBD-PEG nanoemulsion into healthy mice, CT images were obtained in the heart (at 12 min p.i.; arrows in middle panels) and spleen region (at 3 h p.i.; arrows in right panels), confirming classical nanomedicine behavior, with initially high amounts present in systemic circulation, and subsequently significant accumulation in RES organs, such as spleen. **B.** Left: Axial CT images of rabbit kidneys, liver, spleen and tumor obtained at 48 h after the i.v. injection of liposomes containing iohexol. Right: Anterior views of 3D

CT maximum intensity projections (MIP) of a VX2 sarcoma-bearing rabbit at 30 min, 24 and 48 h after the i.v. administration of iodine-containing liposomes. Arrows highlight the VX2 tumor, and EPR-mediated passive drug targeting can be visualized via the gradual opacification of the tumor area. Bottom panels show 3D CT MIP of the segmented tumor volumes before and up to 14 days after liposome injection. **C.** Left: Schematic depiction of non-targeted and several different NGR-targeted iodine-containing PEGylated liposomes. Right: Coronal micro-CT images of H520 tumor-bearing mice at 48 h after the i.v. injection of the four different liposomal nanomedicine formulations. Tumors are highlighted with arrows. The transversal images in the bottom panels provide non-invasive and quantitative information on the heterogeneity of tumor accumulation and intratumoral distribution upon using targeted vs. non-targeted liposomes. Images are reprinted and adapted with permission from ref [81], [82] and [83]. Copyright 2010 Elsevier, Copyright 2011 Elsevier, Copyright 2009 American Chemical Society.

Europe PMC Funders Author Manuscripts

Europe PMC Funders Author Manuscripts

Europe PMC Funders Author Manuscripts

Europe PMC Funders Author Manuscripts

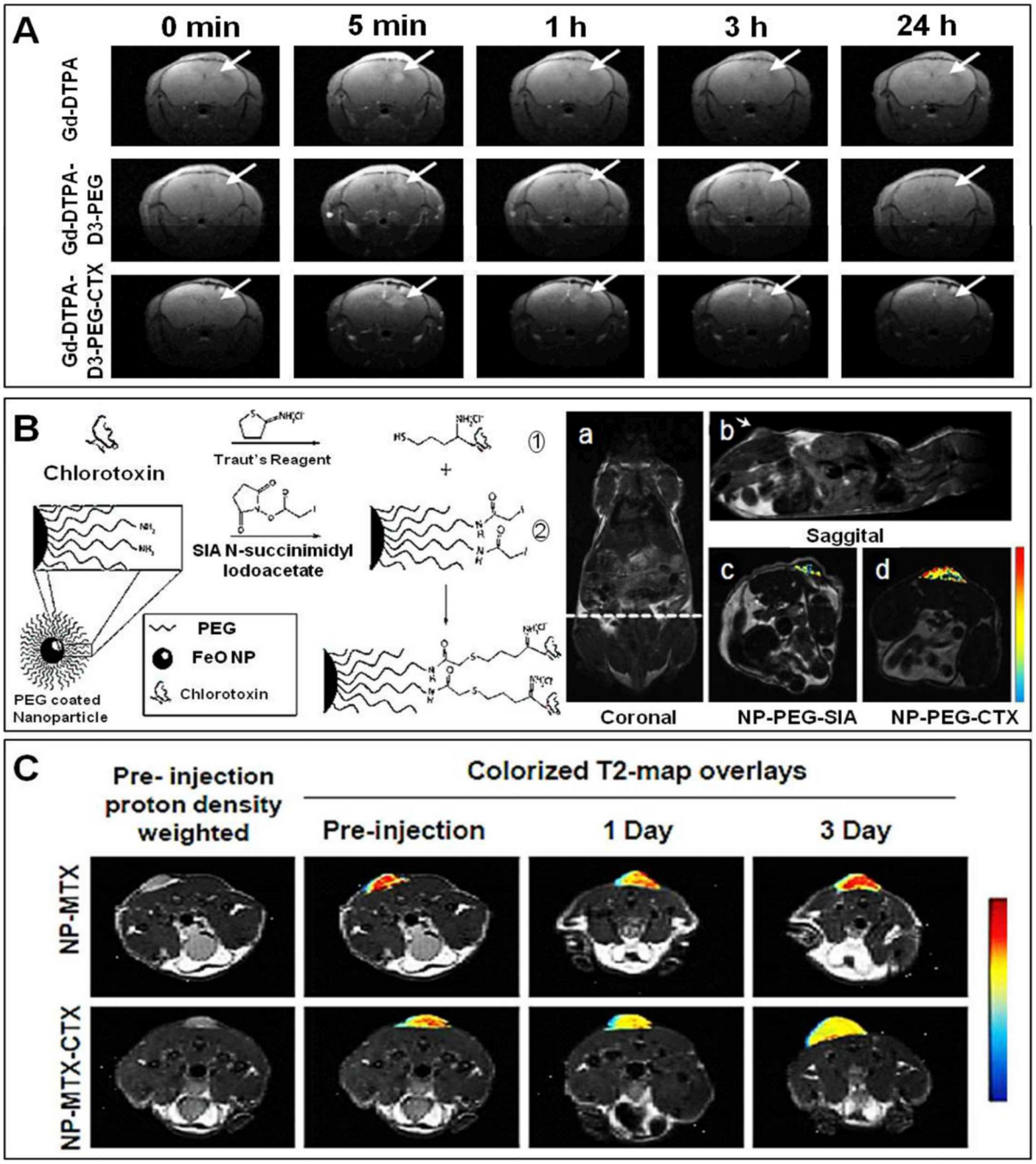

Figure 7. Non-invasive imaging of nanomedicines using MRI

A. Transversal MR images of orthotopic 9L gliosarcoma upon i.v. injection of Gd-DTPA, Gd-DTPA-D3-PEG and Gd-DTPA-D3-PEG-CTX. The signal enhancement indicated by the arrows corresponds to probe accumulation in the tumor lesions from as early as 5 min p.i. onwards. Over time, the signal fades with different kinetics for the different formulations, showing that actively targeted nanoparticles (i.e. chlorotoxin-modified DTPA-D3-PEG) are retained more efficiently at the pathological site than passively targeted nanoparticles. **B.** Left: Schematic depiction of (the preparation of) CTX-targeted iron oxide (IO)

nanoparticles. Right: MR images of a 9L tumor-bearing mouse in coronal (a; dotted line displays the location of the transversal sections displayed in panels c and d), sagittal (b) and transversal (c-d) planes, comparing the tumor targeting potential of passively targeted IO nanoparticles (c) to that of CTX-modified actively targeted IO nanoparticles (d) at 3 h post i.v. injection. The changes in R_2 relaxivity values are depicted by color-coded intensity maps, showing more efficient tumor localization for actively targeted nanoparticles. **C.** MR images of 9L tumor-bearing mice upon the i.v. injection of passively and CTX-modified actively targeted methotrexate (MTX) -containing IO nanoparticles, exemplifying that over time, the latter are retained in tumors more efficiently than the former. Images are reprinted and adapted with permission from ref [94], [95] and [96]. Copyright 2011 Elsevier. Copyright 2008 Wiley Intersciences. Copyright 2008 Future Medicine.

Europe PMC Funders Author Manuscripts

Europe PMC Funders Author Manuscripts

Europe PMC Funders Author Manuscripts

Europe PMC Funders Author Manuscripts

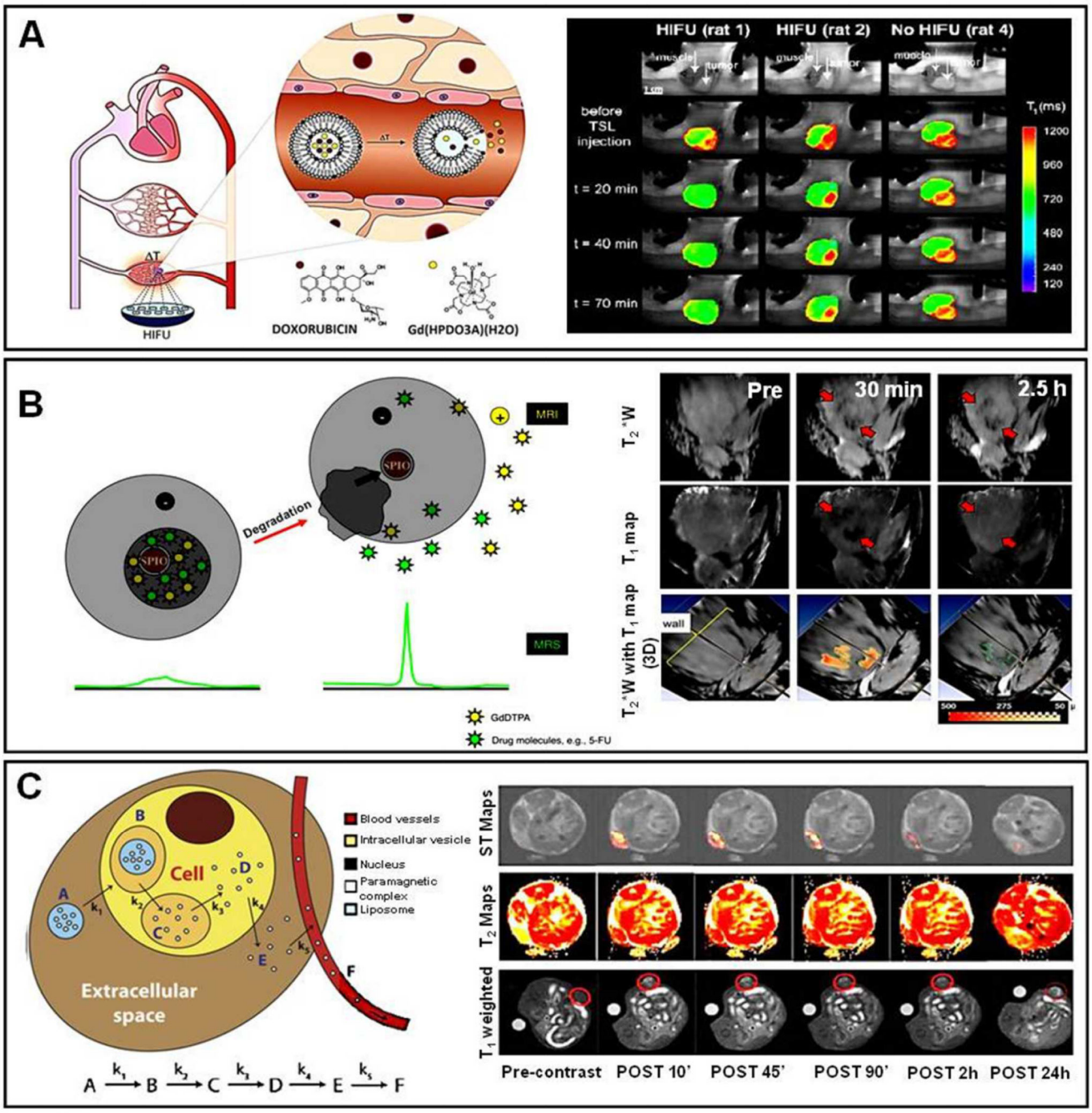

Figure 8. Non-invasive imaging of (model) drug release from nanomedicines using MRI

A. Temperature-sensitive liposomes (TSL) co-loaded with the T_1 MR contrast agent Gd-HPDO3A and doxorubicin were i.v. injected into 9L gliosarcoma-bearing rats, and the tumor area was heated in a controlled manner using MR-guided HIFU. MR imaging was performed before and at several time points after TSL administration and HIFU treatment, exemplifying the release of the MR probe from TSL specifically in heated tumors. Significant inter-individual variability in content release in different tumor-bearing animals can also be observed, e.g. due to central tumor necrosis (see rat 2). **B.** Schematic depiction

Europe PMC Funders Author Manuscripts

Europe PMC Funders Author Manuscripts

of a theranostic PLGA-based nanomedicine formulation containing super-paramagnetic iron oxide (SPIO) nanoparticles, Gd-DTPA and 5-FU. Top right: The tumor localization of the SPIO/Gd-DTPA/5-FU-loaded nanoformulations can be clearly identified as dark regions (red arrows) on the T_2*-weighted MR images, resulting from SPIO-generated contrast. Middle right: T_1 shortening at 30 min p.i., due to the rapid release of Gd-DTPA, and subsequent disappearance of this signal at 2.5 h, due to the rapid diffusion of Gd-DTPA out of the tumor region. Lower right: 3D renderings of the tumor region, showing T_2*-weighted images overlaid with quantitative T_1 values (indicating Gd-DTPA release; in yellow/red). **C.** Left: Schematic depiction of the kinetic model used for the mathematical modeling of the temporal evolution of MR signals upon the intratumoral administration and cellular trafficking of two different paramagnetic liposome formulations acting as multicontrast MR agents. Right: MR images illustrating the temporal evolution of T_1, T_2 and ST signals upon the intratumoral injection of two different MR-responsive liposome formulations. The reported ST and T_2 maps refer to Tm-DOTMA-loaded liposomes; the T_1-weighted images refer to Gd-HPDO3A-loaded liposomes. Images are reprinted and adapted with permission from [97-99]. Copyright 2010-2011 Elsevier.

Europe PMC Funders Author Manuscripts

Europe PMC Funders Author Manuscripts

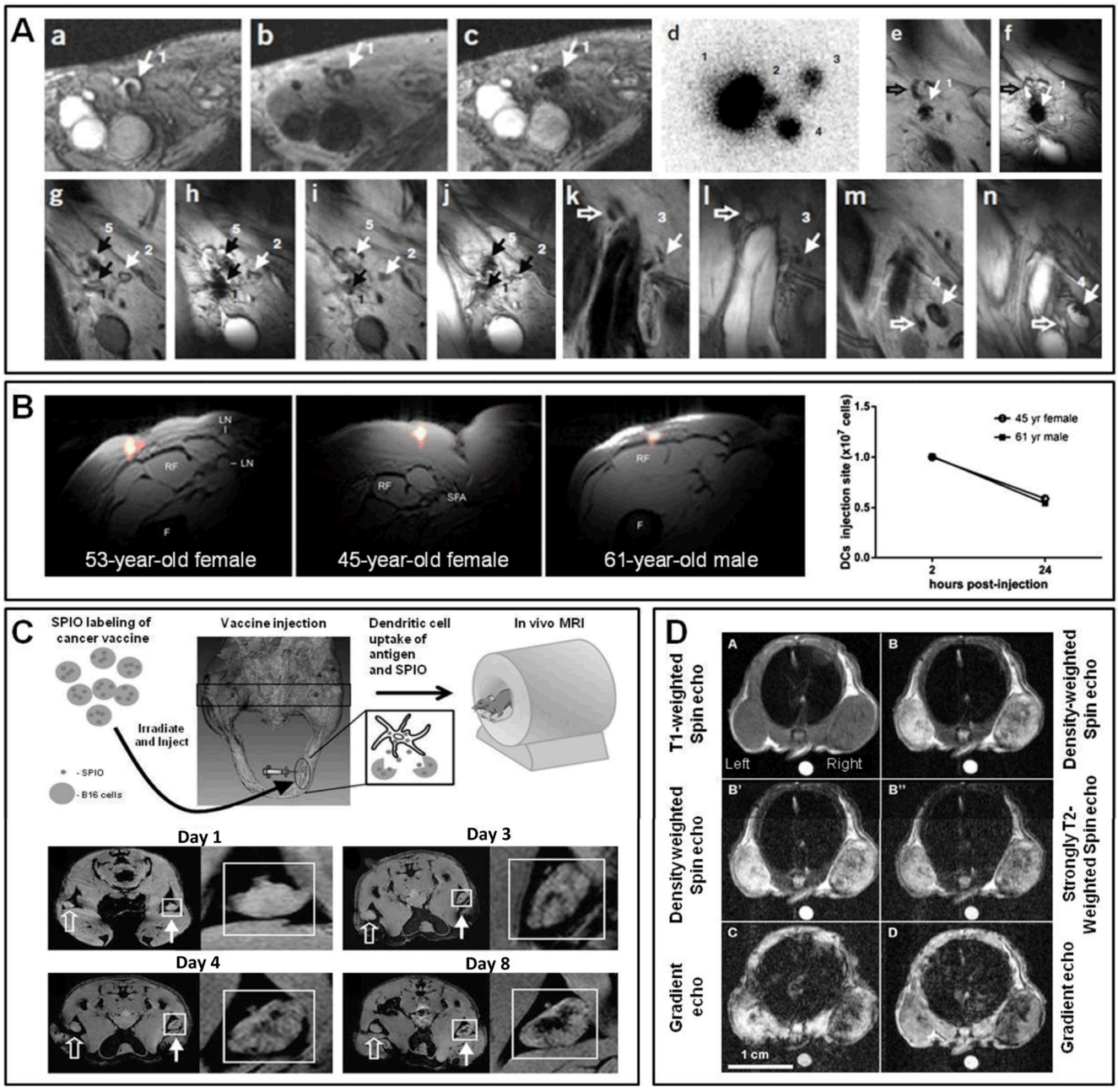

Figure 9. Non-invasive imaging of cell tracking and magnetic drug targeting using MRI

A. Magnetic resonance imaging of dendritic cell (DC) localization and migration in melanoma patients. (a-c): Gradient echo (a,c) and turbo spin echo (b) MR images show the localization of DC (co-labeled with SPIO and ^{111}In) before and after injection in patient 1. In the gradient echo images (a), a hyperintense signal area (1) can be found near the right inguinal lymph node. In the spin echo image (b), which is less sensitive to SPIO, the corresponding lymph node (1) after vaccination could also be seen. (d-n): Tracking the *in vivo* migration of DC. d: In vivo scintigraphy image showing the migration of SPIO- and ^{111}In-colabeled DC from the injection lymph node site (1) to several other lymph nodes

(2-4) at 48 h after DC administration. e-n: Coronal gradient echo and spin echo images illustrating the migration of DC from lymph node 1 (e and f) to other lymph nodes (g-n). Open and closed arrows represent SPIO-negative and SPIO-positive lymph nodes. **B.** Initial proof-of-concept for ^{19}F-based magnetic resonance imaging of intradermally injected DC labeled with a perfluorocarbon-based nanoemulsion into the leg of 3 different colorectal adenocarcinoma patients. The pseudocolor images of ^{19}F-DC are overlaid onto ^{1}H MR anatomical images (F = femur, RF = rectus femoris, SFA = superficial femoral artery, LN = lymph node). On the right, the in vivo data from 2 patients were quantified at 4 h (and not at 2 h; as indicated in the legend) and 24 h post injection, showing that more approximately half of the DC migrate away from the injection site within 24 h. **C.** Top: Schematic depiction of *in vivo* MR cell tracking of inactivated B16 melanoma cell vaccines labeled with SPIO, which after injection into the footpad of mice and drainage via dendritic cells eventually accumulate in the popliteal lymph node (PLN). Bottom: Multigradient T_2-weighted MR images showing gradual vaccine/dendritic cell migration into the PLN (see insets). Closed arrows indicate SPIO-labeled vaccines, open arrows depict unlabeled cell vaccines. **D.** MR imaging and magnetic drug targeting to tumors using i.v. injected maghemite nanocrystal-containing magnetoliposomes (ML). Tumors on the right were exposed to a magnet. A) T1-weighted spin echo; B) and B') density-weighted spin echo; B") strongly T_2-weighted spin echo; C) gradient echo; and D) 3D-spoiled gradient echo. An oil phantom (bright spot on the bottom of the images) was placed on the back of the animals for reference purposes. The tumor on the right clearly appeared darker than the control tumor on the left, exemplifying efficient magnetic drug targeting. Images adapted with permission from [100-103]. Copyright 2005 Nature Publishing Group, Copyright 2014 International Society for Magnetic Resonance in Medicine, Copyright 2009 American Association for Cancer Research, Copyright 2006 Radiological Society of North America.

Europe PMC Funders Author Manuscripts

Europe PMC Funders Author Manuscripts

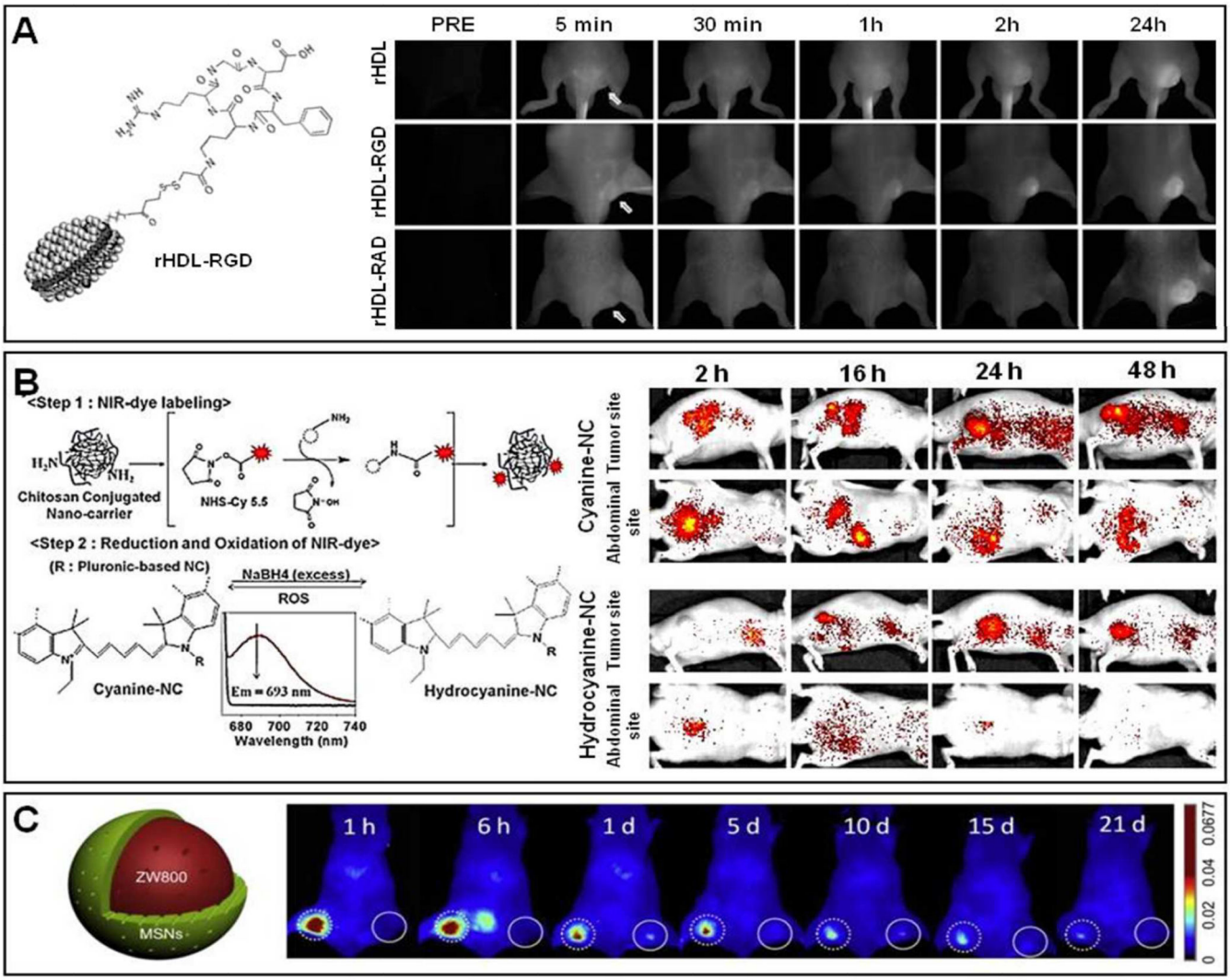

Figure 10. Non-invasive optical imaging of nanomedicines

A. Left: Schematic depiction of an HDL nanoparticle targeted to tumor blood vessels using RGD. Right: 2D FRI of mice bearing subcutaneous EW7 Ewing's sarcoma xenografts i.v. injected with NIRF-labeled rHDL, rHDL-RGD, and rHDL-RAD nanoparticles, showing rapid binding and tumor targeting of RGD-modified rHDL. Arrows highlight the tumor. **B.** Left: Schematic depiction of cyanine- and hydrocyanine-containing nanochitosan (NC). Right: 2D FRI of nude mice bearing SCC7 tumors after the i.v. injection of hydrocyanine-NC and cyanine-NC. Background signals from the abdominal and liver region were evident in case of cyanine-conjugated NC, whereas tumor-specific signals were prominent in case of hydrocyanine-conjugated NC. **C.** Left: Schematic depiction of a mesoporous silica nanoparticle (MSN) containing the fluorophore ZW800. Right: 2D FRI of sentinel lymph nodes (SLN) after the food pad injection of MSN nanoparticles. Dotted circle: Tumor SLN. Solid line: Normal SLN. Images reprinted and adapted with permission from [62;117;118]. Copyright 2010 Federation of American Society for Experimental Biologists (FASEB), Copyright 2011 Elsevier, Copyright 2012 Elsevier.

Europe PMC Funders Author Manuscripts
Europe PMC Funders Author Manuscripts

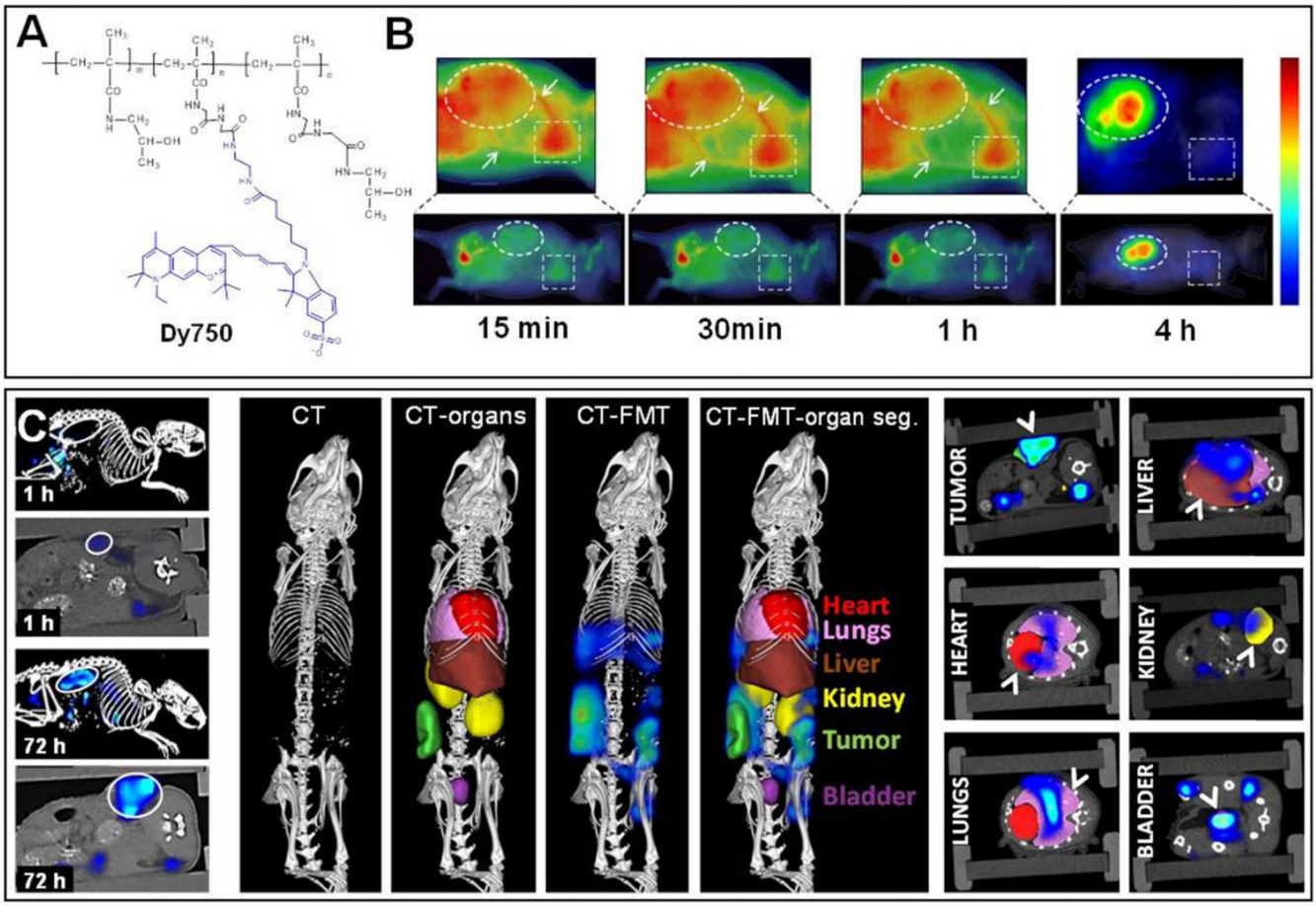

Figure 11. Non-invasive optical imaging of nanomedicines

A. Schematic depiction of a NIRF (Dy750) -labeled pHPMA-based polymeric drug carrier. **B**. 2D FRI of the biodistribution of pHPMA-Dy750 in CT26 tumor-bearing mice, confirming prolonged circulation times (heart highlighted in square, large blood vessels with arrows) and efficient EPR-mediated drug targeting to tumors over time (circle). **C**. Hybrid CT-FMT imaging of nanomedicine biodistribution. Left: 3D FMT images fused with high resolution micro-CT, demonstrating biodistribution of pHPMA-Dy750 in mice bearing CT26 tumors at 1 and 72 h. Middle: Principle of whole-body CT-FMT, which relies on CT-based organ segmentation, and subsequent fusion with FMT-based probe accumulation. Right: 2D CT planes fused with FMT signals representing pHPMA-Dy750 accumulation in tumor, heart, lung, liver, kidney and bladder are shown. Images are reproduced and adapted with permission from [120]. Copyright 2013 American Chemical Society.

Europe PMC Funders Author Manuscripts
Europe PMC Funders Author Manuscripts

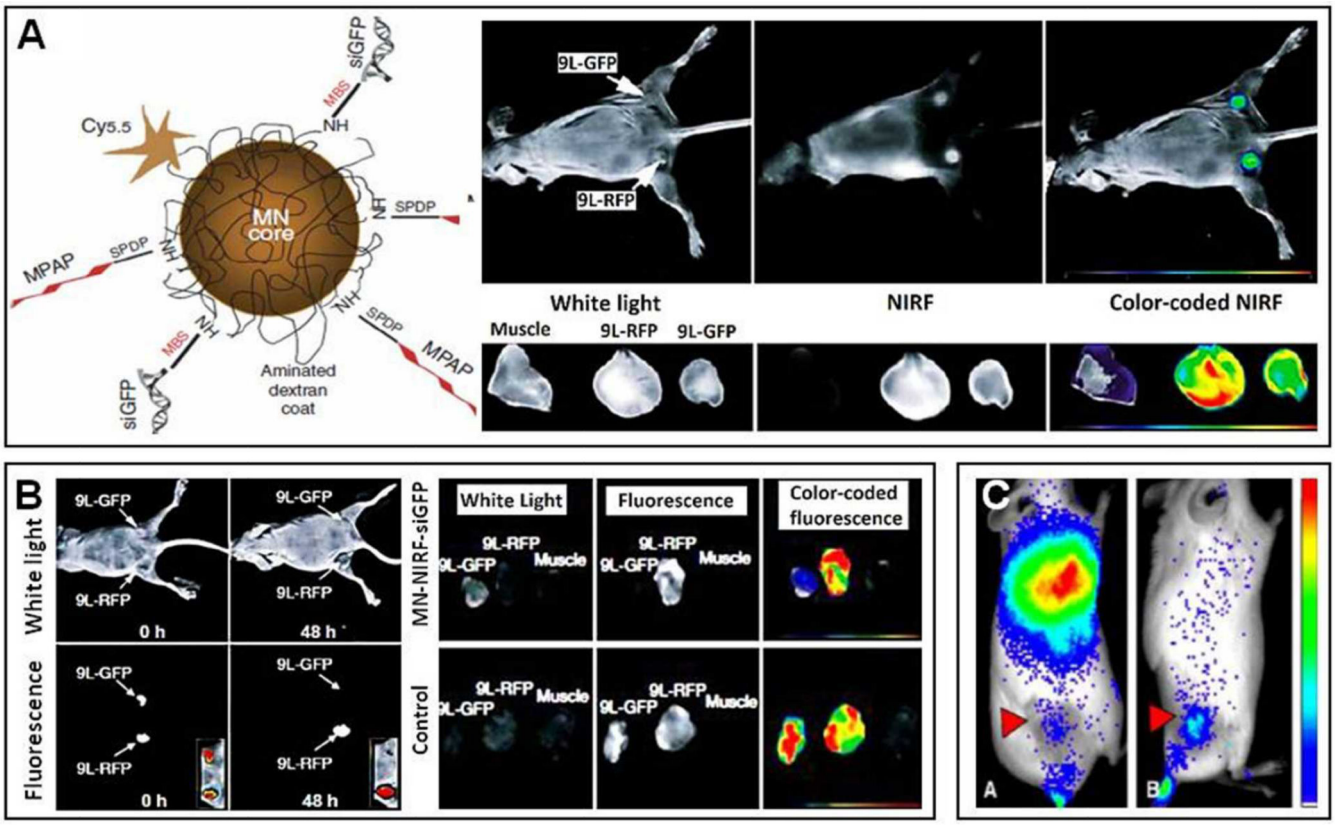

Figure 12. Non-invasive optical imaging of nucleic acid-containing nanomedicines

A. Left: Schematic depiction of iron oxide-based magnetic nanoparticles (MN) containing a NIRF (Cy5.5) and siRNA directed against GFP. Right: Optical imaging of GFP- and RFP-transfected 9L gliosarcoma-bearing nude mice treated with MN-NIRF-siGFP. High NIRF signals in both GFP- and RFP- transfected tumors (indicated by arrows), and low accumulation in muscle tissue, confirm relatively efficient tumor targeting. **B.** *In vivo* (left) and *ex vivo* (right) optical imaging of the gene silencing efficacy of MN-NIRF-siGFP, showing strong and selective GFP silencing in GFP-transfected tumors, but not in RFP-transfected control tumors. **C.** Optical imaging of DNA delivery using bioluminescence imaging. N2A tumor-bearing mice were treated with linear PEI polyplexes (left) and G5-PAMAM polyplexes (right) containing plasmid DNA encoding for luciferase, and gene delivery and transfection efficacy were assessed at 24 h p.i., showing that L-PEI mainly delivered DNA to the lung, whereas G5-PAMAM enabled relatively selective delivery to tumors (arrowheads). Images reprinted and adapted with permission from [163] and [164]. Copyright 2007 Nature Publishing Group, Copyright 2009 Elsevier.

Europe PMC Funders Author Manuscripts
Europe PMC Funders Author Manuscripts

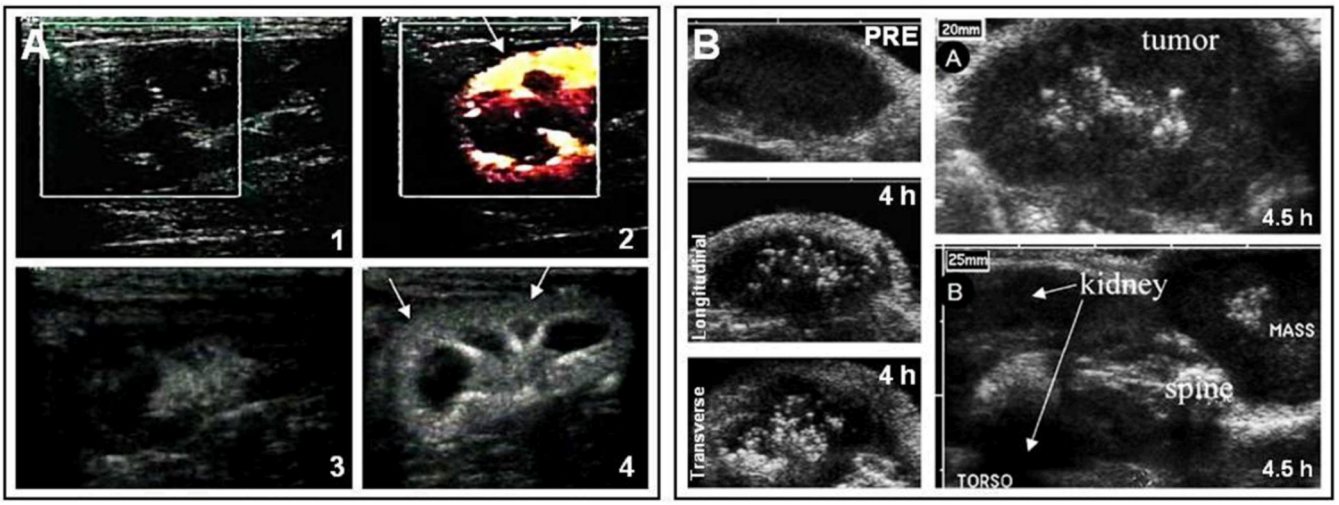

Figure 13. Non-invasive imaging of nanomedicines using US

A. Power Doppler US imaging of the right rabbit kidney before (panel 1) and after (panel 2) the i.v. administration of ST-68N-based nanobubbles, illustrating high perfusion. Arrows indicate the kidney capsule. Pulse inversion harmonic images of the right kidney before and after ST-68N administration are shown in panels 3 and 4, respectively. **B.** B-mode US imaging of MDA-MB-231 xenografts upon the intratumoral injection of PEG-PLLA-PFP-based nanobubbles loaded with doxorubicin. US images were taken before (upper left panel), and at 4 h after i.t. administration, in longitudinal (middle left panel) and transversal (lower lower panel) planes. The upper right panel exemplifies tumor localization of i.v. administered nano/microbubbles at 4.5 h p.i. The lower right panel depicts a trans-torso image of the same mouse, illustrating accumulation in tumor (designated as “mass”), kidneys and spine. Images reprinted and adapted with permission from [171;172]. Copyright 2006 Elsevier, Copyright 2007 Oxford University Press.

Europe PMC Funders Author Manuscripts
Europe PMC Funders Author Manuscripts

Europe PMC Funders Author Manuscripts

Europe PMC Funders Author Manuscripts

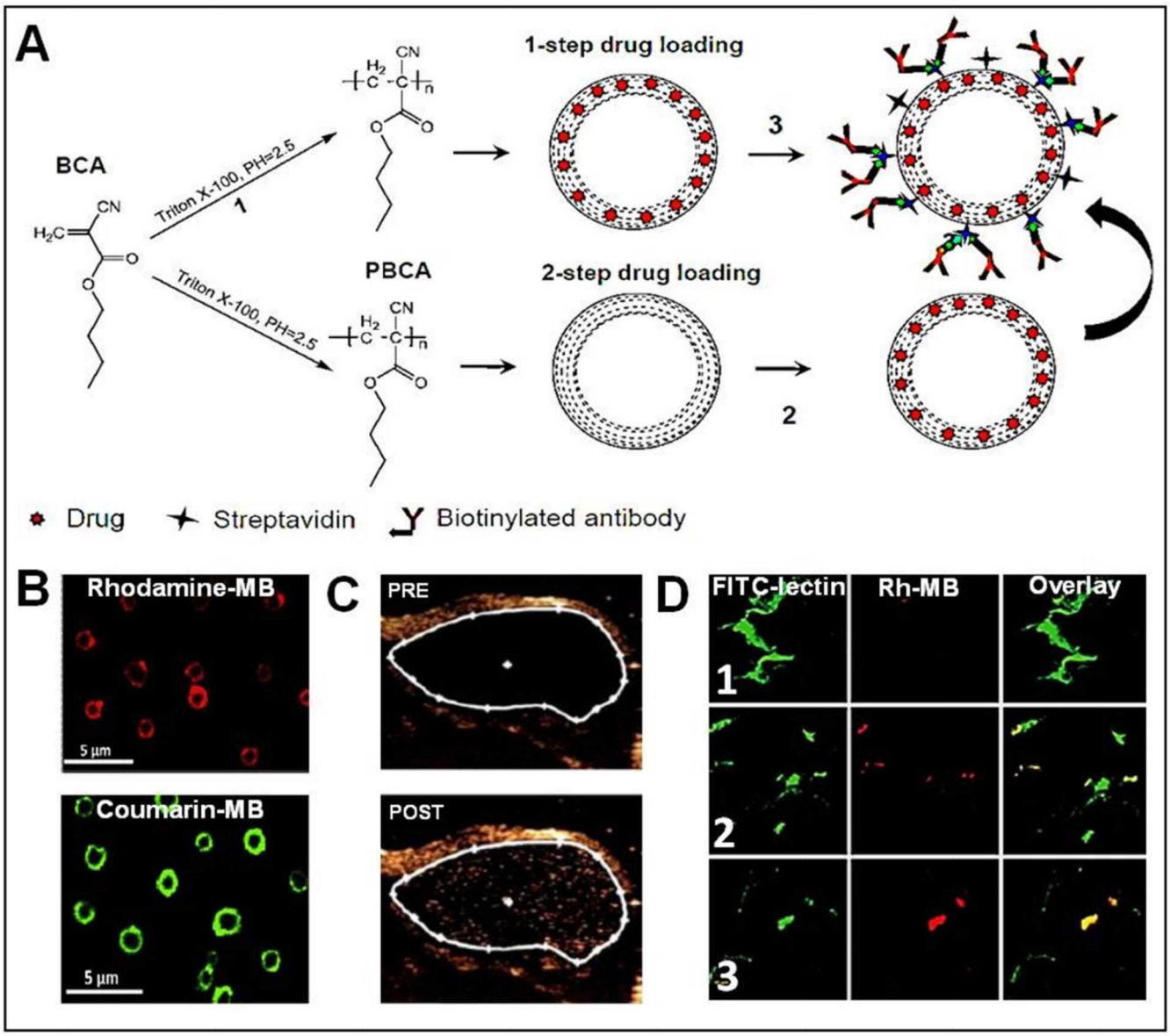

Figure 14. Image-guided, targeted and triggered (model) drug delivery to tumors using US plus MB

A. Schematic depiction of the synthesis of VEGFR2-antibody-targeted polymeric MB loaded with (model) drugs via a 1-step or 2-step procedure. **B**. Two-photon laser scanning microscopy images of MB loaded with the model drugs Rhodamine-B (red) and Coumarin-6 (green). **C**. US imaging of CT26 tumors prior to and 7 min after the i.v. administration of Rhodamine-B-loaded and VEGFR2-targeted MB, showing efficient binding to angiogenic blood vessels. **D**. Fluorescence microscopy analysis of model drug delivery to tumors upon the i.v. injection of Rhodamine-B-loaded and VEGFR2-targeted MB without exposure to US (panel 1), with exposure to three destructive US pulses at 7 min p.i. (panel 2), and with continuous exposure to US for 7 min (panel 3), exemplifying significant Rhodamine-B release in tumors upon combining MB and US. Images reprinted and adapted with permission from [173]. Copyright 2012 Elsevier.

Europe PMC Funders Author Manuscripts

Europe PMC Funders Author Manuscripts

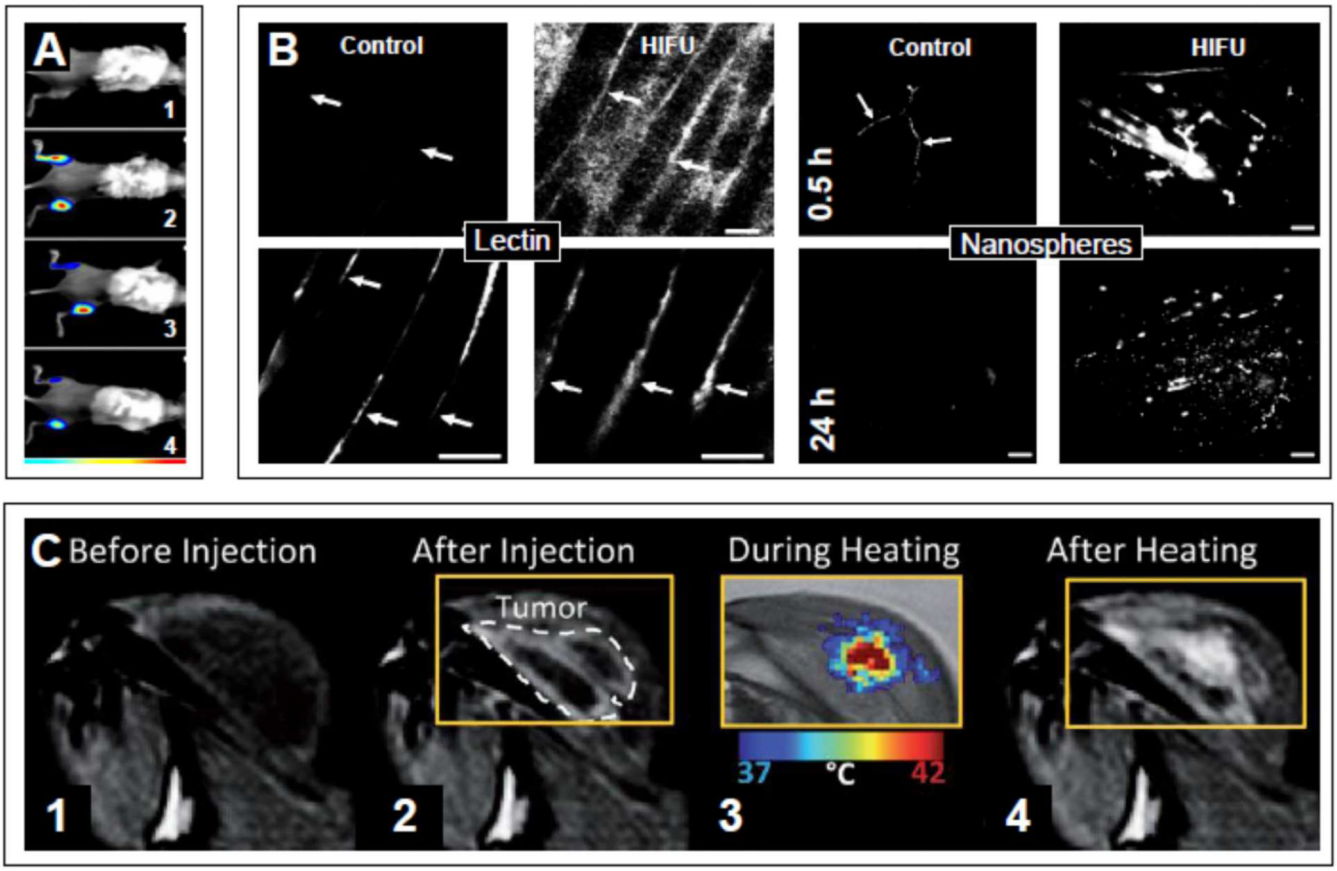

Figure 15. US-based enhancement of (model) drug delivery

A. 2D FRI images of mice intratumorally injected with MB plus TOTO-3 (a cell membrane-impermeable model drug), and treated with US (lower tumor) or left untreated (upper tumor). Optical imaging of TOTO-3 internalization and retention in tumors was carried out before US (1), immediately afterwards (2), and 2 h (3) and 4 h (4) later. **B**. Accumulation of i.v. administered fluorescently labeled lectin and nanospheres in HIFU-pretreated and control muscle tissue in mice at 0.5 and 24 h. Both probes showed significantly more extravasation upon HIFU treatment. Bar: 50 μm. **C.** MR monitoring of US-induced and hyperthermia-mediated T1-contrast agent release from temperature-sensitive liposome. Immediately after liposome administration, the perfusion of tumor blood vessels can be visualized (panel 2). Subsequently, US-mediated mild hyperthermia is applied to the tumor, which can be monitored via real-time MR-thermometry (panel 3), and which leads to efficient Gd-HPDO3A (model drug) release from the temperature-sensitive liposomes only in the heated area (panel 4). Images are reprinted and adapted from [167], [189] and [186]. Copyright 2009 Elsevier, Copyright 2009 Elsevier, Copyright 2011 Informa Healthcare.

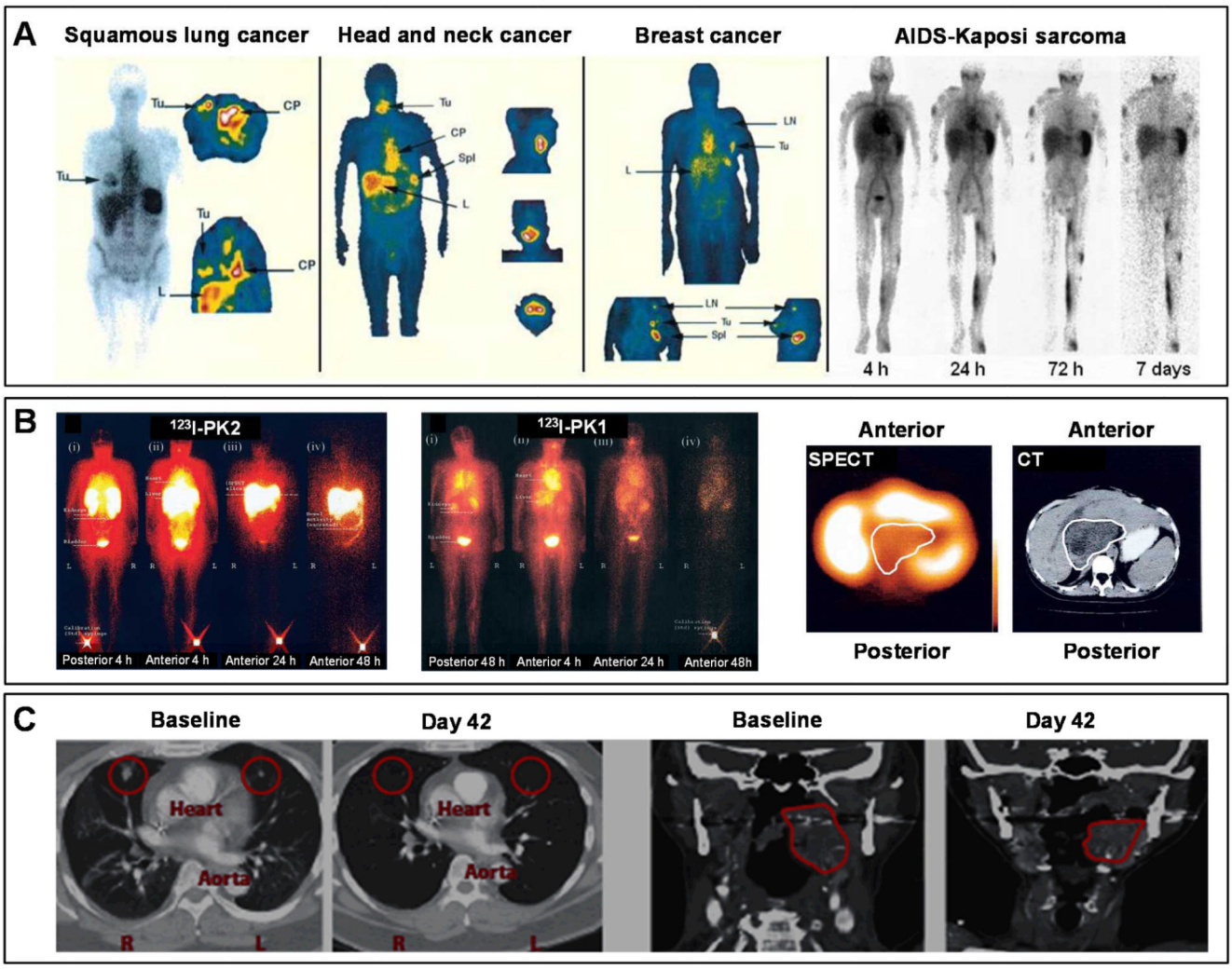

Figure 16. Translational imaging of nanomedicines

A. Monitoring passive drug targeting. The tumor accumulation of ^{111}In-labeled PEGylated liposomes was evaluated in patients suffering from squamous cell lung carcinoma, head and neck cancer, and breast cancer. Gamma camera images were captured at 72 h post i.v. injection, showing clear contrast enhancement in tumors (Tu). Head and neck cancers and squamous lung carcinomas showed high accumulation of the liposomes in the tumor, while breast cancers showed relatively low accumulation. CP represents the cardiac pool (i.e. liposomes in circulation), and L and Spl illustrate accumulation of the liposomes in liver and spleen, respectively. Ln indicates a metastatic lymph node, which also accumulates liposomes fairly efficiently. In the right panel, the longitudinal biodistribution of liposomes in a patient suffering from AIDS-related Kaposi sarcoma is presented, showing strong accumulation in primary tumors (upper and lower leg region), as well as in metastatic lesions (shoulder and facial region). **B.** Monitoring active drug targeting. Left panels: Gamma camera imaging upon the administration of ^{123}I-labeled Gal-pHPMA-GFLG-doxorubicin (PK2), targeting asialoglycoprotein receptors overexpressed by hepatocytes via incorporated galactosamine moieties, as well as of ^{123}I-labeled PK1 (similar polymer-drug

Europe PMC Funders Author Manuscripts
Europe PMC Funders Author Manuscripts

conjugate, but without the liver-specific targeting ligand). Anterior and posterior images at 4 and 24 h exemplify efficient targeting of PK2 to the liver. Right panels: hybrid SPECT-CT imaging of PK2, illustrating accumulation in the peripheral (healthy) regions of the liver, rather than in the central tumor mass (dark area in the middle of the CT image). **C.** Monitoring treatment efficacy. Left panels: Contrast-enhanced CT scans obtained in a cholangiosarcoma patient with lung metastases treated with PSMA-targeted and docetaxel-loaded PLGA nanoparticles (DTXL-TNP). The red circles indicate metastatic lesions observed prior to treatment, which disappeared at day 42 after treatment initiation. Right panels: Contrast-enhanced CT scans obtained in a patient suffering from tonsillar cancer (red circle) treated with DTXL-TNP, showing significant tumor shrinkage at day 42 after treatment initiation. Images are adapted and reproduced with permission from [192], [193] and [194]. Copyright 2006 American Association for Cancer Research, Copyright 2012 American Society of Clinical Oncology, Copyright 2012 American Association for the Advancement of Science.

Europe PMC Funders Author Manuscripts

Europe PMC Funders Author Manuscripts

Europe PMC Funders Author Manuscripts

Europe PMC Funders Author Manuscripts

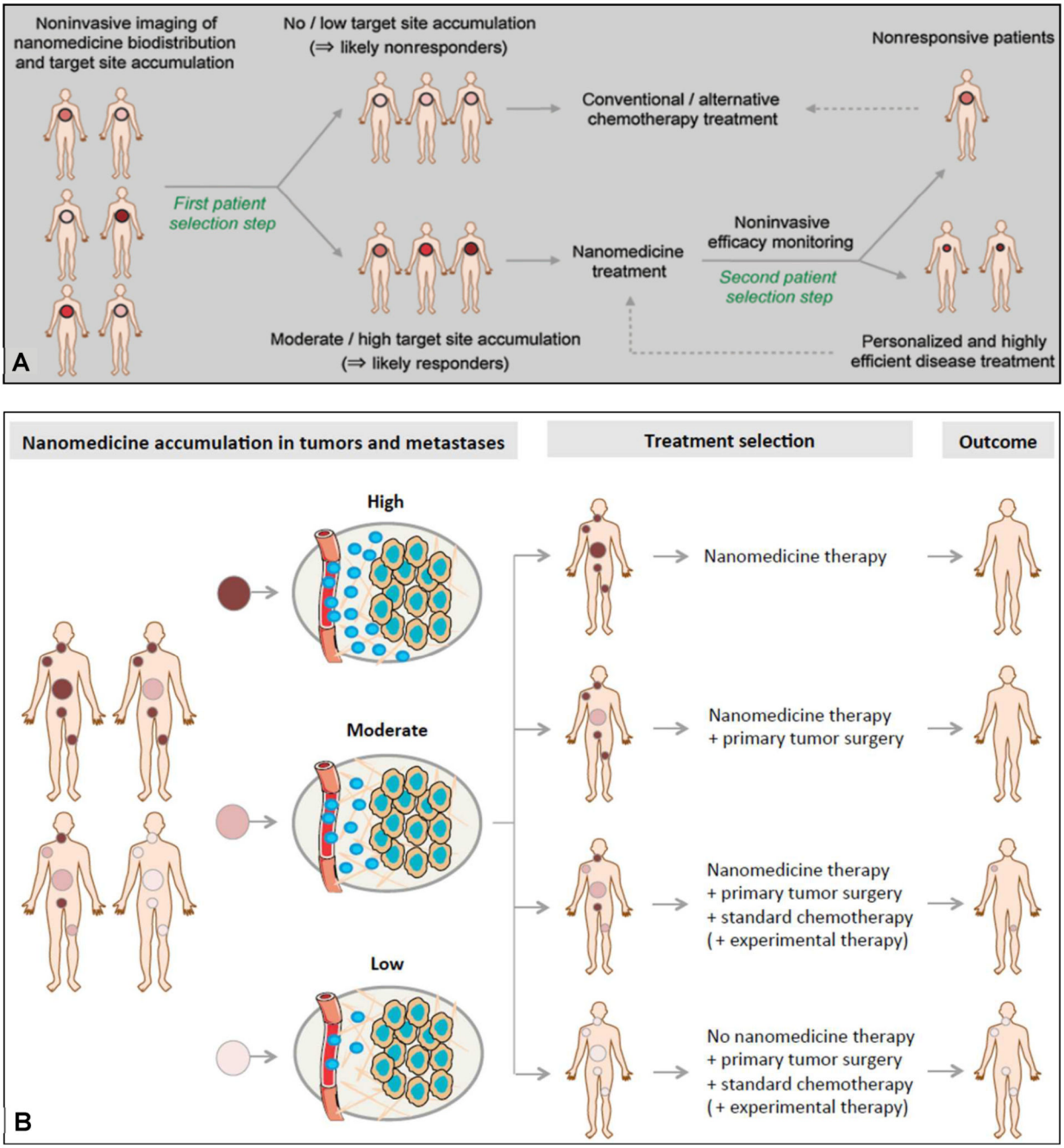

Figure 17. Personalized nanomedicine

Schematic depiction demonstrating how the combination of non-invasive imaging and tumor-targeted drug delivery can be used to individualize and improve nano-chemotherapeutic treatment regimens. Ideally, not only accumulation in primary tumors should be considered (A), but also localization in metastases (B). Depending on the accumulation pattern of nanomedicine formulations in both primary tumors and metastases, optimized treatment regimens can be envisaged for each individual patient, enabling personalized and optimized therapies. Images reproduced with permission from [191,195].

Copyright 2012 American Association for Cancer Research. Copyright 2015 Informa Healthcare.

Europe PMC Funders Author Manuscripts

Europe PMC Funders Author Manuscripts